# COMPARING BOREAL FOREST REGENERATION STRUCTURES BETWEEN HARVESTING AND WILDFIRE DISTURBANCE WITH 3D MORPHOLOGY

TEJUMADE ADEJOKE OJO

A THESIS
TO BE SUBMITTED TO THE FACULTY OF GRADUATE STUDIES
FOR PARTIAL FULFILLMENT OF THE REQUIREMENTS FOR
THE DEGREE OF MASTER OF SCIENCE

GRADUATE PROGRAM IN GEOGRAPHY
YORK UNIVERSITY
TORONTO, ONTARIO

May 2026

**Abstract**

Quantifying landscape structure is central to understanding boreal forest disturbance and recovery. This study examined the three-dimensional morphological structure of post-disturbance regeneration following 30 events in Ontario (15 wildfires and 15 harvests). Annual binary land-cover maps were stacked into temporal voxel cubes (*x, y, t*) and segmented into eight 3D morphological classes. Site-level morphological proportions were analyzed using univariate and multivariate statistical methods to evaluate differences among disturbance types and ecoregions. Wildfire sites contained significantly higher proportions of MASS, while harvested sites contained significantly higher proportions of BOND ($p < 0.05$). Morphological composition also differed significantly between ecoregions, with western sites exhibiting greater MASS, VOID-VOLUME, and VOID proportions and eastern sites showing greater CRUMB and CIRCUIT proportions ($p < 0.05$). Wildfire sites displayed greater structural consistency, whereas harvested sites showed higher variability. These findings indicate that harvesting does not replicate wildfire regeneration patterns and that disturbance type and regional context jointly influence boreal forest recovery.

**Acknowledgements**

"Bless the LORD, O my soul: And all that is within me, *bless* his holy name.!" Ps. 103:1

I would like to express my deepest gratitude to my supervisor, Professor Tarmo Remmel, thank you for believing in me. Your steady guidance, thoughtful advice, and unshakable patience gave me the space to grow both intellectually and personally. I will always be thankful for your time, your honesty, your encouragement and your unwavering support.

To my committee members, Dr. Adeyemi Olusola and Dr. Connie Ko, thank you for your valuable insights, support and careful reading of my work. Your feedback sharpened my thinking and helped me take this research further than I thought possible.

I also want to thank the Natural Sciences and Engineering Research Council of Canada (NSERC) Discovery Grant (RGPIN-2021-03645) awarded to my supervisor, and the Catalyzing Interdisciplinary Research Cluster (CIRC) grant awarded by the Vice-President Research and Innovation at York University to my supervisor, for the financial support that allowed me to carry out this research and for the opportunity to present my research at the Canadian Association of Geographers Annual Conference in 2025. I am also sincerely grateful to have received the Michael Bordt Scholarship, established to support graduate students in Environmental Studies whose research applies informatics to environmental statistics, and the York University Graduate Scholarship. These awards further supported the completion of my research. Your investment in students like me means more than words can express.

To Tricia Fuller Davison, your advice about balance was just as important as any academic feedback. Thank you so much for your support and for always being available to answer my endless questions with patience and kindness.

To my friends and PATTERN Lab, thank you for your laughter, your encouragement, and your quiet reminders that I was not alone in this. I am grateful for every time, check-in, and distraction that helped me stay grounded.

To my husband, thank you for standing by me. Your support and belief in me made all the difference. To my mother and mother-in-law, thank you for your incredible support during one of the most transformative times of my life.

**Table of contents**

**List of figures**

**List of tables**

## 1 Introduction

The boreal forest is one of the largest and most ecologically significant terrestrial biomes on Earth, spanning North America, Europe, and Asia and covering approximately 30% of the world's forested land (Hayes et al., 2022). This biome plays a critical role in regulating global climate systems by storing large quantities of carbon in forest biomass and soils (Bradshaw & Warkentin, 2015; Gauthier et al., 2015). In addition to regulating carbon, the boreal forest filters water, moderates temperature, and supports diverse ecological processes that shape large-scale landscape dynamics (Kurz et al., 2013).

Ecologically, the boreal forest is characterized by cold climates, short growing seasons, and long winters. where mean monthly temperatures remain below freezing for five to seven months of the year (Jorgenson, 2015). Across the circumboreal biome, vegetation is dominated by coniferous species such as black spruce (*Picea mariana*), jack pine (*Pinus banksiana*), tamarack (*Larix laricina*), balsam fir (*Abies balsamea*), Norway spruce (*Picea abies*), Scots pine (*Pinus sylvestris*), and white spruce (*Picea glauca*), often intermixed with shade-intolerant deciduous species, including trembling aspen (*Populus tremuloides*), birches (*Betula pendula, B. pubescens*), and white birch (*Betula papyrifera*) (Brassard & Chen, 2006; Brandt et al., 2013; Hayes et al., 2022).

Soils in the boreal region are typically thin, acidic, and nutrient-poor, yet the slow decomposition of organic matter forms variable-depth organic layers that sustain vegetation despite harsh growing conditions (Turkington, 2001; Vankat, 2002). These structural and environmental constraints contribute to a regenerative forest ecology, in which disturbance is required for forest renewal (Jayen et al., 2006; Gauthier et al., 2015). In boreal forests, several dominant tree species depend on wildfire to initiate regeneration. Jack pine produces serotinous cones that open in response to high temperatures, allowing seeds to be released following fire (Rouse, 1986; Forest, 1993; Liu et al., 2022). Experimental burning studies (Sharpe et al., 2017) show that cone opening and seedling establishment in jack pine are strongly controlled by fire intensity and post-fire seedbed conditions, with little to no regeneration occurring in the absence of burning. Black spruce also relies on fire, retaining semi-serotinous cones that release seeds following burning and promote regeneration on exposed organic and mineral soils (Viereck, 1973; Johnstone et al., 2010). In addition, disturbance plays a central role in the regeneration of

trembling aspen, which responds rapidly to intense canopy mortality through prolific root suckering. Long-term observations from northern Ontario show that aspen regeneration is strongest where disturbance extensively removes overstory cover, whereas limited disturbance results in reduced stem density and growth over time (Groot et al., 2009). Together, these species illustrate how wildfire is tightly linked to regeneration processes and long-term forest structure in boreal ecosystems.

Beyond its ecological role, the boreal forest has substantial economic, cultural, and social importance. Globally, it supplies approximately 37% of industrial timber; thus, about two-thirds of the biome is actively managed for wood production (Girona et al., 2023). In Canada, boreal forests contribute significantly to the economy through timber, pulp, and forest-based manufacturing while supporting ecosystem services, wildlife habitat, and traditional Indigenous land relationships (Burton et al., 2006; Golden et al., 2015). Maintaining ecological integrity in this biome is therefore essential not only for forest resilience but also for sustaining livelihoods, biodiversity, and climate mitigation strategies.

However, Canada's boreal forest is experiencing increasing pressure from both natural and anthropogenic disturbances. Annually, approximately 6 Mha are affected by wildfire, insects, or disease, while industrial harvesting disturbs an estimated 400,000 ha (Wells et al., 2020). As disturbance frequency, intensity, and spatial extent continue to shift under climate change, understanding how boreal forests regenerate across disturbance types has become a priority for forest science and management (Walker et al., 2020).

In boreal forest ecosystems, wildfire has historically been a dominant disturbance, influencing forest composition, spatial patterning, and regeneration dynamics through space and time (Turner, 1989; Liu et al., 2022). Since the period of massive industrialization, forest landscapes have also been reshaped by human activities, particularly through timber harvesting, which now represents a major source of disturbance across much of the managed boreal forest. Modern forest policy increasingly promotes the natural disturbance emulation (NDE) (Kuuluvainen & Gauthier, 2018; MNRF, 2021), whereby harvesting practices are designed to approximate the spatial characteristics and ecological effects of natural wildfire through harvest configuration, retention strategies, and regeneration standards (OMNR, 2001). However, the extent to which harvested forest stands recover, in terms of forest structure, to match wildfire-

disturbed stands remains uncertain. Differences in disturbance mechanisms may lead to different spatial and temporal patterns of regeneration, even when management objectives aim to emulate natural processes.

Quantitative landscape ecology is concerned with understanding the composition and configuration of ecological systems and the processes that shape these patterns through time, using analytical tools to describe, analyze, and monitor landscape structures and changes (Remmel & Csillag, 2003; Lafortezza et al., 2005; Lausch et al., 2015). Composition refers to the types and abundance of elements present in a landscape, while configuration describes how these elements are arranged and connected within it. A wide range of landscape metrics, including patch size, shape, edge density, and connectivity, have been developed to quantify and assess landscape changes over time and measure ecosystem function across scales (Riitters et al., 1995; Hargis et al., 1998; Nowosad & Stepinski, 2019). These metrics support the interpretation of spatial heterogeneity and ecological process (Frelich, 2016; Schindler et al., 2008), but they can be abstract, scale-dependent, and difficult to compare or interpret visually across landscapes (Riitters et al., 1995; Wu, 2004). Landscape structure emerges from the interaction of physical, biological, and human drivers and may remain relatively stable over extended periods or change rapidly in response to disturbance events (Turner, 1989; O'Farrell & Anderson, 2010; J. Wu, 2013).

In this study, forest morphology is used to describe the form and spatial organization of forest structure, including how vegetated and non-vegetated elements are arranged across space and time following disturbance (Turner, 2005; Vogt et al., 2007; Remmel, 2022). A morphological perspective emphasizes structural organization rather than vegetation presence alone, enabling examination of how recovery unfolds beyond simple measures of boreal forest cover or greenness.

Understanding whether boreal forest stands disturbed by wildfire and harvesting recover with similar space–time regeneration patterns over time (Bartels et al., 2016; Mulverhill et al., 2019) is therefore important for evaluating the effectiveness of disturbance-based forest management. In this study, the third analytical dimension represents time rather than vertical forest height. Annual disturbance maps are stacked into a space–time (*x, y, t*) cube in which each voxel records whether a location is disturbed or undisturbed each year. Morphological

segmentation is then applied to this layered disturbance history to quantify how disturbance states persist, contract, fragment, reconnect, or become enclosed through time. The structure measured in this framework, therefore, refers to space–time disturbance and regeneration dynamics, not three-dimensional canopy or vegetation structure.

### 1.1 Ontario's boreal managed forest (MF)

Ontario's boreal forest represents a significant portion of Canada's boreal ecosystem and provides an important case for examining forest recovery across disturbance types. Extending across approximately 45 Mha, the boreal region encompasses nearly half of Ontario's total land area and forms one of the largest contiguous forested landscapes in eastern North America (Thompson et al., 2000; Ouellette et al., 2020). Much of this region falls within the provincial Managed Forest (MF) boundary (Figure 1), where commercial harvesting activities occur alongside conservation mandates and ecosystem-based forest management frameworks (MNRF, 2021).

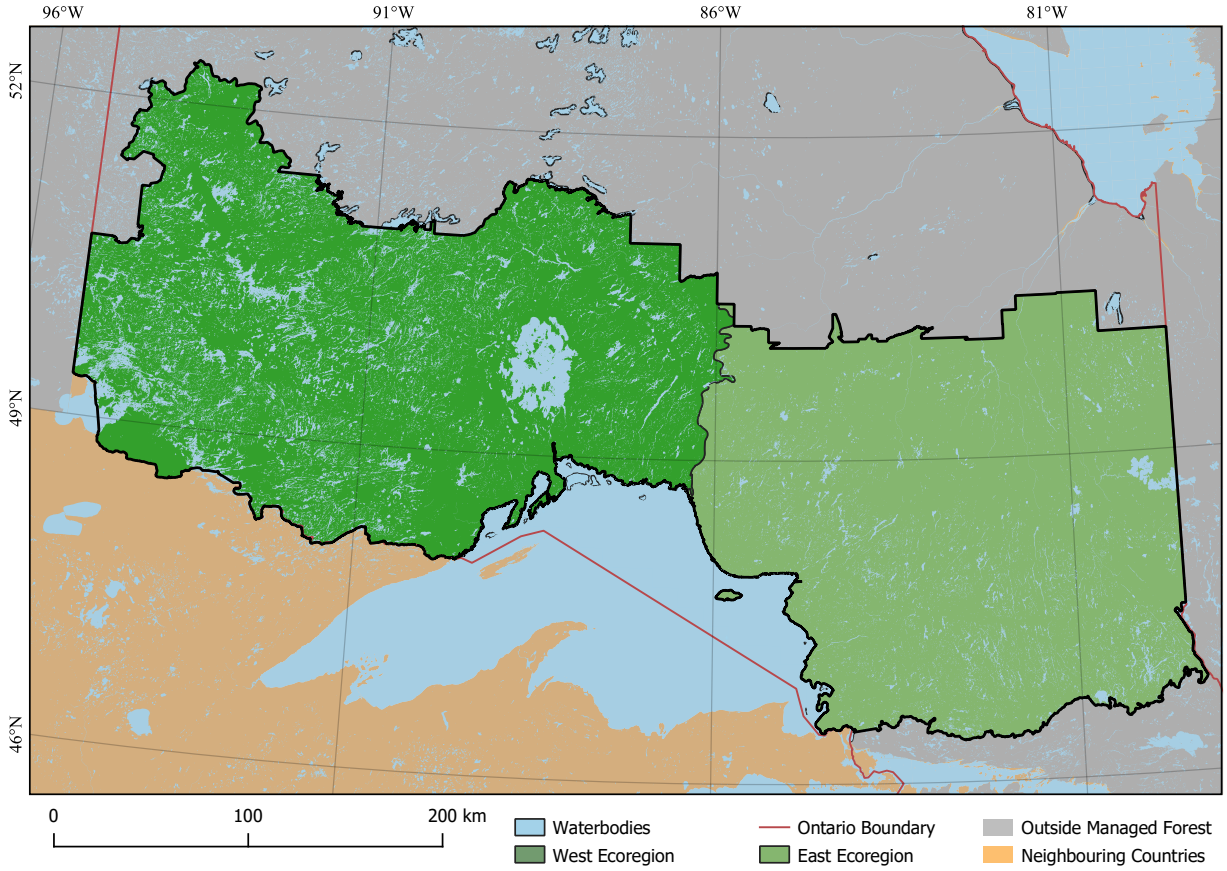


Figure 1. Map of the Ontario managed boreal forest study area showing western (dark green) and eastern (light green) ecoregions, with provincial boundary and major lakes.

Population density across the northern boreal zone remains low, with fewer than one person per square kilometre, and the region is primarily occupied by small communities and Indigenous Nations whose cultural knowledge and land stewardship practices are deeply tied to forest ecosystems (Bergeron & Yves, 2015; Golden et al., 2015; Ahmed et al., 2017). The boreal MF contains roughly two-thirds of Ontario's forest cover, supporting long-term timber supply, economic development, and employment in forest-dependent communities, while simultaneously contributing to provincial biodiversity, habitat networks, and ecosystem function (Robbins, 2007; Mackey et al., 2023).

Forest management in Ontario operates under a balance of ecological, economic, and sustainability objectives (Forest Canada, 1994). Ontario's boreal MF spans multiple ecological regions that differ in climate, soil composition, fire behaviour, and dominant vegetation. The

western boreal region is generally warmer and drier, with coarse-textured glacial deposits that support extensive jack pine and black spruce stands shaped by frequent ignited wildfires. In contrast, eastern regions are cooler and wetter, underlain by glaciolacustrine clays that support mixed wood stands containing trembling aspen, white birch, and balsam fir (Brandt et al., 2013; Hayes et al., 2022). These ecological gradients, defined as systematic spatial changes in climate, soils, vegetation composition, and disturbance regimes, influence disturbance severity, fire return intervals, fuel continuity, and regeneration pathways, making ecoregional variability critical for interpreting structural recovery across disturbance types.

Ontario's boreal forest landscape experiences cyclic disturbances from wildfire, insect outbreaks, windthrow, and industrial activity (Brandt et al., 2013; Girona et al., 2023). Among these, wildfire and clear-cut harvesting represent the most spatially extensive disturbance drivers in the MF. On average, wildfire affects between 3 and 6 Mha of Canadian boreal forest annually, whereas harvesting affects a smaller but ecologically significant portion of forest cover each year (Kurz et al., 2013; Lemprière et al., 2013).

The interaction among ecological processes, management interventions, and disturbance regimes has produced a diverse and dynamic landscape mosaic in which forest stands vary widely in age, structure, and recovery stage. This makes Ontario's boreal MF an ideal setting for investigating how disturbance type and ecological context influence regeneration morphology over time. Also, these boreal ecological characteristics make disturbance-driven regeneration structure a central focus for comparing wildfire and harvesting recovery patterns.

### 1.2 Disturbance regimes: wildfire and forest harvesting

Disturbance is a defining ecological process in the boreal forest, shaping stand composition, age structure, fuel dynamics, and long-term spatial patterning (Bergeron et al., 2004; Bartels et al., 2016; Seidl et al., 2017). Stand-replacing disturbances such as wildfire, insect outbreaks, and large-scale windthrow can reorganize forest structure. In Ontario's Managed Forest, wildfire and forest harvesting represent the most extensive stand-replacing disturbances and the major driver of landscape renewal and structural heterogeneity (Brandt et al., 2013). Although both remove biomass and initiate regeneration, they operate through different mechanisms and residual structures (Bergeron et al., 2017; Seidl & Turner, 2022)

Wildfire removes above-ground biomass through combustion and thermal shock, leaving behind standing deadwood, exposed mineral soils, and a heterogeneous distribution of post-fire residues such as charred stems, seedbanks, and coarse woody debris (Salgado et al., 2024; Vahedifard et al., 2024). Fire behaviour varies with fuel continuity, moisture conditions, weather, and topography, producing a spatial mosaic of burn severities ranging from unburned refugia (Perera & Cui, 2010; Araya et al., 2015) to complete crown combustion (De Groot et al., 2013). In contrast, harvesting removes live biomass mechanically and often results in more abrupt boundaries and straighter edges than those produced by wildfires, reduced deadwood accumulation, and less disruption of the forest floor, which can favour residual species and support different regeneration structures (Arseneault, 2001).

These differences can influence the speed and form of structural recovery. Fire-affected stands are often described as showing rapid vegetation recovery, a pattern that this study evaluates using time-explicit morphological classification, followed by slower phases of structural consolidation as residual trees fall, coarse woody debris accumulates, and vegetation becomes organized into distinct vertical layers through time (Bartels et al., 2016). In contrast, harvested stands may reach vegetation cover or spectral greenness thresholds relatively quickly through planting or uniform regeneration, while the internal structure of the stand develops more gradually where residual structures such as standing dead trees, fallen logs, and undisturbed microsites are limited (Donato et al., 2012) As a result, forest stands originating from wildfire and harvesting may appear similar during early stages of recovery when assessed using surface vegetation indicators, yet differ substantially in their regeneration pattern through time, including differences in disturbance persistence, patch connectivity, and gap retention, as detected by time-explicit morphological classification.

Regeneration trajectories, which are the pathways through which forests reorganize following disturbance, vary with disturbance type, ecological zone, and local environmental conditions such as climate, soils, and pre-disturbance stand composition (Seidl & Turner, 2022). Structural attributes that reflect this reorganization, including vertical layering, spatial continuity of vegetation, and the persistence of internal gaps, often develop more slowly than changes in vegetation greenness captured by spectral indices (Bartels et al., 2016; Banin et al., 2023; White et al., 2023). As disturbance regimes are increasingly influenced by climate-driven changes in

fire behaviour (Halofsky et al., 2020) and by forest management practices that alter disturbance size, frequency, and configuration, the need to quantify post-disturbance forest structure in ways that explicitly represent spatial pattern and can be applied across large landscapes becomes more pressing (OMNR, 2001; Perera & Cui, 2010; Perera et al., 2008; Seidl et al., 2014; Lesmeister et al., 2025). These considerations highlight the origin of disturbance and forest recovery, which shape the forest in distinct and measurable ways.

### 1.3 Post-disturbance regeneration

Post-disturbance regeneration is the process by which forest ecosystems reorganize following a disturbance through the growth and spatial arrangement of new vegetation. Regeneration involves not only the return of plant cover, but also the reformation of forest structure over time as stems establish, layers develop, and patches expand or connect across space. Large disturbances, such as wildfire and forest harvesting, initiate a period of reorganization in which forest structure is rebuilt over time. Following disturbance, regeneration proceeds through a combination of seedling establishment, vegetative reproduction, and competitive interactions that reshape stand composition, spatial pattern, and vertical development (Bergeron et al., 1999; Greene et al., 1999; Kuuluvainen, 2009). While vegetation cover may return relatively quickly, the development of forest structure often unfolds more gradually as stems grow, layers form, and spatial connections emerge within the stand.

Empirical studies show that regeneration trajectories vary widely depending on disturbance origin, ecological setting, and pre-disturbance conditions. Across Canadian forests, recovery rates of canopy cover, height, and basal area differ by biome and ecozone, with boreal stands often requiring a decade or more to develop early structural attributes following disturbance (Bartels et al., 2016). These averages, however, mask substantial spatial variability linked to disturbance severity, substrate conditions, and species composition. As a result, stands that appear similar in age or vegetation cover may differ markedly in internal organization and spatial structure.

Comparative studies in boreal forests suggest that wildfire and harvesting can produce different recovery trajectories. However, most assessments rely on two-dimensional spectral summaries or stand-level indicators and do not evaluate how disturbance states evolve through

time as connected structures. This study extends that understanding by examining regeneration as a time-explicit morphological pattern, allowing disturbance persistence, reconnection, and fragmentation to be measured within a unified 3D voxel framework. Studies comparing young post-fire and post-harvest stands report that harvested areas tend to retain more pre-disturbance tree species and experience less variability in forest-floor disturbance, whereas wildfire more strongly disrupts the organic layer and promotes pioneer species and lichen communities (Harper et al., 2004; Brassard & Chen, 2006). In black spruce–feathermoss forests of Québec, wildfire has been shown to create greater forest-floor disturbance and microsite heterogeneity, At the same time harvested sites maintain more residual vegetation and experience less severe soil disruption (Nguyen-Xuan et al., 2000). These ecological differences are expected to influence how disturbed and recovering patches persist, reconnect, or fragment through time.

At broader spatial scales, review studies across boreal ecozones indicate that fire is stronger driver of forest composition and age structure than logging over large extents and long-time frames (Martin et al., 2020). Harvesting, by contrast, tends to cluster in accessible and commercially valuable areas, producing distinctive spatial patterns of disturbance extent and rotation length. Together, these processes generate mosaics of stands at different recovery stages of recovery. These large-scale disturbance regimes influence how disturbance patches persist, overlap, and reorganize through time, forming landscape patterns that can be evaluated using time-explicit morphological analysis.

Recent research also highlights that regeneration dynamics are being reshaped by climate change and management pressures. Warmer temperatures, longer fire seasons, and altered precipitation regimes have increased fire activity and severity across much of the boreal forest (Bartels et al., 2016). At the same time, forest management policies, including disturbance emulation guidelines and conservation set-asides, are modifying where and how harvesting occurs (Pickell et al., 2013; Acil et al., 2024). These changes raise questions about whether future disturbance regimes will maintain historical structural patterns and whether anthropogenic disturbances can realistically emulate the structural outcomes of natural fire (Kuuluvainen et al., 2021).

Despite strong ecological evidence that the origin of disturbance shapes regeneration pathways, consistently characterizing these differences across landscapes remains challenging.

Structural attributes such as spatial continuity, patch development, and internal gaps often emerge over longer time scales than vegetation presence alone. Tracking how regeneration develops through time, therefore, requires approaches that move beyond cover and describe the evolving form and arrangement of recovering forest structure (Remmel, 2022).

### 1.4 Monitoring post-disturbance recovery

Monitoring post-disturbance regeneration remains a major challenge in boreal forest research, particularly across large and remote landscapes where recovery unfolds over decades. Remote sensing has therefore become the primary tool for assessing disturbance and recovery at broad spatial scales, providing repeatable observations through time that are not feasible through field-based monitoring alone (Ahmed et al., 2017; White et al., 2022; Birch et al., 2025).

Most large-scale monitoring approaches rely on spectral vegetation indices, such as the Normalized Difference Vegetation Index (NDVI)(Rouse et al., 1974; Bonannella et al., 2022; Celebrezze et al., 2024; Birch et al., 2025), which summarizes vegetation greenness and related photosynthetic activity using satellite reflectance data. These indices are effective for detecting disturbance and identifying the return of vegetation cover. However, they typically evaluate each year independently and provide limited insight into how disturbance states persist, reconnect, or fragment through time.

Time-series methods have improved the ability to track recovery trajectories (Banskota et al., 2014; Ahmed et al., 2017) by analyzing spectral change over multiple years. Approaches such as LandTrendr and Composite2Change can identify disturbance timing, magnitude, and general recovery trends across landscapes (Kennedy et al., 2010; Hermosilla et al., 2015, 2016; Pasquarella et al., 2022; He et al., 2024). Yet these methods largely represent recovery as a return toward pre-disturbance spectral conditions. Because spectral indices often saturate at moderate biomass levels, they may indicate recovery even when disturbance states continue to reorganize through time (Wulder et al., 2012; Bartels et al., 2016).

Three-dimensional remote sensing approaches, including LiDAR (Baltsavias, 1999) and photogrammetric point clouds (Westoby et al., 2012), provide detailed information on canopy height and vertical layering (Tompalski et al., 2021). These datasets offer important insight into forest structural attributes, but they are often spatially incomplete or lack consistent temporal

coverage across long monitoring periods. As a result, long-term recovery studies across large regions frequently rely on multi-year spectral products. Rather than reconstructing vertical canopy structure, this study integrates annual disturbance classifications into a stacked temporal sequence to evaluate regeneration as a connected disturbance-state pattern.

### 1.5 Limits to approaches in monitoring forest recovery

Despite these advances in forest recovery monitoring, important limitations remain in detecting patterns of structural recovery. Remote sensing approaches to forest disturbance and recovery have advanced substantially, with increasing emphasis on describing forest structure and spatial configuration rather than vegetation presence alone (Remmel & Csillag, 2003; Remmel, 2020). Recovery is now understood not only as the return of canopy greenness but also as a process in which structural patterns reorganize across space and time, and spatial features such as gaps, edges, and connectivity evolve after disturbance (Seidl et al., 2020; Seidl & Turner, 2022). Structural measures, therefore, provide important insights into habitat formation, carbon storage, and ecosystem resilience when comparing post-disturbance recovery across disturbance types (Zhang et al., 2025).

Three-dimensional approaches, including LiDAR and structure-from-motion photogrammetry, have strengthened structural analysis by measuring canopy height, vertical layering, and gap structure rather than reflectance alone (Pascual et al., 2010; Tompalski et al., 2021). These data can distinguish disturbance severity and reveal structural differences between burned and harvested stands, even after spectral signals converge (Vogelmann et al., 2016; García et al., 2020). However, such datasets are often spatially incomplete and collected irregularly in time, limiting their ability to provide consistent annual coverage across broad managed landscapes.

To address these limitations, some studies derive structural proxies from satellite time series using patch configuration and fragmentation metrics, such as those implemented in FRAGSTATS, where direct three-dimensional data are unavailable (McGarigal & Marks, 1995; Hermosilla et al., 2015; Ahmed et al., 2017). These approaches demonstrate that spectral recovery does not always correspond to changes in landscape configuration. However, such

analyses typically evaluate configurations within individual temporal layers or compare metrics across years, rather than embedding the full temporal sequence within a unified analytical framework.

Multi-year Landsat imagery is widely used to detect disturbance timing, magnitude, and vegetation regrowth trajectories across large regions (Kennedy et al., 2010; Hermosilla et al., 2016; Ahmed et al., 2017; Bonannella et al., 2022). Most of these methods rely on spectral indices and trajectory models that summarize greenness and spectral change through time (Cohen & Goward, 2004; Banskota et al., 2014; Birch et al., 2025). While effective for detecting disturbance and regrowth signals, they provide limited information about the spatial configuration and internal organization of regenerating forest structure. Spectral recovery indicates that vegetation has returned, but it does not reveal how forest structure is organized. As a result, wildfire and harvested stands may appear similar in recovery rate when evaluated spectrally, even when their spatial pattern and internal structures may differ in ecologically meaningful ways (Bartels et al., 2016; McRae et al., 2001; White et al., 2022).

Although Landsat time series is widely used for disturbance and recovery monitoring, it has rarely been applied from a morphological perspective that explicitly represents spatial organization through time. In particular, voxel-based morphological segmentation frameworks have not yet been widely applied to multi-year Landsat stacks to quantify how forest structure develops after wildfire and harvesting (Remmel, 2022). The framework implemented in this study addresses this need by applying Landsat time series within a voxel-based morphological analysis to compare structural regeneration patterns between disturbance types (fire and harvesting). This gap creates the need for a framework that represents recovery as a connected spatio-temporal structure rather than as independent yearly maps.

### 1.6 Morphological segmentation in landscape ecology

Segmentation offers an alternative representation of spatial patterns that directly addresses these limitations. Rather than treating a landscape as a collection of independent pixels, segmentation groups spatially connected elements into contiguous regions with shared characteristics (Soille, 2004). Morphological segmentation extends this logic by classifying pixels based on their spatial relationships, thereby enabling the explicit distinction of interior,

edge, connected, and isolated structures. In two dimensions, Morphological Spatial Pattern Analysis (MSPA) operationalizes this approach by segmenting a binary map into mutually exclusive structural classes, including Background, Core, Edge, Islet, Branch, Loop, Bridge, Perforation, and Core-opening (Soille & Vogt, 2009). These classes shift analysis away from abstract indices toward spatially interpretable components that explicitly represent structural roles within the landscape.

A useful starting point for structuring landscapes in this context is the binary representation of space. Any landscape can be expressed as two classes: a foreground, representing a feature of interest, and a background, representing its absence (Figure 2). This binary form is typically encoded as a grid of 1s and 0s. The same landscape can be classified in different ways depending on the phenomenon being foregrounded, such as disturbance versus no disturbance, forest versus non-forest, or vegetation versus bare ground. Once defined, this binary structure becomes the input for morphological segmentation.

The foreground area of a binary image can be classified into seven uniquely defined morphological MSPA classes: (1) Core is the interior area excluding a perimeter and the foreground pixels that are distant from the background by a distance greater than a given edge width, (2) Edge cells form interfaces at the outer margin of a core with the background cells, (3) Islets are clusters of foreground cells that are too small to contain Core and Edge cells, (4) Loops are connected cells that connect a core back to itself, forming a closed shape, which helps reinforce the overall connectivity within that area of the image, (5) Bridges are connected cells that join distinct areas of core cells, (6) Perforation cells form interfaces that are holes within a core area, and morphological class, (7) Branch cells are protrusions from a core that are not connected at the protruding end and are not wide enough to contain both Edge and Core. The classification of and Edge pixel types is essential for delineating transitions between foreground and background cells within the binary image.

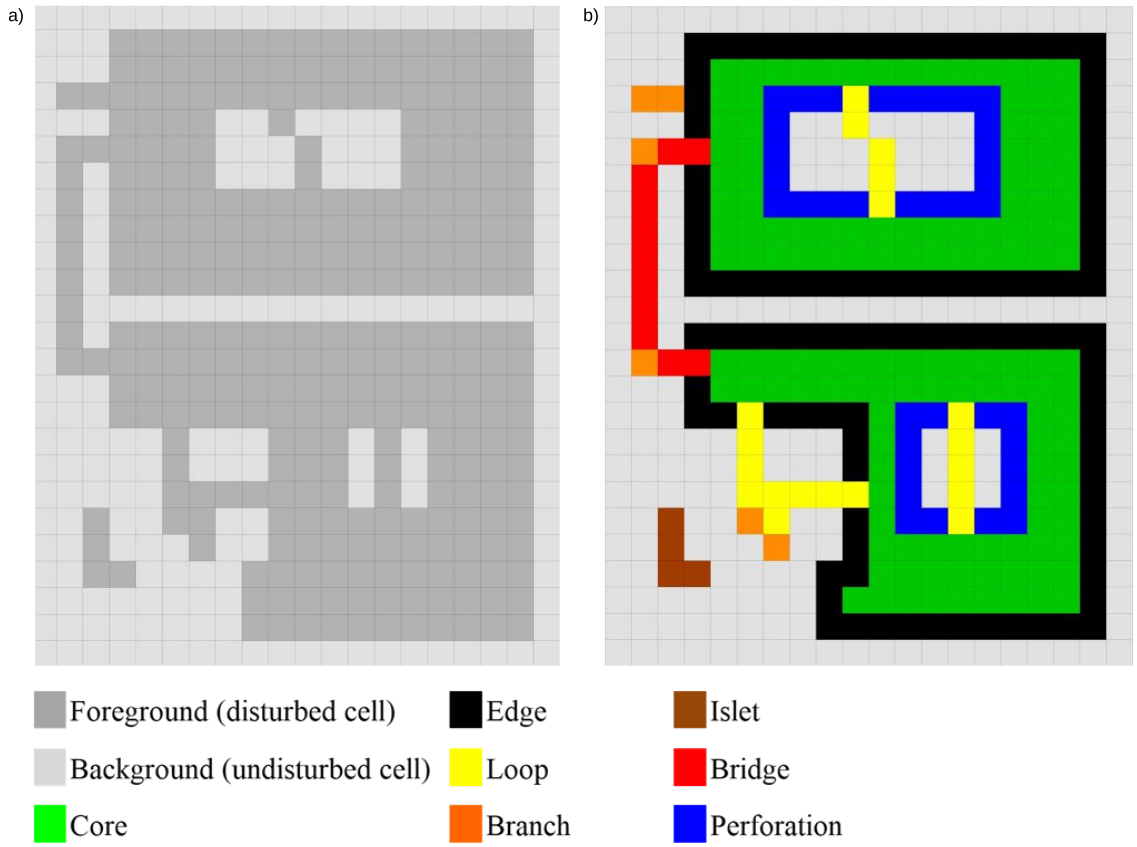


Figure 2. A binary image of disturbed and undisturbed cells (a) and its 2D morphological segmentation into the seven mutually exclusive morphological classes and the background class (b), using a Rook's case neighbourhood structure in which cells are connected only when they share an edge.

Morphological Spatial Pattern Analysis (MSPA) at the landscape level (Soille & Vogt, 2009, 2022) is useful for identifying several aspects of morphology and offers a systematic investigation of each cell's impact on the overall structure of an object represented by the foreground cells in an image; in this study, this characterizes the morphological structure of the boreal forest at a given instance in time. MSPA performs a 2D segmentation of a binary landscape into its morphologic elements, which, for images of forest disturbance, provide summaries of structure on a horizontal plane. MSPA focuses on the form and connectivity of landcover classes and provides a theoretical framework for analyzing the spatial structure of a landscape (Riitters et al., 2009; Soille & Vogt, 2009).

Most existing landscape metrics describe spatial patterns in two dimensions and are evaluated at single time steps. Post-disturbance recovery, however, unfolds over multiple years. Representing time as an explicit analytical dimension enables recovery to be analyzed as a continuous structural process rather than as a sequence of independent maps (Remmel, 2022). Also, because configuration focuses on how landscape elements are arranged and connected, methods are required to make these structural relationships comparable over time and to compare them as recovery unfolds.

In this thesis, 3D does not refer to physical forest height or volumetric canopy structure (*x, y, z*). Instead, it refers to a space–time cube (*x, y, t*) created by stacking annual disturbance classifications through time. Each voxel represents a spatial cell at a specific year and is classified as disturbed or undisturbed based on the vegetation index threshold. Morphological segmentation is applied to this space–time cube to classify voxels according to their spatial and temporal connectivity and structural role. The resulting morphological classes describe how disturbed areas persist, contract, fragment, reconnect, or become enclosed over time as regeneration progresses. The method therefore characterizes spatiotemporal disturbance and recovery patterns rather than vertical forest structure, such as canopy height, layering, or biomass distribution.

Advancements in 3D measurements have expanded the possibilities in the field of geospatial analysis in ecology and geography (Dandois & Ellis, 2013). Recently, two-dimensional morphological segmentation concepts have been extended into the third dimension, enabling segmentation of three-dimensional binary voxel arrays into their respective morphological classes (Remmel, 2022). Voxels are volumetric pixels representing discrete units within a three-dimensional array. Definitions of existing 2D morphologic classes have been extended to the 3D reality of voxels and given new names to distinguish whether 2D or 3D morphology that is being addressed. Table 1 summarizes the corresponding names of the 3D class extensions from the 2D case. For example, Core becomes MASS, Edge becomes SKIN, and small isolated patches become CRUMB. At the same time additional classes capture spatial elements unique to volumetric environments, including ANTENNA, CIRCUIT, BOND, VOID, and VOID-VOLUME (VVOL). Three-dimensional morphological segmentation generalizes

MSPA logic to voxel arrays (Remmel, 2022), assigning each voxel to a structural role based on its connectivity to neighbouring voxels.

Table 1. The comparative analysis of the 2D and 3D morphological classification.

| Class | 2D Morphological Class | 3D Morphological Class |
|---|---|---|
| 1 | Background | OUTSIDE |
| 2 | Core | MASS |
| 3 | Edge | SKIN |
| 4 | Islet | CRUMB |
| 5 | Branch | ANTENNA |
| 6 | Loop | CIRCUIT |
| 7 | Bridge | BOND |
| 8 | Perforation | VOID |
| 9 | Core-Opening | VOID-VOLUME |

Annual binary maps are stacked to form a voxel cube representing disturbance and recovery as a temporal structure. This allows regeneration to be interpreted through its evolving spatial connectivity: interior recovery may form MASS, expanding edges may appear as SKIN, isolated recolonization may register as CRUMB, and temporal pathways or connections may emerge as BOND or CIRCUIT, as all are defined in Table 2.

This shift enables recovery to be analyzed as a continuous structural process rather than as independent yearly maps. Instead of asking whether vegetation has returned, voxel-based morphological segmentation enables recovery to be described in terms of structural organization. Whether it forms a cohesive interior, spreads from edges, fragments into disconnected components, or develops stable connectivity. This concept motivates the voxel-based workflow used in Sections 2, where Landsat-derived binary time series are stacked into voxel cubes and segmented into 3D morphological classes.

Table 2: Definitions of 3D morphological classes used in voxel-based segmentation.

| Class | 3D Morph Classes | Morphological Meaning |
|---|---|---|
| 1 | OUTSIDE | Voxels that do not belong to the feature of interest (coded as 0 in the binary cube). These represent the background surrounding the object being analyzed. |
| 2 | MASS | Interior voxels that are surrounded on all six sides by neighbouring feature voxels. These represent the core of a 3D object. |
| 3 | SKIN | Voxels that neighbour MASS voxels and form the external surface of the object. They are adjacent to MASS but exposed to outside space. |
| 4 | CRUMB | Small discrete voxel clusters that contain no MASS voxels and do not connect to larger voxels. |
| 5 | CIRCUIT | Connector voxels that link a MASS back to itself, forming a closed loop within the structure. |
| 6 | ANTENNA | Connector voxels that extend outward from a MASS but connect to it at only a single point. These represent protrusions from the object. |
| 7 | BOND | Connector voxels that link two or more separate MASS clusters within the object of interest. |
| 8 | VOID- VOLUME | Voxels representing the fully enclosed empty space (i.e., the voxels assigned 0) inside the feature of interest. It is also called the interior hole. |
| 9 | VOID | Voxels representing the internal boundary of an empty space located inside the object. These are internal edges surrounding holes within the structure. These voxels surround the VOID-VOLUME. |

### 1.7 Research objectives and questions

This research tests whether boreal forest stands disturbed by wildfire recover differently from those disturbed by forest harvesting, specifically in terms of their time-explicit morphological organization. The framework is applied to classified satellite images that represent annual disturbance states. By stacking these annual layers into a unified analytical volume in which time forms the third dimension, regeneration is evaluated as a connected disturbance-state structure rather than as a measure of canopy height or vertical forest architecture. Accordingly, this research has two objectives.

First, this research comprises two phases (*Phase-1* and *Phase-2*). The first is to translate the existing R-based *morph* package (Remmel, 2022) into a Python library, enabling more

efficient processing of large spatial datasets, and the Second is to implement this framework on time-series satellite data to evaluate whether boreal forests disturbed by wildfire and harvesting exhibit differences in structural regeneration patterns when recovery is examined as a space-time process. Together, these objectives support the development of both a methodological contribution and an applied case study examining disturbance-driven regeneration trajectories in Ontario's managed boreal forest.

Understanding the regeneration structure of the boreal forest after a disturbance is important for forest management (Blanco et al., 2009; Schroeder et al., 2011) and guided by current challenges in landscape monitoring and disturbance ecology, this research addresses the following questions:

1. Do boreal forest stands disturbed by wildfire and harvesting differ in their regeneration structure when examined through a voxel-based, time-explicit framework? This question is addressed by testing whether the proportions of space–time morphological classes computed from voxel-based segmentation of annual disturbance layers differ significantly between wildfire and harvesting sites and between eastern and western ecoregions within the Ontario MF. These class proportions are derived from stacked (*x, y, t*) disturbance classifications, where the third dimension represents time. Differences in disturbance type and regional environmental conditions are expected to produce distinct regeneration patterns, reflected in morphological class proportions.

2. Are structural regeneration patterns consistent within disturbance types and across ecological regions in boreal Ontario? Here, I will test whether the proportions of 3D morphological classes computed for a sample of wildfire and harvesting disturbances differ significantly across disturbance types and between east and west ecoregions within the province. I expect that disturbance type and regional environmental conditions will produce distinct regeneration patterns, which will be reflected in the proportions of morphological classes.

3. Does incorporating time as an explicit third dimension improve the interpretation of post-disturbance recovery compared to two-dimensional spectral approaches? This analysis compares pattern measures derived from time-explicit voxel-based morphological

segmentation with those derived from single-year or two-dimensional spectral summaries. The comparison examines whether the time-stacked (*x, y, t*) framework better identifies patterns of persistence, fragmentation, reconnection, and re-disturbance over time. It is expected that the time-explicit framework will provide a clearer interpretation of regeneration dynamics than two-dimensional spectral measures alone.

These questions explore how disturbance mechanisms and ecological context influence the form, organization, and progression of recovery after disturbance, rather than whether vegetation simply returns. These questions position recovery as a structural process through time rather than a simple return of vegetation. The following sections, therefore, examine how post-disturbance regeneration unfolds, how recovery has been monitored at the landscape scale, and why existing approaches remain limited for comparing wildfire and harvest recovery over time.

# 2 Methodology

## 2.1 Study design overview

This chapter explains how the study was carried out. The method used in this research is organized into two main phases:

1. *Phase-1*: Code translation
2. *Phase-2*: Temporal morphological pattern comparison between wildfire and harvesting regeneration

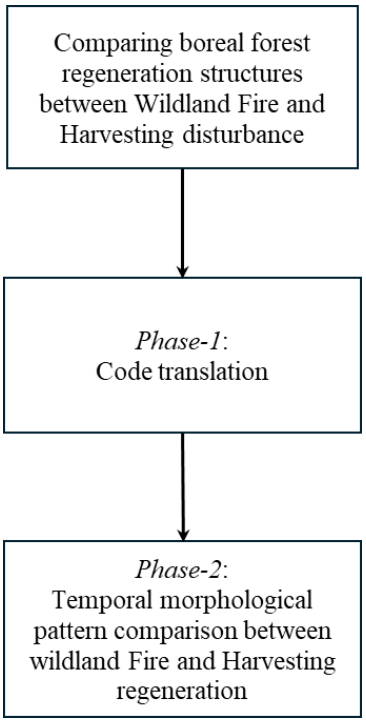


Figure 3. A flow chart showing the research phases.

In this research, *Phase-1* provides a methodological tool that enables three-dimensional segmentation of binary disturbance time-series data. *Phase-2* uses that tool to ask whether wildfire and harvesting produce different structural trajectories in Ontario's managed boreal forest.

## 2.2 *Phase-1*: code translation

*Phase-1* of this research focused on the development of *morphpy*, a Python-based translation and expansion of the original R 'morph' package (Remmel, 2022). The original R

implementation demonstrated that morphological segmentation could be applied to binary voxel datasets to identify structural patterns using graph theory and three-dimensional connectivity rules. Its analytical strength lay in its ability to assign mutually exclusive morphological classes to spatially connected voxel elements. However, the R implementation was limited in its ability to handle larger datasets. The reliance on memory-heavy arrays and the use of *igraph* (Csardi & Nepusz, 2005). For connectivity construction, the translation of the package was intensified, particularly voxel cubes derived from multi-year remote sensing inputs. During early testing, it became evident that the R version could not handle a large amount of data without crashing, exhausting memory. These limitations necessitated translation before applying the method to the scale of disturbance and recovery patterns observed across the Ontario-managed boreal forest.

The foundational principle guiding this phase is the MSPA (Soille & Vogt, 2009) a framework, which is extended into three dimensions (Remmel, 2022). Instead of classifying pixels, the approach assigns roles to voxels, treating them as spatial units with measurable adjacency in six directions. The nine morphological classes OUTSIDE, MASS, SKIN, CRUMB, ANTENNA, CIRCUIT, BOND, VOID, and VOID-VOLUME provide a structured vocabulary for describing the spatial and temporal behaviour of disturbance and regeneration patterns. These classes capture distinctions that binary maps cannot convey, whether disturbance becomes consolidated into core mass, fragments into isolated units, stretches into branching or looping tendrils, or encloses internal empty spaces. When applied to NDVI-derived voxel cubes, the method treats regeneration as a dynamic structure evolving over time rather than as static, independent maps.

To enable the application of this framework to large voxel datasets derived from multi-year remote sensing imagery, the original R-based morph framework (Remmel, 2022) was translated to Python and implemented as a custom package called *morphpy*. This translation preserves the conceptual and analytical logic of the original method while allowing more efficient processing of large three-dimensional arrays and graph-based connectivity structures required for voxel segmentation. The Python implementation also facilitates integration with the geospatial data processing workflows used in this study.

The design of *morphpy* retained the core conceptual logic of the R ‘morph’ package's original method while adopting a modular architecture better suited to extension and reproducibility. The segmentation routine centres on a single function, `morph3d()`, which accepts a binary 3D NumPy array representing the voxel cube. In this study, each cube consisted

of stacked disturbance/undisturbed states derived from annual NDVI thresholds across multiple years. The *x* and *y* axes represented space, while the *z*-axis represented time. The segmentation begins with validation of 3D binary data, assignment of unique voxel identifiers, padding of cube boundaries to avoid edge misclassification, and construction of voxel adjacency by shifting the ID grid in six spatial directions. This adjacency structure is converted into an edge list and stored as a NetworkX graph, with each voxel as a node connected to its orthogonal neighbours.

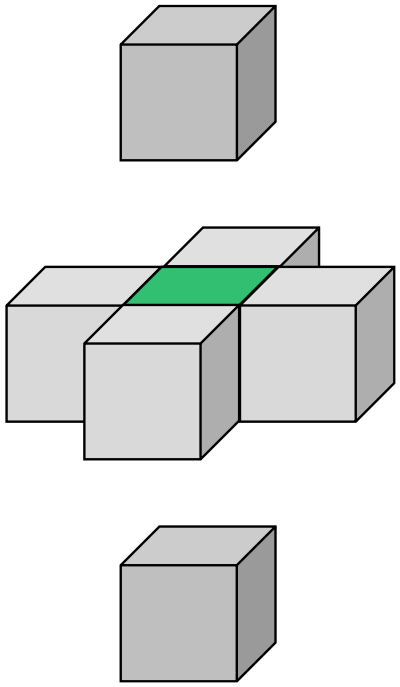

Figure 4. Conceptual illustration of 3D voxel adjacency and orthogonal neighbour connectivity used in morphological segmentation. The central voxel (green = MASS) is connected to its six face-sharing neighbours in the *x, y, and t* (time) directions (grey = SKIN), which form the adjacency structure.

Morphological classification follows a hierarchical logic. MASS voxels are identified first as those with six neighbouring disturbed voxels. SKIN voxels are then identified as those directly adjacent to MASS. CRUMB objects, small clusters with no internal (MASS) or surface (SKIN) structure, are assigned next. Remaining voxels are treated as connectors and refined into ANTENNA, CIRCUIT, or BOND classes based on their relationship to MASS clusters. Internal empty spaces are identified using a flood-fill algorithm applied to background voxels, distinguishing outer background from enclosed voids, which are then labelled as VOID-VOLUME and their inner boundaries labelled VOID. The output is a fully classified 3D voxel

structure in which each voxel is assigned a unique morphological code. A detailed development note and Python script for *morphpy* 3D morphological segmentation are provided in Appendix A and Appendix B

The implementation produces multiple complementary outputs: a *morphCode* cube (a three-dimensional labelled array in which each voxel is assigned a morphological class code), summary tables of voxel counts and percentage by morphological class, three-dimensional object identifiers that delineate discrete space–time structures, and optional diagnostic visualizations generated using Matplotlib (Hunter, 2007) and Plotly (Plotly Technologies Inc, 2015). These outputs are structured to support reproducibility and consistent comparison across disturbance sites and disturbance types, enabling efficient aggregation, comparison, and statistical testing.

Validation occurred at multiple stages. Synthetic voxel cubes were used early in development to test whether the logic performed predictably in idealized structural arrangements. Real datasets were then processed and visually examined using interactive 3D renderings to assess whether segmentation results aligned with expected disturbance shapes and ecological interpretation. Where possible, segmentation outputs were compared with those generated using the original R implementation. However, exact numerical equivalence is expected due to similarities in the segmentation process and flood-fill logic. The agreement in the overall class proportions and structure confirmed that methodological integrity was preserved.

Beyond translation, the development of *morphpy* represents a novel methodological contribution to remote sensing and landscape ecology. The original morph framework was designed for time-series remote sensing datasets but was constrained by software performance. *morphpy* extends the method to enable the structural evaluation of ecological patterns rather than descriptively or spectrally. Treating time as a formal dimension provides a representation of forest change in which fragmentation, reconnection, consolidation, collapse, and expansion are measurable morphological phenomena.

*morphpy* therefore served as the analytical model for the remainder of this research. The segmentation outputs generated in *Phase-1* serve as the core data inputs for *Phase-2*, in which voxel-level morphological patterns are compared between wildfire and harvesting disturbance types and across ecoregions. In this way, the translation step was not only a technical prerequisite but a foundational development that enabled this research to move beyond pixel-wise change detection toward structural interpretation of post-disturbance ecological processes.

The Full explanation notes of the *morphpy* supporting code (utils) are provided in Appendix C Having established a computational framework that represents regeneration as a three-dimensional structural process, the next phase applies this approach to empirical disturbance data. By analyzing wildfire- and harvest-affected sites across Ontario's managed boreal forest, this study evaluates whether differences in disturbance mechanisms are reflected in distinct structural regeneration trajectories.

### 2.3 *Phase-2*: Study site sample and NDVI processing

This phase of the research investigates the regeneration structure of boreal forests following two major disturbance types, wildfire and clear-cut harvesting, using annual NDVI time-series data to assess post-disturbance recovery through morphological segmentation. The objective is to analyze and compare structural regeneration patterns using the *morphpy* segmentation algorithm on 3D binary data derived from Landsat imagery. For each disturbance site, these data form a voxel cube representing annual time slices of disturbance presence or absence across an eleven-year period.

The study focuses on 30 boreal forest disturbance sites, evenly divided between 15 wildfire and 15 harvesting events. Each site (Figure 5) was randomly selected from within Ontario's MF region from the Ontario Boreal Disturbance Database (*BorealDB*)[1] (Ouellette et al., 2020), with an emphasis on representing both eastern and western boreal ecoregions. For identification throughout the thesis, each site was assigned an alphanumeric code: FS denotes wildfire sites, HS denotes harvesting sites, and the accompanying number identifies the individual site (e.g., FS01, HS01). *BorealDB* contains mapped point records of historical wildfire and harvesting disturbances, including the recorded disturbance year and confidence values for disturbance type. Each point represents a disturbance location and includes attributes indicating whether the event was classified as fire or harvest.

[1] https://www.borealdb.ca/

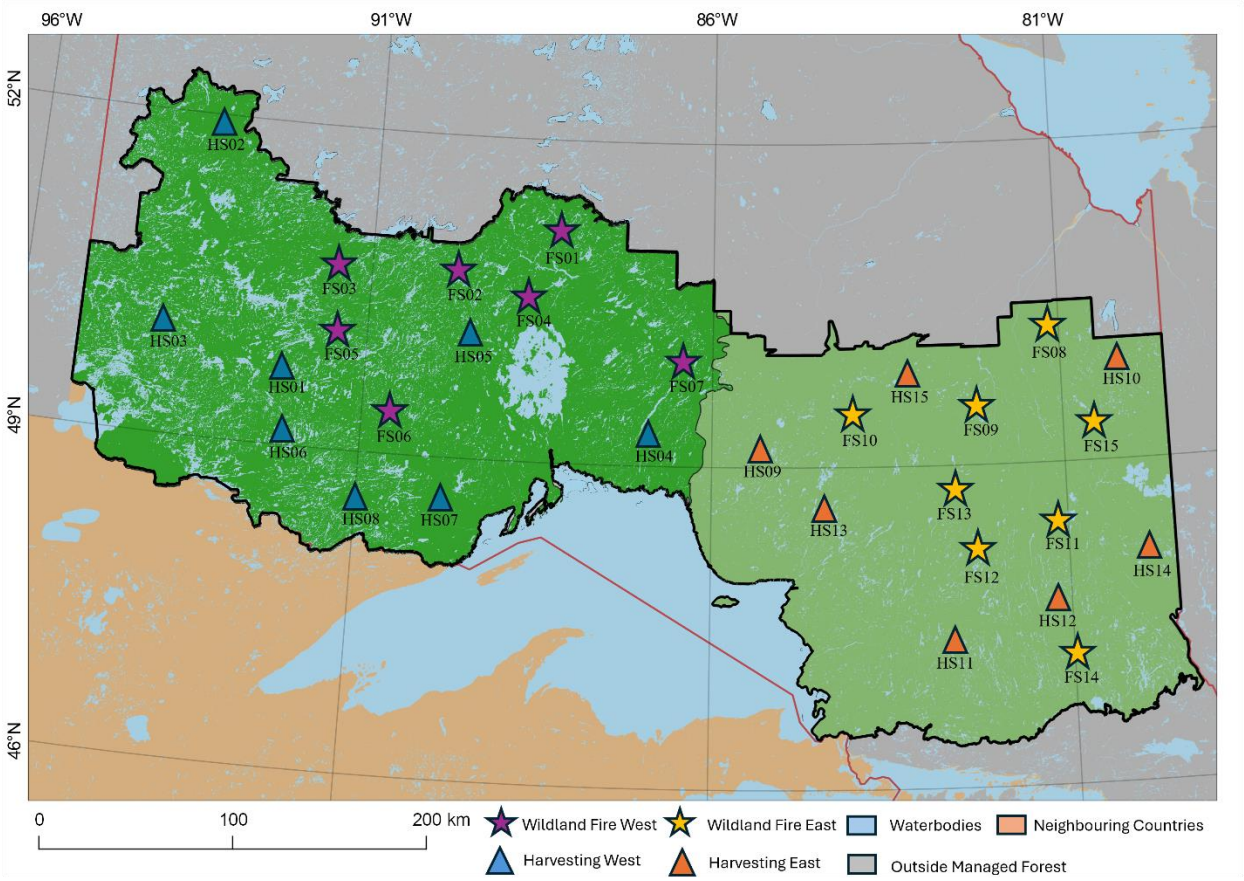


Figure 5. Locations of selected wildfire and harvesting disturbance sites across Ontario's Managed Forest, grouped by eastern and western ecoregions. Alphanumeric labels identify individual study sites: FS = wildfire site, HS = harvesting site, and the accompanying number denotes the unique site identification code.

The study sites were selected using the disturbance code, fire confidence, and harvest confidence fields in *BorealDB* (Ouellette et al., 2020). The disturbance code field was first used to identify disturbance type and timing, where current year fire disturbances were coded as `(1)`, current year harvest disturbances as `(10)`, fire disturbances within the previous two years as `(100)`, and harvest disturbances within the previous two years as `(1000)`. The fire confidence and harvest confidence fields were then used to assess the reliability of these classifications. These confidence values represent the percentage agreement among multiple disturbance data products available for a given location and year. In *BorealDB*, disturbance classifications from Landsat-derived products and additional disturbance datasets from Natural Resources Canada (NRCan), Aviation, Forest Fire and Emergency Services (AFFES), and the Ontario Ministry of Natural Resources and Forestry (MNRF) were compared, and confidence was calculated as a

weighted proportion of sources identifying the same disturbance class. Because the number of available input datasets varies by year, possible confidence values also vary among annual layers. For example, where three products were available, confidence values of 33%, 67%, and 100% indicate agreement by one, two, or all three products, respectively, whereas where four products were available, possible values include 25%, 50%, 75%, and 100%. Higher confidence values therefore indicate stronger multi-source agreement that a disturbance occurred at that location, whereas lower values indicate greater classification uncertainty. Separate fire confidence and harvest confidence fields were used to distinguish support for each disturbance type. Only disturbance points with high confidence values for a single disturbance type were retained to reduce uncertainty and ensure that selected study sites were based on the most reliable disturbance records. This step reduced the likelihood of including sites where the disturbance type was uncertain or where multiple disturbance signals overlapped (Remmel et al., 2023; Wu et al., 2025).

Wildfire and harvesting sites were selected separately to maintain a clear distinction between disturbance origins. For each selected site, the disturbance year was defined as the first recorded disturbance year for that location in the database. This year served as the reference year for the recovery analysis. One year before the recorded disturbance year was included to represent the pre-disturbance vegetation condition. The years following the disturbance were treated as recovery years. An eleven-year time window was constructed for each site, consisting of one pre-disturbance year, the disturbance year itself, and the subsequent recovery years. This fixed study period enabled consistent comparison of regeneration patterns across sites, disturbance types, and ecoregions.

This spatial stratification ensures that the analysis captures not only differences between disturbance types, but also ecological variability associated with geographic location. While the original proposal envisaged a broader temporal span (1972–2021), this thesis narrows the scope to a controlled 11-year monitoring window (1990–2000) to maintain data consistency and ensure computational feasibility during segmentation. For each selected disturbance site, a time series of 11 consecutive years of NDVI data was compiled, beginning in the year of disturbance. These annual time slices were derived from Landsat 5 TM and Landsat 7 ETM+ Collection 2 Level-2 surface reflectance products accessed via the Google Earth Engine (GEE) platform. Annual NDVI was calculated using the standard formula (Rouse. et al., 1974):

$$NDVI = \frac{NIR - RED}{NIR + RED} \quad (1)$$

where NIR corresponds to Band 4 and RED to Band 3 for Landsat 5 and 7. For each year, all available scenes between 1 April and 30 October were filtered by spatial extent and screened using QA_PIXEL cloud, cirrus, shadow, and atmospheric opacity masks. Remaining cloud-free observations were aggregated into a single annual composite using a pixel-wise mean reflectance reducer. NDVI was subsequently computed from this growing season mean composite, yielding one NDVI raster per year. The resulting 11 annual rasters were stacked sequentially to represent the temporal ($t$) dimension of the $x$,$y$,$t$ voxel structure.

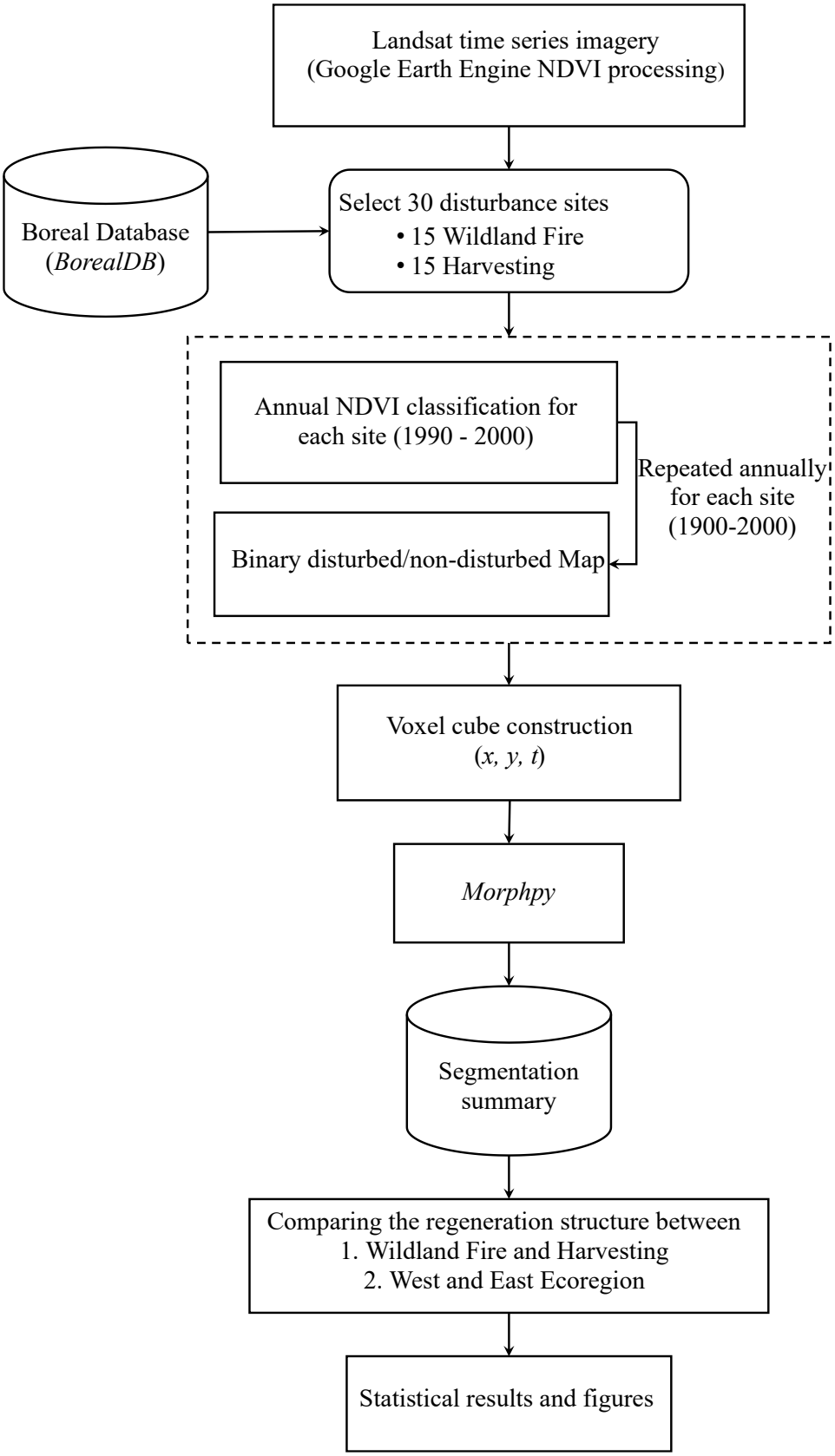


Figure 6. Conceptual flow diagram showing the processing steps of time-series image processing for temporal 3D morphological segmentation.

### 2.4 Binary classification and voxel cube construction

Annual NDVI composites were generated in Google Earth Engine (GEE) using a custom script (Gorelick et al., 2017) to automate the filtering, masking, and compositing of Landsat 5 surface reflectance imagery. The workflow applied pixel-level cloud and shadow masking, followed by a water mask using a reference boundary shapefile of Ontario's managed forests. Multispectral bands were rescaled to top-of-atmosphere reflectance values and thresholder to remove extreme outliers, while thermal bands were processed to exclude anomalously high or low surface temperatures. NDVI was calculated from growing-season imagery (May–September), with all processing steps performed in GEE to ensure scalability and spatial consistency across sites and years.

For each year between 1990 and 2000, site-level NDVI composites were exported to Google Drive as GeoTIFF rasters and imported into ArcGIS Pro for classification. An NDVI threshold of 0.5 was applied uniformly across all sites and years to delineate disturbed (1) from undisturbed (0) conditions, as this value provided a consistent separation between lower NDVI values associated with disturbed or sparsely vegetated areas and higher NDVI values associated with more established vegetation across the annual distributions. Each NDVI raster was reclassified into a binary map using ArcGIS Pro's reclassification tools and clipped to the spatial footprint of the disturbance site to maintain alignment across years. Following reclassification, the 11 annual binary rasters for each site were stacked chronologically to form a three-dimensional voxel cube. The $x$ and $y$ dimensions represent the spatial grid of the site-level rasters, while the third dimension represents time ($t$). Each voxel corresponds to a single 30 m × 30 m pixel for a specific year and records each "voxel" status as either 1 (disturbed) or 0 (undisturbed), as shown in Figure 7. Because disturbance sizes varied across sites, the spatial extent of each voxel cube differed accordingly, whereas temporal depth was standardized to eleven annual slices per site.

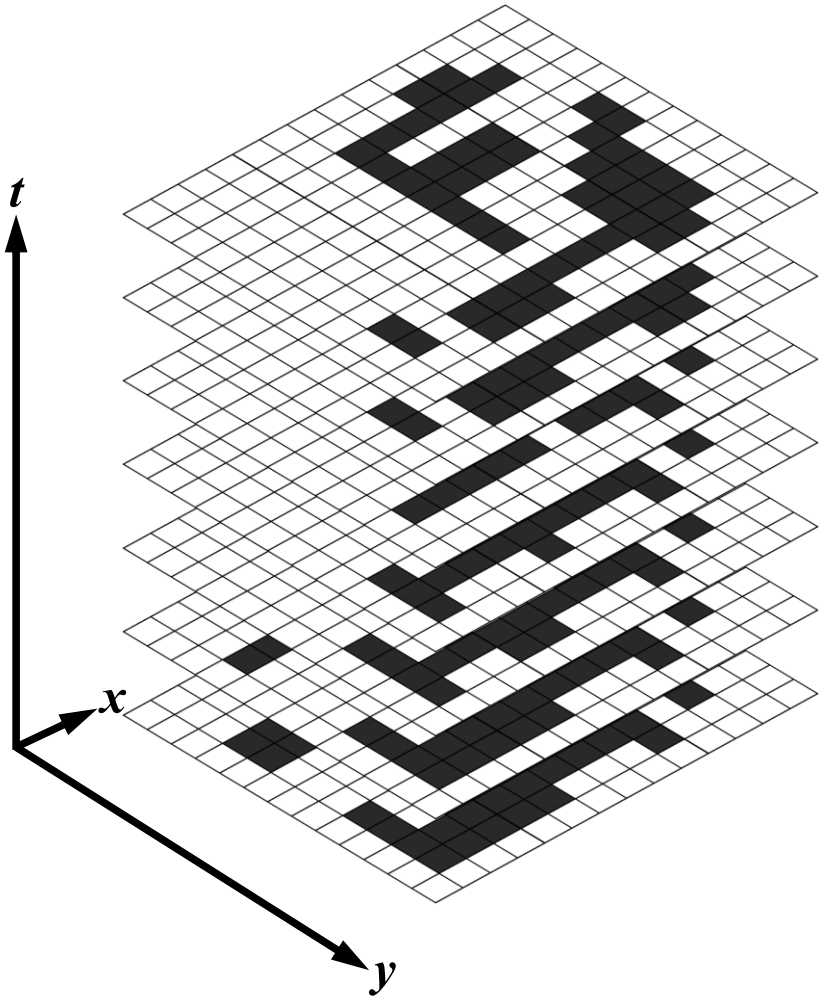


Figure 7. Conceptual representation of the space–time (*x,y,t*) voxel cube constructed from annual NDVI composites. dark cells indicate disturbed, while light cells represent undisturbed conditions. Each horizontal layer corresponds to one annual NDVI composite, and vertical stacking represents time (*t*).

The voxel cube representation used in this study differs from that used in typical remote sensing time-series analyses. In typical temporal analyses, pixels are treated independently, and spectral values are examined through time for each spatial location, evaluating transitions year by year. In contrast, the voxel cube treats time as a structural dimension alongside spatial coordinates, forming a three-dimensional cube of voxels. Morphological segmentation is then applied to this voxel cube to evaluate connectivity among voxels across both space and time simultaneously. As a result, the analysis identifies continuous spatio-temporal structures rather than tracking independent pixel transitions between years.

This stacking process transformed annual two-dimensional NDVI-based disturbance maps into a connected space–time volume that represents post-disturbance change across years (Figure 8). The resulting voxel cubes served as input to the *morphpy* `morph3d()` function, which classified voxels into morphological classes based on three-dimensional connectivity and structural role over time. These classifications form the basis for identifying MASS cores, SKIN layers, CRUMB elements, and dynamic connectors such as ANTENNA and BOND within the evolving regeneration structure of the boreal forest.

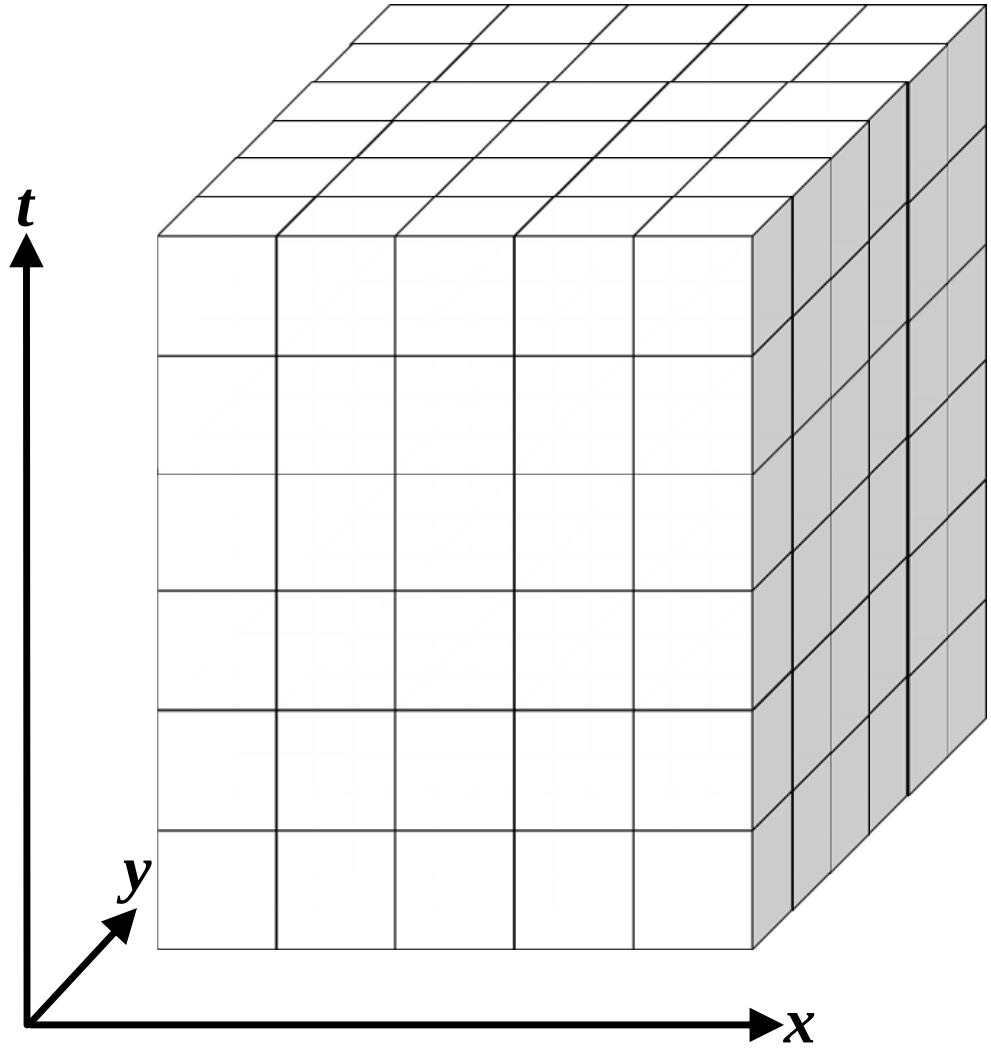


Figure 8. Stacked time series data extended into voxels (volumetric cells). The *x*-axis is the longitude, the *y*-axis is the latitude, and the *t*-axis is the time.

## 2.5 Morphological segmentation

Once the 3D binary voxel cubes were constructed for each disturbance site, the next step was to apply the `morph3d()` function of the *morphpy* library to segment each cube into distinct morphological classes. This process relies on a voxel-based morphological framework that characterizes the shape, structure, and connectivity of disturbed sites in both space and time. The segmentation algorithm is adapted from the original `morph` package developed for the R environment (Remmel, 2022) and fully re-implemented in Python as part of this study's *Phase-1* workflow.

Morphological segmentation was performed in a Jupyter Notebook environment to enable iterative development, real-time visualization, and reproducibility. For each voxel cube, the core function `morph3d()` (see Appendix B and Appendix D)[2] was executed with the logging option enabled. These included the parameters `VERBOSE=True`, which provided step-by-step console feedback during processing; `PLOT=True`, which triggered the display of key intermediate segmentation results; and `FINALPLOT=True`, which produced visual summaries of the classified morphological classes in 3D.

Upon execution, *morphpy* performed a series of connectivity-based operations to isolate and categorize clusters of disturbed voxels. These clusters were identified based on their 3D spatio-temporal configuration and evaluated through neighbourhood connectivity using morphological criteria defined in the original framework. The function output consisted of a labelled 3D array in which each voxel was assigned a morphological class code. The full sequence of operations implemented in *morphpy* is summarized in the code statement below.

[22] https://github.com/tejumade-ojo/morphpy.git

**Statement code: 3D Morphological Segmentation (*morphpy*)**

**Input:**

Binary 3D data cube (0 = undisturbed, 1 = disturbed)

**Output:**

Morphological classification map with codes:
MASS, SKIN, CRUMB, CIRCUIT, ANTENNA, BOND, VOID-VOLUME, VOID

**Step 1: Validate Input Data**

1. Check that the input is a numeric 3D array.
2. Confirm that values are binary (0 or 1).
3. Stop execution if validation fails.

**Step 2: Prepare Data Cube**

4. Pad the data cube with a one-voxel boundary to handle edge effects.
5. Assign a unique ID to each voxel.
6. Initialize:
   - objectID
   - coreCode
   - expandedCoreCode
   - morphCode.

**Step 3: Compute Voxel Connectivity**

7. Identify 6-connected neighbours (±x, ±y, ±t directions).
8. Retain only neighbours belonging to disturbed voxels (value = 1).
9. Build a graph representation of voxel connectivity.
10. Decompose the graph into connected components (objects).

**Step 4: Assign Object IDs**

11. Label each connected component with a unique object ID.
12. Assign all non-disturbed voxels as OUTSIDE (Code = 1)

**Step 5: Identify MASS Voxels**

13. For each object: Find voxels with 6 neighbours
14. Assign these as MASS (Code = 2)

**Step 6: Identify SKIN Voxels**

15. For each MASS voxel:
16. Identify neighbouring voxels not classified as MASS
17. Assign them as **SKIN (Code = 3)**

**Step 7: Identify CRUMB Voxels**

18. For each object:
19. If the object has only one voxel → assign CRUMB
20. If the object is not connected to MASS or SKIN → assign CRUMB. Label as **CRUMB (Code = 4)**

**Step 8: Identify CONNECTOR Voxels**

21. Assign all remaining disturbed voxels as **CONNECTOR**
22. If it connects only one core back to itself, assign **CIRCUIT** (**Code = 5**)

**Step 9: Identify ANTENNA Voxels**

23. For each object: Remove MASS and SKIN from the graph
24. Analyze remaining connector subgraphs
25. If a connector connects to MASS at only one point and forms a dead-end is classified as **ANTENNA (Code = 6)**

**Step 10: Identify BOND Voxels**

26. Identify separate MASS cores within each object.
27. Expand each core to include adjacent SKIN and CONNECTOR voxels
28. For each connector chain: If it connects two or more cores → assign **BOND (Code = 7)**

**Step 11: Identify VOID-VOLUME**

29. Perform flood-fill from the outer boundary.
30. Mark all external empty space as outside (-1)
31. Identify enclosed empty regions (not connected to the outside)
32. Validate that regions are fully surrounded by disturbed voxels
33. Assign valid regions as **VOID-VOLUME (Code = 8)**

**Step 12: Identify VOID Voxels**

34. For each VOID-VOLUME voxel: Check neighbouring disturbed voxels
35. Assign adjacent disturbed voxels as **VOID (Code = 9)**

**Step 13: Output Results**

36. Return final morphCode array and summary table
37. Optionally generate plots for each morphological class

The classification output for each site was used to generate both summary statistics and diagnostic visuals. An example of the 3D visualizations of each morphological class Figure 9 were automatically rendered within the Jupyter environment, allowing immediate assessment of segmentation accuracy. These included wireframe overlays of voxel clusters and colour-coded representations of all morphological classes shown in Figure 10. The visual feedback supported the interpretation of the disturbance through time Figure 11 and enabled verification of spatial coherence, temporal continuity, and classification. For each disturbance site, *morphpy* generated a summary table containing voxel counts per morphological class. These outputs formed the basis for subsequent statistical analysis, allowing comparison of morphological composition across disturbance types and ecoregions.

Following the completion of morphological segmentation, each voxel within the three-dimensional binary cube was classified into one of eight morphological classes. The output for each disturbance site was stored as a labelled NumPy array, where integer codes corresponded to the morphological categories: MASS, SKIN, CRUMB, CIRCUIT, ANTENNA, BOND, VOID-VOLUME, and VOID. These classified arrays formed the basis for the quantitative analysis of post-disturbance forest structure.

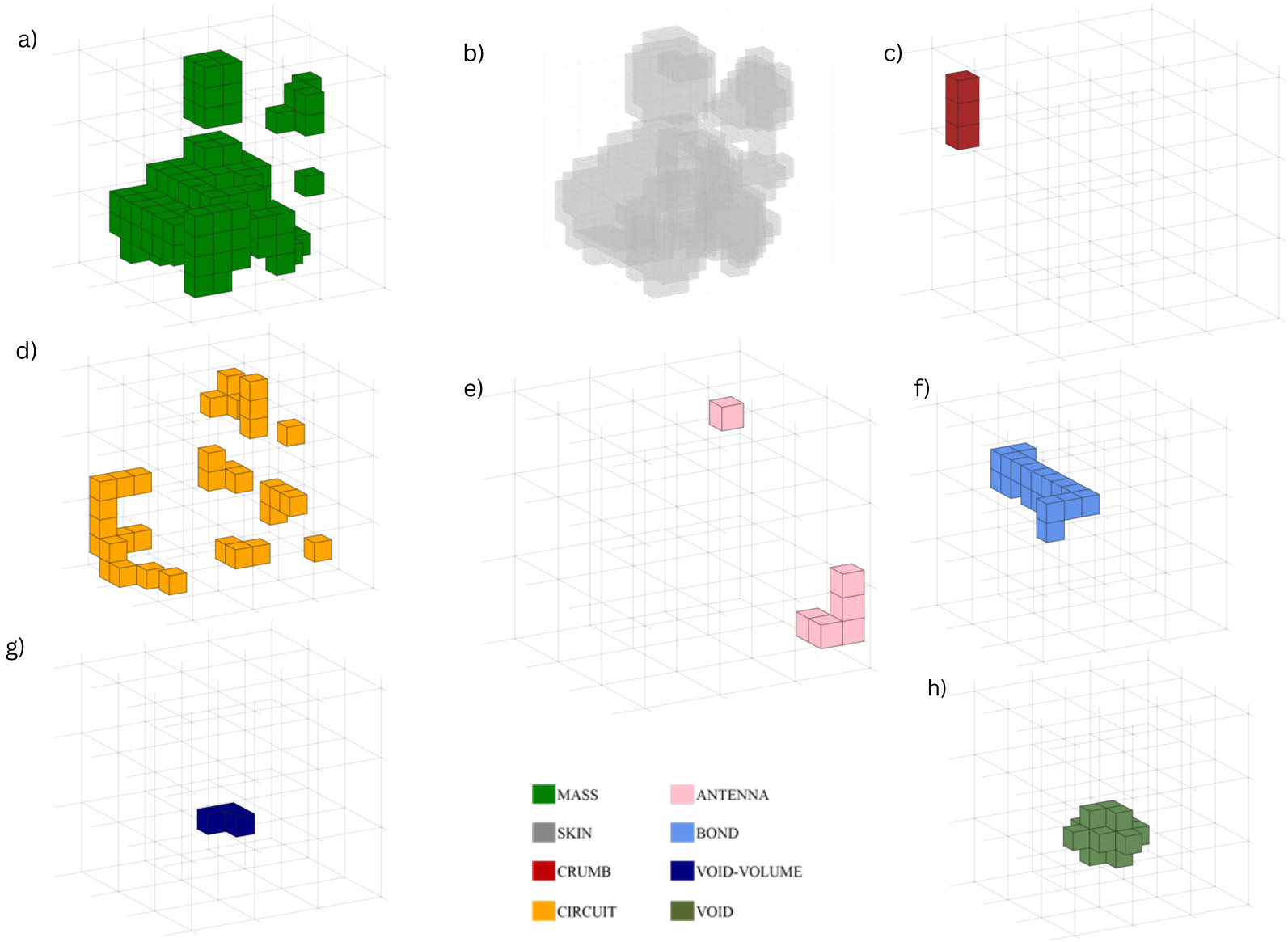


Figure 9. An example of 3D morphological classes showing a) MASS, b) SKIN, c) CRUMB, d) CIRCUIT, e) ANTENNA, f) BOND, g) VOID-VOLUME, h) VOID

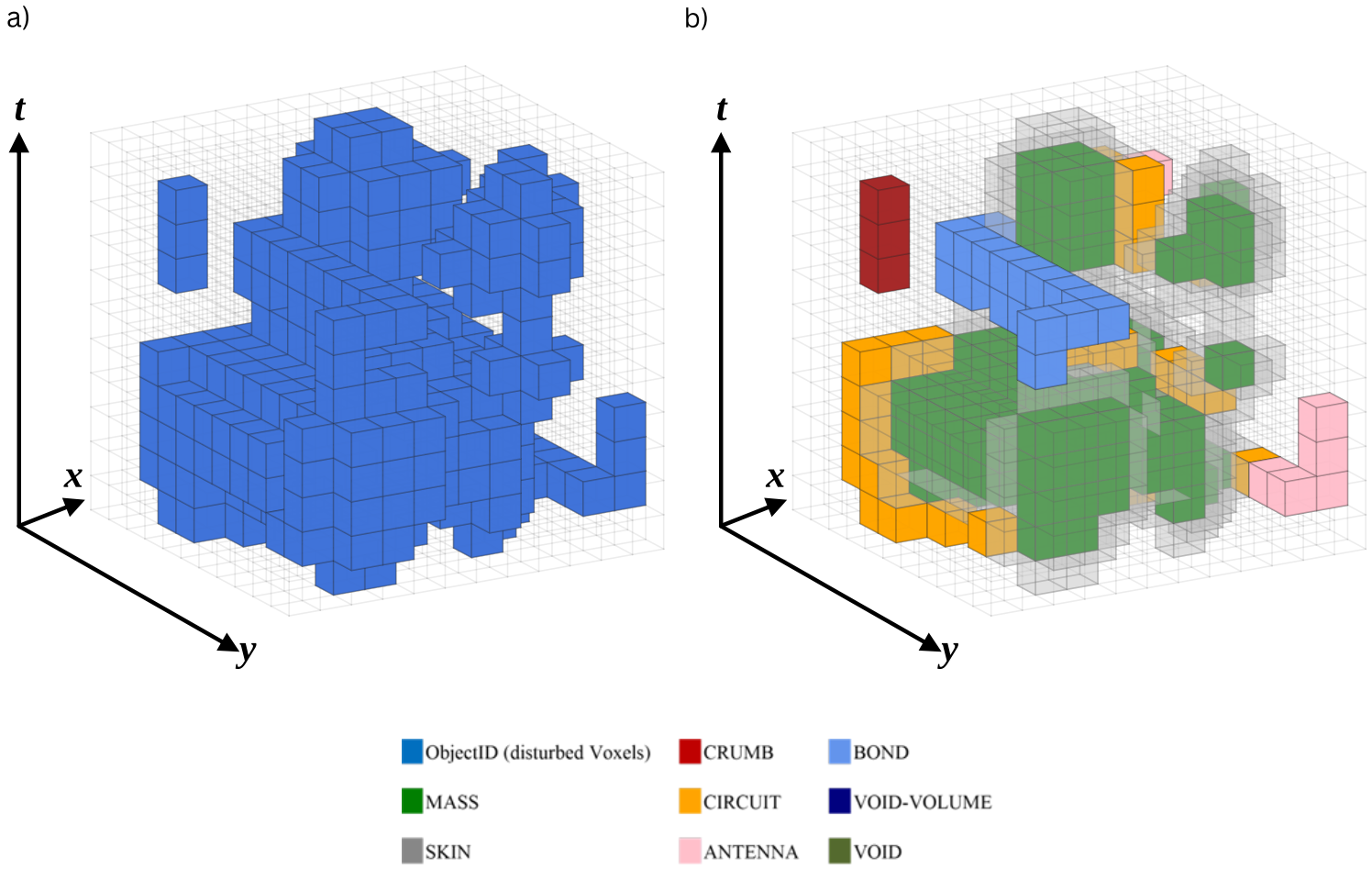


Figure 10. Three-dimensional representation of morphological classes, where (a) shows the objectID view of all disturbed voxels as a single connected structure and (b) presents the corresponding 3D morphological segmentation illustrating the spatial–temporal distribution of structural classes, with axes representing spatial dimensions (*x, y*) and time (*t*)

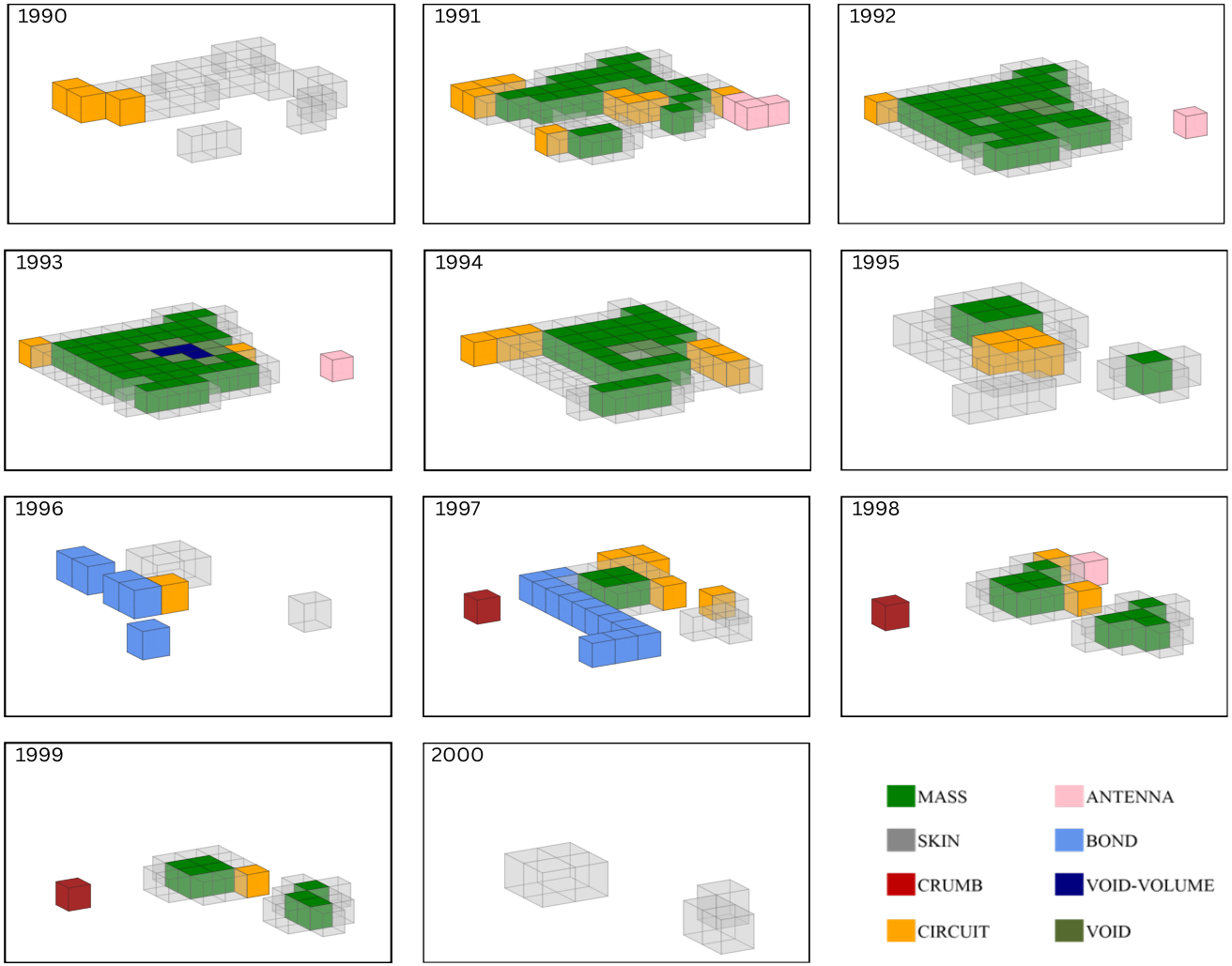


Figure 11. Temporal representation of 3D morphological structure (1990–2000). Morphological segmentation was performed on the full 3D (*x, y, t*) voxel cube, and each panel shows a 1-year slice extracted from the resulting 3D classification. The annual slices are displayed separately to reveal the internal spatial arrangement of morphological classes, including MASS, SKIN, CRUMB, CIRCUIT, ANTENNA, BOND, VOID-VOLUME and VOID

### 2.6 3D Morphological classes extraction

Voxel counts for each morphological class were computed using the NumPy (Harris et al., 2020) function `np.unique(..., return_counts=True)`. This operation produced the total number of voxels assigned to each class within a site. The results were subsequently organized into structured dictionaries and compiled using the pandas library (McKinney, 2010), enabling efficient tabulation and data export. To ensure comparability across sites of varying spatial extent, all voxel counts were normalized to percentages and proportions relative to the total number of disturbed voxels in each site. This normalization allowed structural composition to be interpreted independently of total disturbance size.

All site-level summaries were consolidated into a single master table with 30 rows (one per disturbance site) and 8 columns corresponding to the morphological classes, along with 2 additional categorical factor fields identifying disturbance type (wildfire or harvest) and ecoregion (East or West). The resulting dataset provided a standardized foundation for subsequent statistical analyses to test differences in morphological composition across disturbance categories.

### 2.7 Statistical analysis

The statistical design for this study was developed to evaluate how boreal forests regenerate after disturbance by quantifying differences in their three-dimensional morphological structure. Morphological segmentation produces eight interdependent classes: MASS, SKIN, CRUMB, CIRCUIT, ANTENNA, BOND, VOID, and VOID-VOLUME that together describe the integrity, connectivity, and fragmentation characteristics of the regenerating canopy. Because these classes emerge from the same voxel volume and respond jointly to ecological recovery processes, the analytical framework required methods capable of examining both the individual behaviour of each class and the collective behaviour of the entire structural system. All analyses were structured to address the three research questions guiding the thesis: whether wildfire and harvesting generate different morphological signatures, whether structural patterns are internally consistent within disturbance types, and how incorporating time as a third dimension enhances interpretation of post-disturbance recovery.

A range of statistical approaches was applied rather than relying on a single test per hypothesis. This was necessary because morphological classes are interdependent, multivariate,

and ecologically meaningful only when interpreted across multiple dimensions. The analysis followed a stepwise structure. First, exploratory visualizations were used to inspect distributions, examine extreme values, and understand general structural behaviour. Next, univariate tests were used to assess whether individual morphological classes differed between disturbance types. Finally, multivariate procedures evaluated the combined behaviour of the full morphological system. This stepwise approach allowed each research question to be examined from multiple analytical angles, increasing confidence in the interpretation of statistical outcomes.

Morphological segmentation was applied to voxel-based volumes derived from Landsat NDVI composites covering 1990–2000. Each voxel represented a binary vegetation state for a given year, and the third dimension encoded temporal depth across eleven years of post-disturbance recovery. From these volumes, voxel counts and site-level proportions were extracted for each morphological class. Proportions of morphological classes were used rather than raw voxel counts for each class, thereby standardizing comparisons across sites of different sizes (i.e., different total voxel counts) and ensuring that the structural analyses reflected relative composition rather than absolute volume.

### 2.8 Disturbance type and ecoregion differences.

This analysis evaluates whether regeneration structure differs between wildfire and harvesting disturbances and between eastern and western boreal ecoregions (which differ in terms of fire regime (McRae et al., 2001; Best et al., 2024). The Ontario Managed Forest spans a large geographic area that includes environmental gradients in climate, precipitation, soil conditions, and disturbance history. These gradients can influence forest regeneration patterns and vegetation recovery trajectories following disturbance (MNR, 2013; Ontario Ministry of Northern Development, Mines, Natural Resources and Forestry, 2021). To account for these regional differences, sites were coded as belonging to either the eastern or western ecoregion within the Ontario Managed Forest. This stratification allows the analysis to determine whether observed regeneration structures are driven solely by disturbance type (wildfire versus harvesting) or whether regional ecological context also contributes to differences in morphological class composition.

**$H_0$:** Morphological class proportions are the same for wildfire and harvesting sites within the Ontario MF.

**$H_1$:** Morphological class proportions are not the same for wildfire and harvesting sites.

**$H_0$**: The distribution of morphological class proportions is the same for western and eastern ecoregions.

**$H_1$**: The distribution of morphological class proportions is not the same for western and eastern ecoregions.

Morphological differences between disturbance types and ecoregions were examined using a structured, multilevel analytical framework that progressed from aggregated comparisons to class-specific and multivariate analyses. This approach enabled the identification of broad differences in overall morphological composition, the specific classes contributing to those differences, and the combined behaviour of structural elements across disturbance and regional contexts.

Overall morphological composition was assessed using contingency table analysis to compare the distribution of morphological classes between groups. Observed voxel counts were aggregated by class and grouped by disturbance type and ecoregion. Chi-square tests of homogeneity were applied to compare observed and expected frequencies under the assumption of no difference in morphological composition. Separate tests were conducted for disturbance type (wildfire versus harvesting) and ecoregion (west versus east), and for stratified comparisons within each disturbance category. All tests were evaluated at a significance level of $\alpha = 0.05$.

**$H_0$**: The mean proportion of each morphological class does not differ between wildfire and harvesting sites.

**$H_1$**: The mean proportion of at least one morphological class differs between wildfire and harvesting sites.

**$H_0$:** The mean proportion of each morphological class does not differ between western and eastern ecoregions.

**$H_1$:** The mean proportion of at least one morphological class differs between western and eastern ecoregions.

Class-level differences in morphological composition were examined using independent-samples *t*-tests applied to site-level proportions. Mean proportions of each morphological class were compared between wildfire and harvesting sites and between western and eastern ecoregions. This approach enabled the identification of specific structural elements that differed between groups, even when aggregated distributions appeared similar.

**$H_0$:** Among wildfire sites, the distribution of morphological class proportions is the same between western and eastern ecoregions.

**$H_1$:** Among wildfire sites, the distribution of morphological class proportions is not the same between western and eastern ecoregions.

To determine whether regional differences in morphological composition were present within each disturbance type, separate stratified analyses were conducted for wildfire and harvested sites. This approach allowed the influence of ecoregion to be evaluated while holding disturbance origin constant. For wildfire sites, morphological class proportions were grouped by western and eastern ecoregions and compared using a Chi-square test of homogeneity of proportions. The test evaluated whether the proportional distribution of morphological classes was the same across regions for fire-disturbed sites.

The same procedure was then applied to harvested sites. Morphological class proportions for harvest-disturbed sites were grouped by western and eastern ecoregions, and a separate Chi-square test of homogeneity of proportion was used to assess whether regional differences in class composition existed within harvested disturbances.

**$H_0$:** Among harvested sites, the distribution of morphological class proportions is the same between western and eastern ecoregions.

**$H_1$:** Among harvested sites, the distribution of morphological class proportions is not the same between western and eastern ecoregions.

For both analyses, observed class totals were compared with expected frequencies under the null hypothesis of equal proportional distributions. Tests were evaluated at a significance level of $\alpha = 0.05$. By conducting these stratified comparisons separately for wildfire and harvesting, the analysis determined whether regional effects were consistent across disturbance types or specific to a single disturbance process.

Distributional divergence between groups was quantified using symmetric Kullback–Leibler divergence (KLD) (Kullback & Leibler, 1951) based on group-level mean compositions. These metrics measure divergence between probability distributions and were used to compare wildfire and harvesting compositions, as well as western and eastern ecoregional compositions, providing a continuous measure of structural dissimilarity beyond hypothesis testing.

**$H_0$:** The multivariate mean morphological composition does not differ between wildfire and harvesting sites

**$H_1$**: The multivariate mean morphological composition differs between wildfire and harvesting sites.

**$H_0$**: The multivariate mean morphological composition does not differ between western and eastern ecoregions.

**$H_1$:** The multivariate mean morphological composition differs between western and eastern ecoregions.

Multivariate differences in morphological composition were assessed using a multivariate analysis of variance (MANOVA) applied to all morphological classes simultaneously. This approach evaluates whether the combined morphological composition differs between disturbance types and between ecoregions while accounting for covariance among classes. The

analysis was conducted using the `MANOVA()` function, with Wilks' lambda used as the primary test statistic. All analyses were conducted using normalized morphological class proportions to ensure comparability across sites and to reflect relative structural composition rather than differences in total voxel counts.

### 2.9 Morphological structure within disturbance types

This analysis evaluates whether regeneration structures remain internally consistent within disturbance types and across ecological regions.

Morphological structures within disturbance types were examined to determine whether they are internally coherent within each disturbance type, whether wildfire sites resemble one another in their structural patterns, and whether harvesting sites exhibit similar internal consistency. This question focuses on within-group stability rather than between-group differences.

**$H_0$:** Morphological class composition does not differ within disturbance types.
**$H_1$:** Morphological class composition differs between ecoregions and/or within disturbance types.

**$H_0$**: Morphological class composition does not differ between the East and West ecoregions.
**$H_1$**: Morphological class composition differs between ecoregions.

Variation in morphological composition within disturbance categories was assessed using multivariate dispersion analysis to evaluate the degree of structural consistency across sites. This analysis complements between-group comparisons by quantifying how tightly site-level morphological compositions cluster within each disturbance type.

Bray–Curtis dissimilarity was calculated from site-level morphological class proportions to quantify compositional differences between sites. Bray–Curtis is a distance measure that compares the relative composition of two samples based on class abundances or proportions, where values range from 0 (identical composition) to 1 (completely dissimilar composition) (Bray & Curtis, 1957; Legendre et al., 1998). This measure is appropriate for proportional ecological data and was used to construct a dissimilarity matrix representing variation in

morphological composition across all sites. Distances from each site to its group centroid were then calculated from the Bray–Curtis dissimilarity matrix. These distances provide a measure of within-group variability, with smaller distances indicating greater structural consistency and larger distances indicating higher heterogeneity among sites within the same disturbance category. Differences in dispersion between groups were formally tested using permutational analysis of multivariate dispersions (PERMDISP). This analysis was used to compare structural variability between disturbance types and between ecoregions by testing whether mean distances to group centroids differ significantly between groups.

**$H_0$**: Morphological classes do not differ among Fire–West, Fire–East, Harvest–West, and Harvest–East groups.

**$H_1$**: Morphological classes differ among the Fire–West, Fire–East, Harvest–West, and Harvest–East groups.

To examine the combined influence of disturbance and ecoregion on structural variability, dispersion was also evaluated across four disturbance–ecoregion subgroups (Fire–West, Fire–East, Harvest–West, and Harvest–East). This allowed assessment of whether structural consistency differs when disturbance type and regional context are considered jointly.

To support the interpretation of multivariate patterns, principal coordinates analysis (PCoA) was conducted using the Bray–Curtis dissimilarity matrix (Bray & Curtis, 1957; Gower, 1966). This ordination method provides a low-dimensional representation of relationships among sites, allowing visualization of clustering patterns and relative dispersion among disturbance types and ecoregions.

In addition, a two-factor multivariate analysis of variance (MANOVA) including disturbance type, ecoregion, and their interaction was conducted to assess whether differences in morphological composition vary across regions. This analysis complements dispersion-based methods by evaluating whether group-level differences depend on the interaction between disturbance and regional context.

## 2.10 Time-explicit 3D voxel segmentation

The third research question examined how the temporal dimension, incorporated directly into the voxel-based model, enhances the interpretation of post-disturbance regeneration structure. Time-explicit analysis was used to examine how morphological structures developed, persisted, and changed across consecutive years following disturbance. Rather than treating each annual disturbance layer as an independent map, annual binary classifications were stacked into a single voxel cube in which the third analytical dimension represented time. This allowed regeneration to be evaluated as a connected structural process unfolding across years rather than as a sequence of isolated spatial snapshots.

For each disturbance site, an annual binary raster representing disturbed and undisturbed conditions was arranged sequentially to form an 11-layer (*x, y, t)* voxel cube spanning 1990 to 2000. Morphological segmentation was then applied to the full time-explicit cube using *morphpy*, assigning each voxel to one of the eight 3D morphological classes. This procedure preserved temporal adjacency between consecutive years and enabled the detection of structural transitions, such as consolidation, fragmentation, reconnection, and enclosure, over time.

Temporal outputs were summarized at multiple levels to support comparison of regeneration trajectories. First, annual voxel counts and annual proportions of each morphological class were calculated for every site, producing year-by-year summaries of structural composition. These annual summaries were then averaged across all wildfire and harvested sites to generate disturbance-level temporal trajectories. Equivalent summaries were also calculated separately for western and eastern sites within each disturbance type to evaluate regional differences in time-explicit regeneration patterns. In addition, annual class trajectories were retained for each individual site to examine variability in temporal behaviour among disturbance events.

Temporal trajectories were summarized using both voxel counts and relative proportions for each morphological class because the two measures provided complementary information. Voxel counts described changes in the absolute amount of each class through time, revealing increases or decreases in total structural extent. Relative proportions described how each class's contribution changed relative to the total disturbed structure, allowing comparison after standardizing for differences in site size. Using both measures provided a more complete

interpretation of morphological change through time, as absolute abundance and relative dominance may emphasize different temporal patterns.

Temporal trajectories were visualized using stacked area charts in which annual counts and proportions of morphological classes were plotted through time. These visualizations were generated for all wildfire and harvested sites combined, for wildfire and harvested sites stratified by ecoregion, and for each individual disturbance site. This time-explicit representation was used to identify recurring patterns in the emergence, persistence, fluctuation, and decline of morphological classes across years, thereby extending the analysis beyond single-year comparisons to the structural progression of regeneration through time.

# 3 Results

## 3.1 Segmentation output overview

This section presents the results of segmentation and statistical analyses examining post-disturbance boreal regeneration patterns across wildfire and harvesting sites. The findings are organized according to the three research questions: (1) the characteristics of the segmentation output, (2) statistical comparisons that evaluate differences and similarities among disturbance types, ecoregions, and internal structural consistency, and (3) the influence of the temporal dimension on the resulting morphological patterns.

Morphological segmentation was successfully performed for all 30 disturbance sites included in the study. Across all sites, every morphological class was segmented and represented in all the disturbance sites, although the relative abundance of individual classes varied substantially among sites.

Initial evaluation of the segmentation output indicated clear differences in mean morphological composition between disturbance types, shown in Figure 12. MASS and SKIN accounted for the largest proportion of disturbed voxels at both wildfire and harvesting sites, confirming that these classes were the dominant structural elements overall. Wildfire sites showed a greater relative proportion of MASS, suggesting larger, less fragmented disturbance patterns over time, whereas harvesting sites showed higher proportions of BOND, CIRCUIT, and CRUMB, indicating more subdivided, connected temporal structural patterns. VOID and VOID-VOLUME remained minor classes in both groups but were slightly more represented in wildfire and harvested sites, consistent with the presence of internal gaps within the space–time structure.

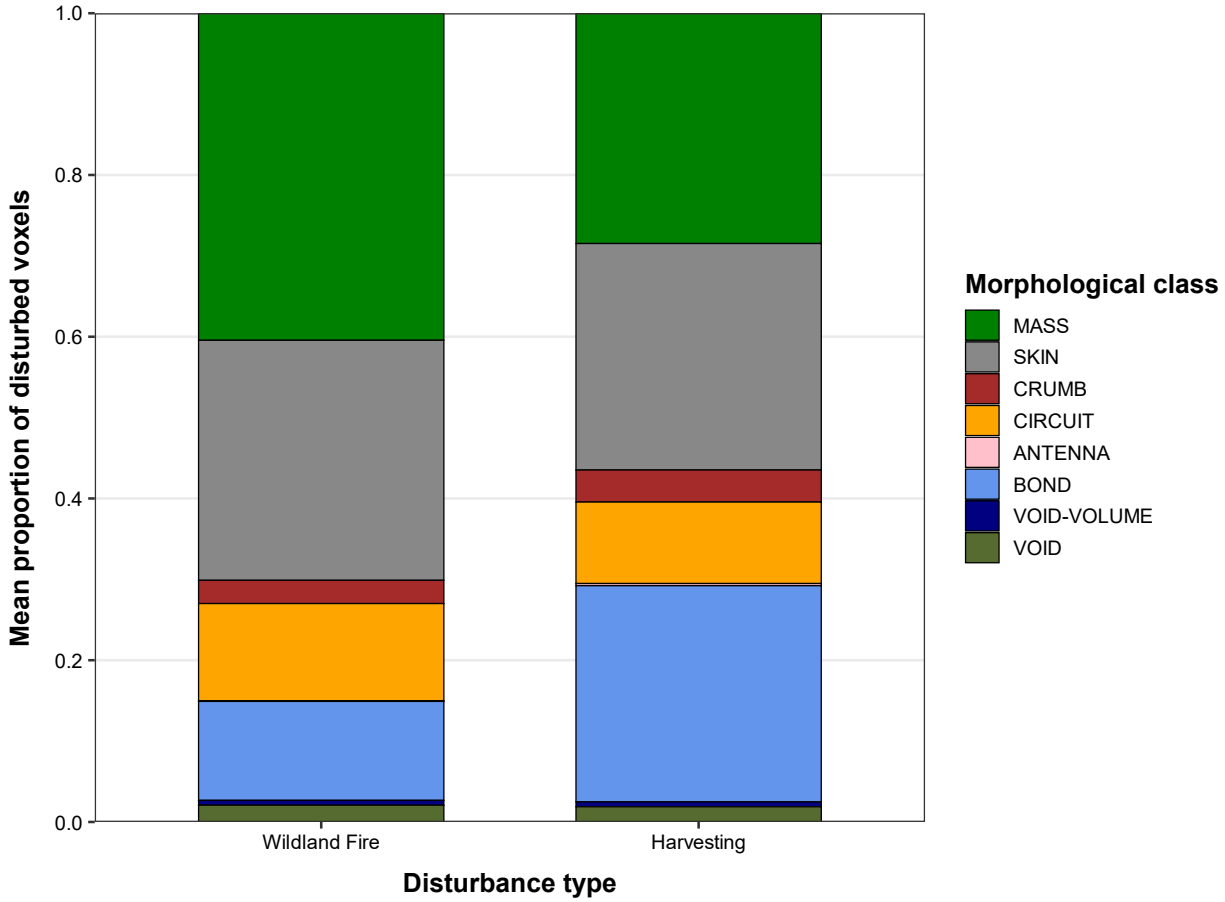


Figure 12. Mean proportional composition of 3D morphological classes by disturbance type. Stacked bars show the average share of disturbed voxels classified as MASS, SKIN, CRUMB, CIRCUIT, ANTENNA, BOND, VOID-VOLUME, and VOID across all wildfires and harvesting sites.

Regional contrasts were also evident in the average morphological composition of disturbed voxels across the western and eastern boreal ecoregions, as shown in Figure 13. In both regions, MASS and SKIN represented the highest proportions among the classified voxels, indicating that core and edge structures remained the dominant components of regeneration patterns. The western ecoregion had a higher proportion of MASS, consistent with larger, less fragmented disturbance patterns over time. By comparison, the eastern ecoregion exhibited greater proportions of BOND, CIRCUIT, and CRUMB, reflecting more subdivided and connected structural patterns across years. VOID and VOID-VOLUME contributed only a small share of the total composition in both regions, with modest differences between ecoregions.

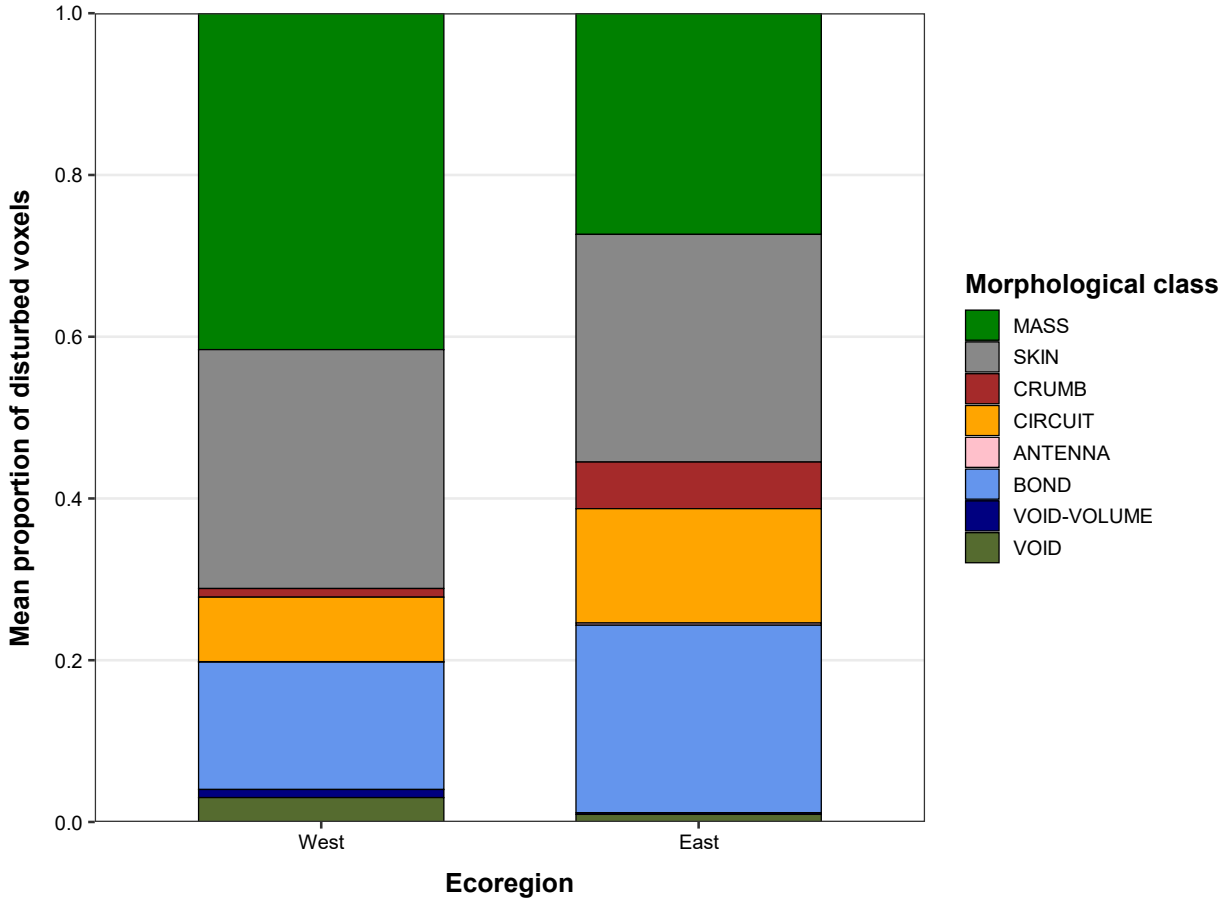


Figure 13. Mean proportional composition of 3D morphological classes by boreal ecoregion. Stacked bars show the average share of disturbed voxels classified as MASS, SKIN, CRUMB, CIRCUIT, ANTENNA, BOND, VOID-VOLUME, and VOID across all sites in the western and eastern boreal regions.

### 3.2 Disturbance regeneration structure and ecoregion differences

Descriptive summaries revealed broad structural contrasts between wildfire and harvesting disturbance sites (Table 3). Across wildfire-affected sites, MASS and SKIN consistently accounted for the largest proportions of disturbed voxels, indicating development of more cohesive interior and surface structures. In contrast, harvested sites exhibited relatively higher contributions from transitional and connective classes, particularly BOND, and an increased representation of fragmented components such as CRUMB and CIRCUIT, suggesting a more segmented regeneration structure. These results suggest that harvesting regeneration remained more segmented and connection-dependent than wildfire regeneration, based on the combined behaviour of multiple morphological classes.

Table 3. Descriptive statistics for the proportion of morphological classes for wildfire and harvesting disturbance sites across eastern and western ecoregions, derived from 11-year NDVI-based voxel segmentation (1990–2000).

| Distype | DisturbID | MASS | SKIN | CRUMB | CIRCUIT | ANTENNA | BOND | VVOL | VOID |
|---|---|---|---|---|---|---|---|---|---|
| Fire | 1 | 0.46 | 0.29 | 0.01 | 0.08 | 0.00 | 0.10 | 0.01 | 0.04 |
| Fire | 2 | 0.55 | 0.26 | 0.00 | 0.07 | 0.00 | 0.05 | 0.02 | 0.06 |
| Fire | 3 | 0.45 | 0.30 | 0.00 | 0.09 | 0.00 | 0.11 | 0.01 | 0.04 |
| Fire | 4 | 0.59 | 0.27 | 0.00 | 0.05 | 0.00 | 0.03 | 0.01 | 0.04 |
| Fire | 5 | 0.48 | 0.33 | 0.01 | 0.10 | 0.00 | 0.05 | 0.01 | 0.02 |
| Fire | 6 | 0.58 | 0.29 | 0.00 | 0.05 | 0.00 | 0.03 | 0.01 | 0.03 |
| Fire | 7 | 0.44 | 0.33 | 0.00 | 0.08 | 0.00 | 0.12 | 0.01 | 0.02 |
| Fire | 8 | 0.38 | 0.35 | 0.05 | 0.10 | 0.00 | 0.11 | 0.00 | 0.00 |
| Fire | 9 | 0.07 | 0.10 | 0.11 | 0.49 | 0.00 | 0.23 | 0.00 | 0.00 |
| Fire | 10 | 0.40 | 0.34 | 0.03 | 0.11 | 0.00 | 0.11 | 0.00 | 0.01 |
| Fire | 11 | 0.17 | 0.31 | 0.03 | 0.10 | 0.00 | 0.39 | 0.00 | 0.00 |
| Fire | 12 | 0.40 | 0.35 | 0.02 | 0.12 | 0.00 | 0.09 | 0.01 | 0.02 |
| Fire | 13 | 0.38 | 0.30 | 0.04 | 0.11 | 0.00 | 0.15 | 0.00 | 0.01 |
| Fire | 14 | 0.26 | 0.29 | 0.10 | 0.16 | 0.01 | 0.16 | 0.00 | 0.01 |
| Fire | 15 | 0.44 | 0.33 | 0.03 | 0.09 | 0.00 | 0.10 | 0.00 | 0.01 |
| Harvest | 1 | 0.36 | 0.23 | 0.00 | 0.07 | 0.00 | 0.27 | 0.01 | 0.04 |
| Harvest | 2 | 0.14 | 0.23 | 0.05 | 0.11 | 0.00 | 0.46 | 0.00 | 0.00 |
| Harvest | 3 | 0.24 | 0.21 | 0.04 | 0.08 | 0.01 | 0.41 | 0.01 | 0.02 |
| Harvest | 4 | 0.34 | 0.29 | 0.01 | 0.08 | 0.00 | 0.23 | 0.01 | 0.03 |
| Harvest | 5 | 0.51 | 0.34 | 0.00 | 0.07 | 0.00 | 0.03 | 0.01 | 0.04 |
| Harvest | 6 | 0.49 | 0.33 | 0.00 | 0.08 | 0.00 | 0.06 | 0.01 | 0.03 |
| Harvest | 7 | 0.27 | 0.35 | 0.01 | 0.08 | 0.00 | 0.24 | 0.01 | 0.02 |
| Harvest | 8 | 0.31 | 0.36 | 0.03 | 0.10 | 0.00 | 0.16 | 0.01 | 0.02 |
| Harvest | 9 | 0.30 | 0.28 | 0.01 | 0.08 | 0.00 | 0.28 | 0.01 | 0.03 |
| Harvest | 10 | 0.19 | 0.19 | 0.05 | 0.08 | 0.01 | 0.47 | 0.01 | 0.01 |
| Harvest | 11 | 0.26 | 0.29 | 0.06 | 0.12 | 0.00 | 0.25 | 0.00 | 0.01 |
| Harvest | 12 | 0.25 | 0.25 | 0.15 | 0.16 | 0.01 | 0.16 | 0.00 | 0.01 |
| Harvest | 13 | 0.20 | 0.30 | 0.06 | 0.17 | 0.01 | 0.24 | 0.00 | 0.01 |
| Harvest | 14 | 0.25 | 0.30 | 0.04 | 0.12 | 0.00 | 0.26 | 0.00 | 0.01 |
| Harvest | 15 | 0.13 | 0.22 | 0.08 | 0.10 | 0.00 | 0.46 | 0.00 | 0.00 |

Site-level distributions of morphological class proportions by disturbance type are shown in Figure 14. MASS exhibits a higher median and broader spread under wildfire, while BOND shows higher median values and substantially greater variability under harvesting. SKIN and CIRCUIT display overlapping central tendencies but differ in dispersion, indicating partial structural similarity with differing variability between disturbance types. CRUMB remains low in both groups but shows greater variability under harvesting. ANTENNA contributes negligibly across all sites, while VOID and VOID-VOLUME show moderate representation with largely overlapping distributions.

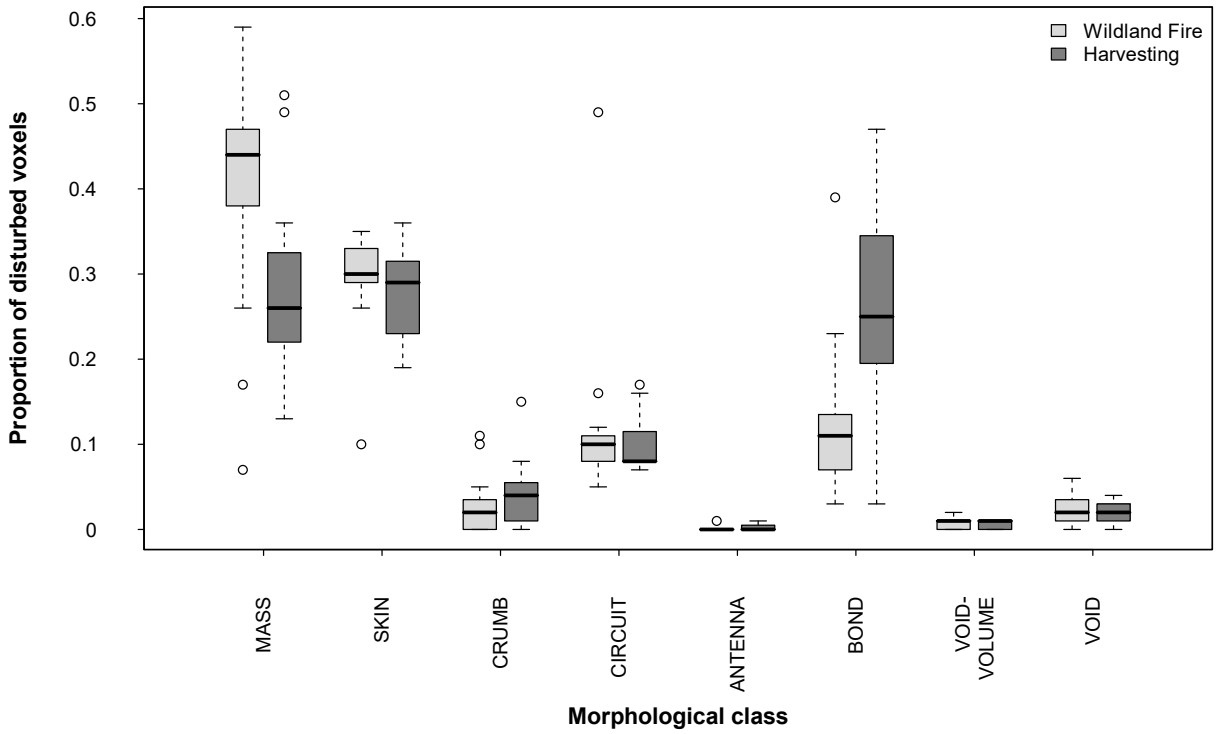


Figure 14. Distribution of morphological class proportions across disturbance types, wildfire and harvesting

Class-specific patterns are further illustrated in Figure 15, where each morphological class is presented separately. These panels confirm that differences between disturbance types are concentrated in a subset of classes. MASS consistently dominates wildfire sites, whereas BOND is more prominent and variable in harvested sites. Other classes, including SKIN, CIRCUIT, and VOID-related categories, exhibit substantial overlap between disturbance types, indicating that not all structural components respond strongly to disturbance differences.

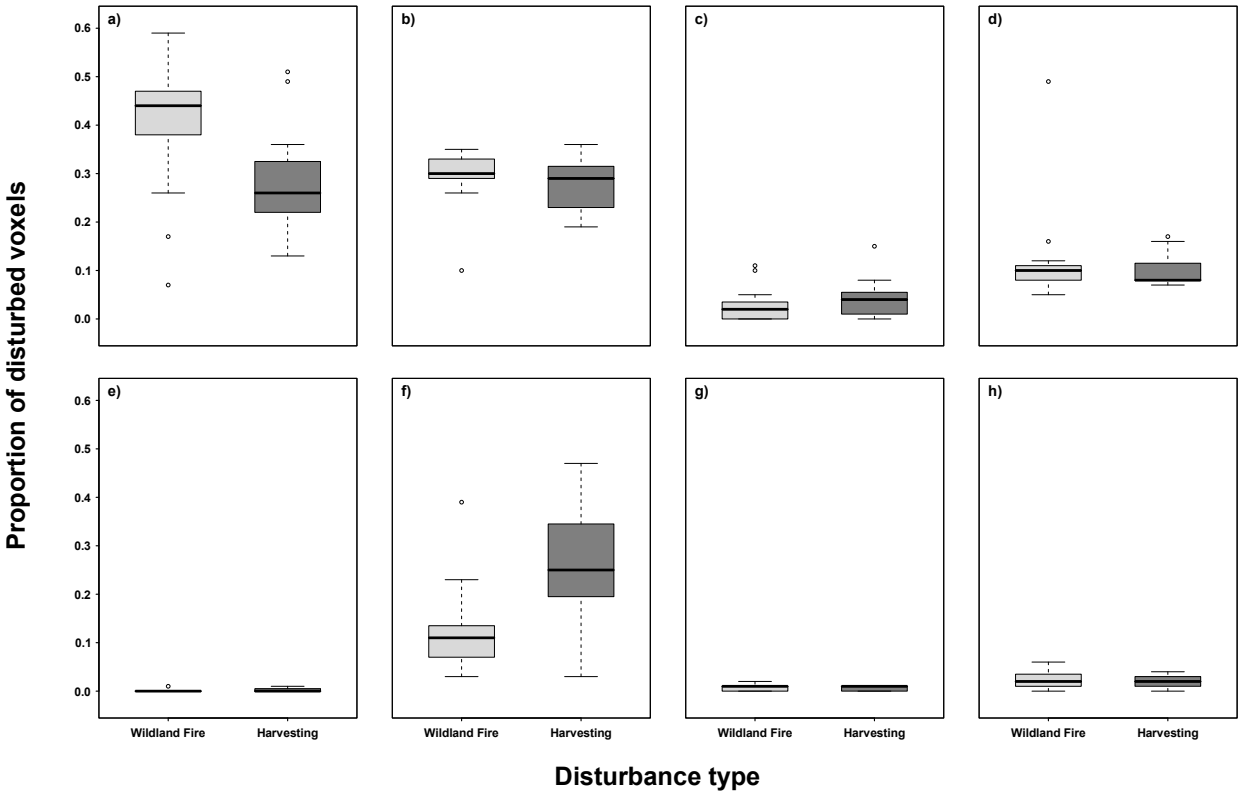


Figure 15. Disturbance regeneration structure differences between wildfire and harvest sites based on morphological class proportions: a) MASS, b) SKIN, c) CRUMB, d) CIRCUIT, e) ANTENNA, f) BOND, g) VOID-VOLUME, and h) VOID.

To evaluate whether wildfire and harvesting disturbances produce distinct morphological structures, both aggregated and class-level statistical analyses were conducted.

Table 4. Contingency table of observed (O) and expected (E) proportions for morphological classes by disturbance types.

| DistType | MASS | SKIN | CRUMB | CIRCUIT | ANTENNA | BOND | VVOL | VOID |
|---|---|---|---|---|---|---|---|---|
| Fire(O) | 6.05 | 4.44 | 0.43 | 1.79 | 0.03 | 1.84 | 0.11 | 0.32 |
| Fire(E) | 5.15 | 4.31 | 0.52 | 1.65 | 0.04 | 2.91 | 0.11 | 0.30 |
| Harvesting(O) | 4.26 | 4.19 | 0.61 | 1.52 | 0.06 | 3.97 | 0.10 | 0.29 |
| Harvesting(E) | 5.15 | 4.31 | 0.52 | 1.65 | 0.04 | 2.91 | 0.11 | 0.30 |

At the aggregated level, a chi-square test of homogeneity of proportion was applied to the summed morphological class proportions obtained by pooling the site-level proportions for all 15 wildfire sites and all 15 harvesting sites into two group totals Table 4. The test statistic ($\chi^2 = 1.17$, $df = 7$) was less than the critical value = 14.067, indicating no statistically significant difference in overall morphological composition between wildfire and harvesting sites. This result suggests that, when morphological classes are considered collectively, the overall proportional distribution remains broadly similar across disturbance types. The Chi-square distribution and decision threshold are illustrated in Figure 16.

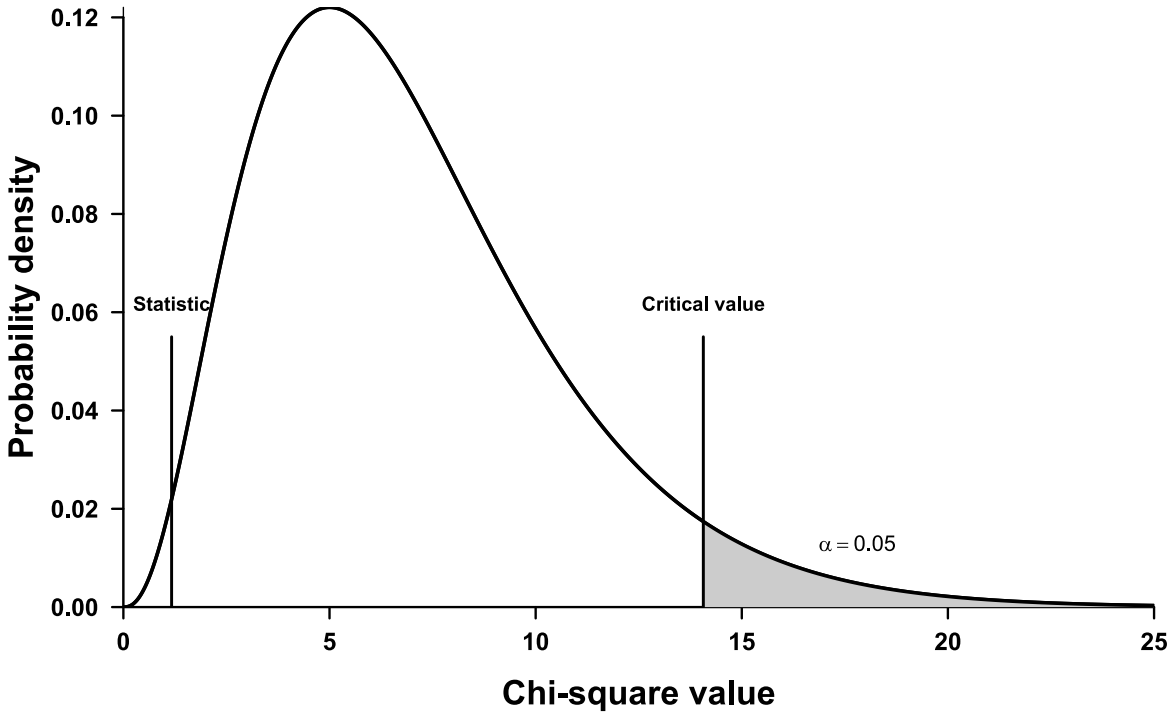


Figure 16. Chi-square distribution showing the test statistic and critical value for the morphological class frequency comparison based on disturbance type. The shaded grey area indicates the critical region.

Table 5. Independent-samples *t*-test results comparing mean morphological class proportions between wildfire and harvesting disturbance types.

| MorphClass | Mean_Wildfire | Mean_Harvesting | *t* | *df* | *p*-value |
|---|---|---|---|---|---|
| MASS | 0.4033 | 0.2707 | 2.5855 | 28 | 0.0152 |
| SKIN | 0.2960 | 0.2180 | 0.8563 | 28 | 0.3991 |
| CRUMB | 0.0287 | 0.0393 | -0.7781 | 28 | 0.4431 |
| CIRCUIT | 0.1200 | 0.1000 | 0.7013 | 28 | 0.4889 |
| ANTENNA | 0.0007 | 0.0027 | -1.4739 | 28 | 0.1517 |
| BOND | 0.1220 | 0.2653 | -3.3837 | 28 | 0.0021 |
| VOID_VOLUME | 0.0060 | 0.0060 | -0.0000 | 28 | 1.0000 |
| VOID | 0.0207 | 0.0187 | 0.3498 | 28 | 0.7291 |

At the class-specific level, independent-samples *t*-tests were conducted for each morphological class to compare mean proportions between wildfire and harvesting sites, with $\alpha = 0.05$. For each test, the null hypothesis ($H_0$) stated that the mean class proportion did not differ between disturbance types, while the alternative hypothesis ($H_1$) stated that the mean proportion differed between wildfire and harvesting sites. Results indicated statistically significant differences for MASS and BOND. Mean MASS proportions were significantly higher in wildfire sites ($p < 0.05$), whereas mean BOND proportions were significantly higher in harvested sites ($p < 0.05$). No statistically significant differences were detected for SKIN, CRUMB, CIRCUIT, ANTENNA, VOID-VOLUME, or VOID ($p > 0.05$).

Together, these results indicate that disturbance effects are not uniform across all morphological classes but are instead expressed through the combined behaviour of key structural components. Wildfire disturbance sites are generally shown to be associated with greater development of core structural elements MASS and lower BOND proportions, reflecting more cohesive and internally connected regenerated structures, while harvested sites show reduced MASS and increased BOND proportions, indicating more fragmented and connector-dependent regeneration structure . However, these class-level differences do not translate into a significant shift in the overall morphological composition when all classes are considered together

Morphological structure also varied by ecoregion. When sites were grouped into eastern and western boreal regions, western sites generally had higher proportions of MASS ($p < 0.05$),

indicating more consolidated core structures. In contrast, eastern sites had higher proportions of CRUMB, CIRCUIT and BOND ($p < 0.05$). Distributional differences across ecoregions are shown in Figure 17 and Figure 18, where boxplots summarize class-level proportions by region. MASS exhibits higher medians and greater spread at western sites, whereas CRUMB and CIRCUIT show higher central tendencies at eastern sites. SKIN and ANTENNA display substantial overlap between regions. indicating limited regional differentiation for these classes. Differences in VOID-related classes are present but less pronounced compared to core and connector classes.

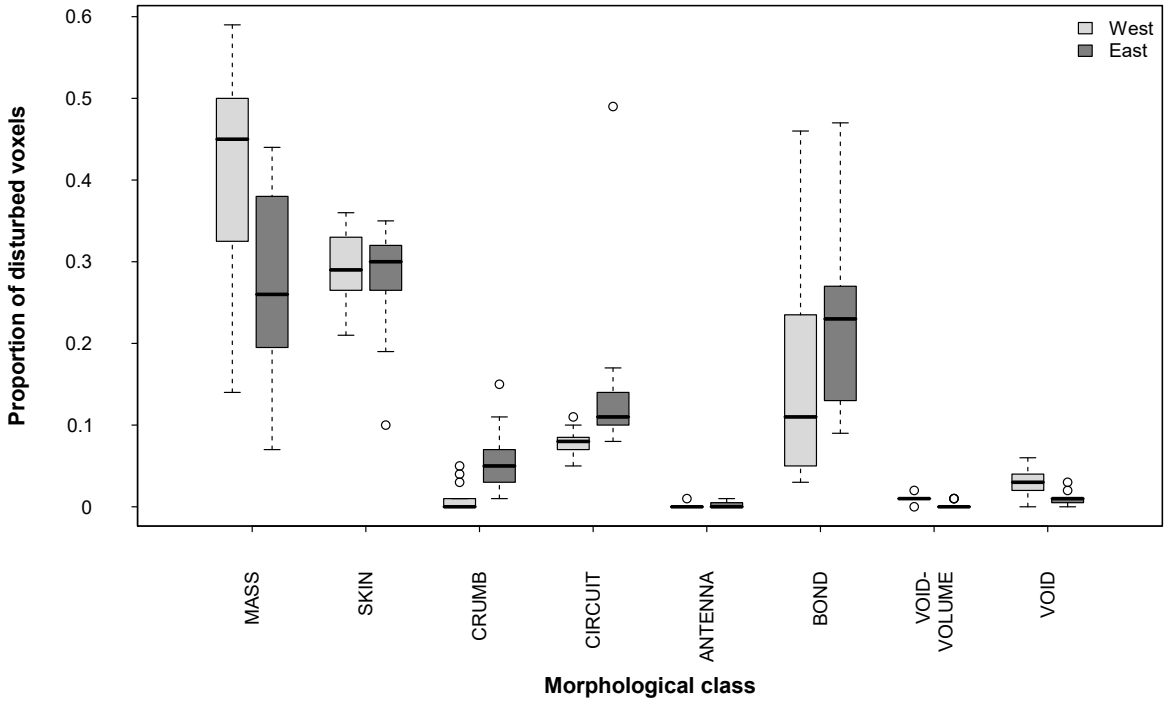


Figure 17. Distribution of morphological class proportions across the western and eastern boreal ecoregions based on combined wildfire and harvesting disturbance sites.

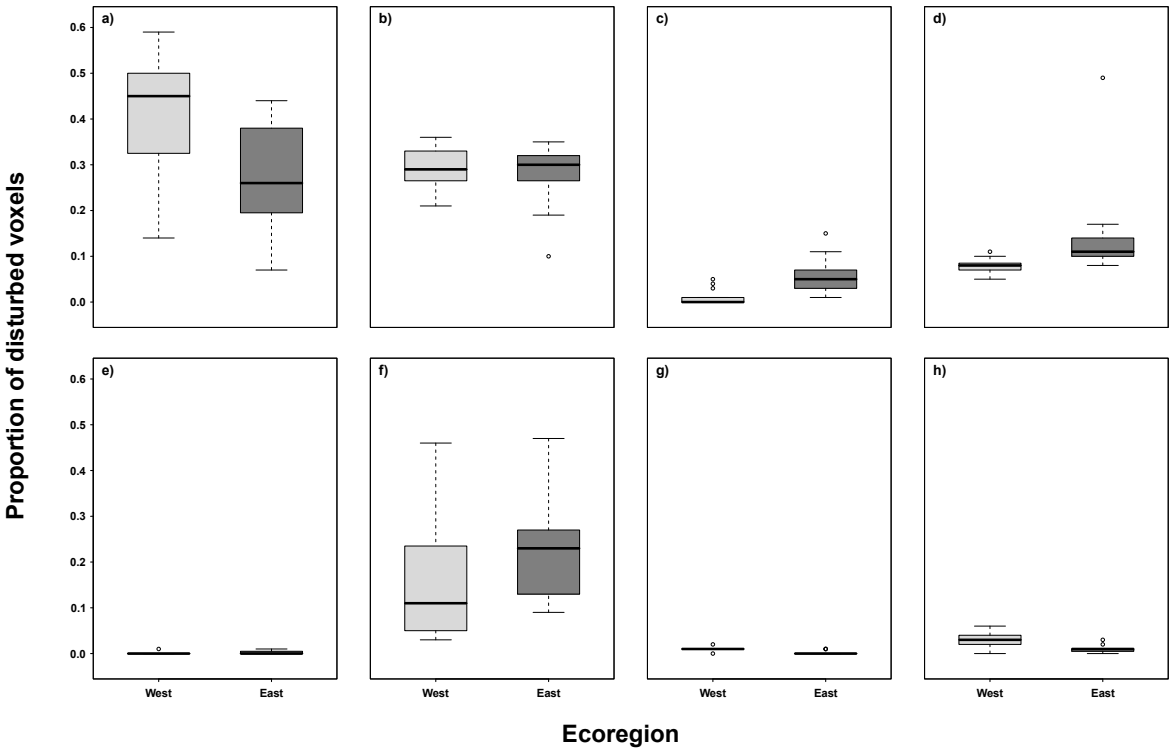


Figure 18. Distribution of morphological class proportions across western and eastern boreal ecoregions. Based on morphological class proportions: a) MASS, b) SKIN, c) CRUMB, d) CIRCUIT, e) ANTENNA, f) BOND, g) VOID-VOLUME, and h) VOID.

Table 6. Contingency table of observed (O) and expected (E) proportions for morphological classes by western and eastern ecoregions.

| DistType | MASS | SKIN | CRUMB | CIRCUIT | ANTENNA | BOND | VVOL | VOID |
|---|---|---|---|---|---|---|---|---|
| West(O) | 5.90 | 3.23 | 0.18 | 1.14 | 0.03 | 2.21 | 1.02 | 1.29 |
| West(E) | 4.93 | 3.33 | 0.51 | 1.60 | 0.04 | 2.74 | 0.82 | 1.03 |
| East(O) | 4.10 | 3.43 | 0.84 | 2.05 | 0.08 | 3.27 | 0.61 | 0.77 |
| East(E) | 4.93 | 3.33 | 0.51 | 1.60 | 0.04 | 2.74 | 0.82 | 1.03 |

The chi-square test comparing eastern and western ecoregions, with fire and harvesting combined for each ecoregion(Table 6), showed no statistically significant difference in morphological composition. The observed test statistic ($\chi^2 = 1.52$, $df = 7$) was below the critical value of 14.07, indicating comparable distributions of morphological elements between regions (Figure 19)

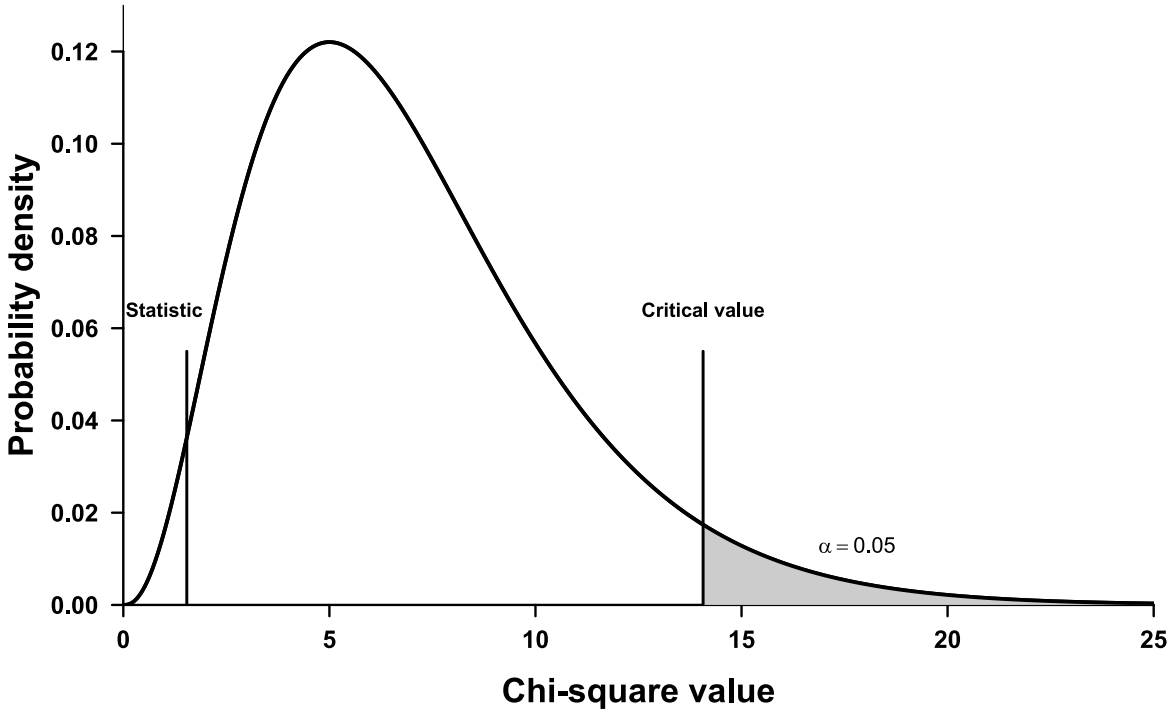


Figure 19. Chi-square distribution for the comparison of combined disturbance types (fire and harvesting) between western and eastern ecoregions. Showing the test statistic and critical value for the morphological class proportion comparison.

Table 7. Contingency table of observed (O) proportions for morphological classes by disturbance type, western and eastern ecoregions

| DistType | MASS | SKIN | CRUMB | CIRCUIT | ANTENNA | BOND | VVOL | VOID |
|---|---|---|---|---|---|---|---|---|
| Fire (W(O)) | 3.55 | 2.07 | 0.03 | 0.52 | 0.01 | 0.49 | 0.09 | 0.25 |
| Fire(W(E)) | 2.82 | 2.07 | 0.20 | 0.83 | 0.02 | 0.86 | 0.05 | 0.15 |
| Fire (E(O)) | 2.50 | 2.37 | 0.40 | 1.27 | 0.02 | 1.35 | 0.02 | 0.07 |
| Fire (E(E)) | 3.23 | 2.37 | 0.23 | 0.95 | 0.02 | 0.98 | 0.06 | 0.17 |

Table 8. Contingency table of observed (O) and expected (E) proportion for morphological classes by disturbance type, western and eastern ecoregions

| DistType | MASS | SKIN | CRUMB | CIRCUIT | ANTENNA | BOND | VVOL | VOID |
|---|---|---|---|---|---|---|---|---|
| Harvest(W(O)) | 2.66 | 2.35 | 0.16 | 0.68 | 0.03 | 1.86 | 0.07 | 0.20 |
| Harvest(W(E)) | 2.77 | 2.23 | 0.33 | 0.95 | 0.02 | 0.98 | 0.07 | 0.20 |
| Harvest(E(O)) | 1.60 | 1.84 | 0.46 | 0.84 | 0.03 | 2.12 | 0.03 | 0.09 |
| Harvest(E(E)) | 1.99 | 1.95 | 0.29 | 0.81 | 0.03 | 2.12 | 0.06 | 0.15 |

To further examine whether regional differences varied by disturbance type, separate chi-square tests of homogeneity were conducted for wildfire (Table 7)and harvesting sites(Table 8). In each case, the test compared the aggregated proportions of the eight morphological classes between the western and eastern ecoregions within a single disturbance type. The null hypothesis ($H_0$) stated that the proportional distribution of morphological classes was the same in both ecoregions, whereas the alternative hypothesis ($H_1$) stated that at least one class proportion differed between ecoregions. For fire-disturbed sites, the results indicated no statistically significant difference in morphological composition between western and eastern ecoregions, with the test statistic ($\chi^2 = 1.33$, $df = 7$) not exceeding the critical value of 14.07 at $\alpha = 0.05$ (Figure 20) Similarly, for harvesting sites, no statistically significant difference was detected between ecoregions, as the test statistic ($\chi^2 = 0.56$, $df = 7$) also did not exceed the critical value (Figure 21). Overall, these results indicate that, after pooling site-level proportions within each disturbance type, the relative distribution of morphological classes was statistically similar between western and eastern ecoregions.

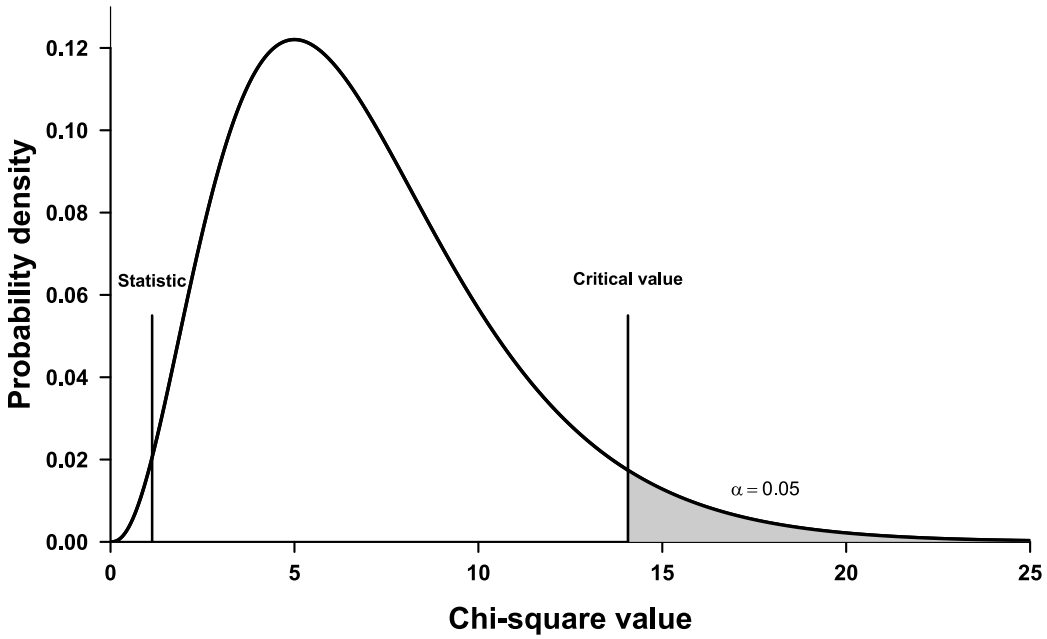


Figure 20. Chi-square distribution showing the test statistic and critical value for the morphological class frequency comparison of fire-disturbed sites across the eastern and western ecoregions.

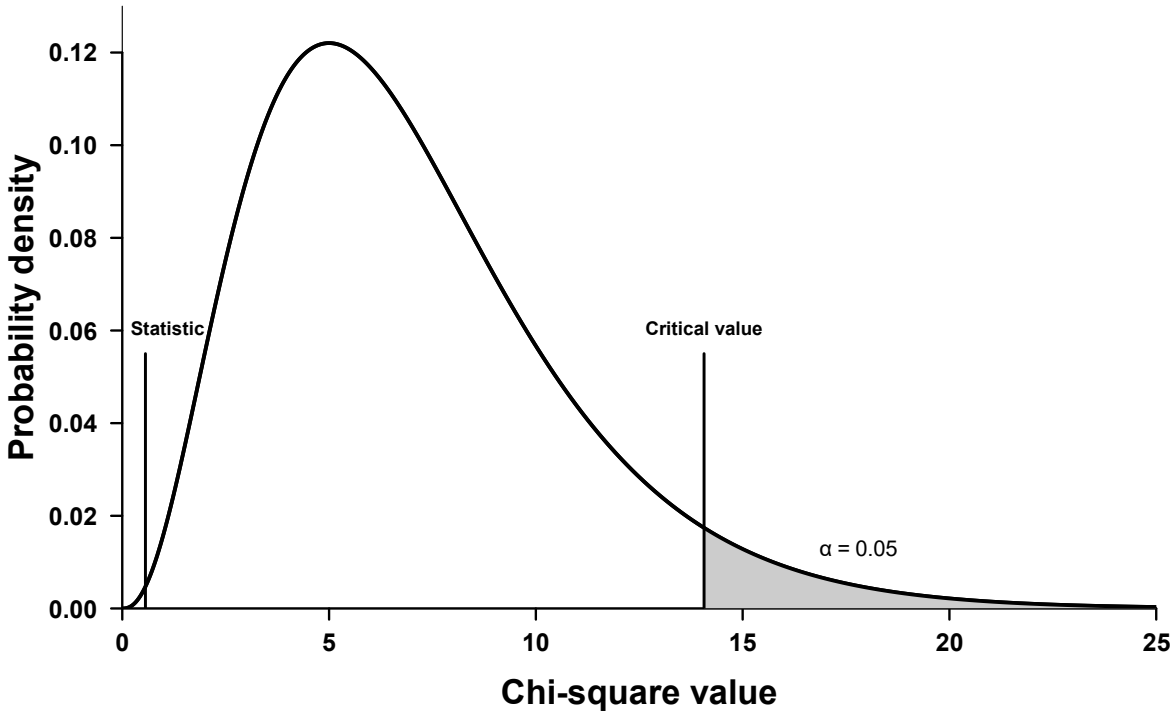


Figure 21. Chi-square distribution showing the test statistic and critical value for the morphological class frequency comparison of harvested sites across the eastern and western ecoregions.

Table 9. Independent-samples *t*-test results comparing mean morphological class proportions between western and eastern boreal ecoregions.

| MorphClass | Mean_West | Mean_East | *t*_value | *df* | *p*-value |
|---|---|---|---|---|---|
| MASS | 0.4140 | 0.2720 | 3.1927 | 28 | 0.0034 |
| SKIN | 0.2940 | 0.2800 | -0.6626 | 28 | 0.5130 |
| CRUMB | 0.0107 | 0.0573 | -4.3665 | 28 | 0.0002 |
| CIRCUIT | 0.0793 | 0.1407 | -2.3294 | 28 | 0.0273 |
| ANTENNA | 0.0007 | 0.0027 | -1.4739 | 28 | 0.1516 |
| BOND | 0.1567 | 0.2307 | -1.5322 | 28 | 0.1367 |
| VOID-VOLUME | 0.0100 | 0.0020 | 5.5268 | 28 | 0.0000 |
| VOID | 0.0300 | 0.0093 | 4.9280 | 28 | 0.0000 |

Independent-samples *t*-tests comparing western and eastern sites confirmed significant regional differences for several classes Table 9. MASS classes were higher at western sites, indicating more consolidated and internally structured morphology. In contrast, CRUMB and

CIRCUIT were higher at eastern sites, reflecting greater fragmentation and connectivity. No significant differences were observed for the remaining classes.

Multivariate analyses further supported these patterns. A MANOVA detected a significant effect of disturbance type on the combined morphological composition (Wilks' lambda = 0.450, $p = 0.0152$) and a significant effect of ecoregion (Wilks' lambda = 0.399, $p = 0.0054$), indicating that both disturbance processes and regional context influence the overall distribution of morphological classes.

Distributional divergence metrics showed consistent patterns. Symmetric Kullback–Leibler divergence indicated modest separation between wildfire and harvesting compositions (KLD = 0.083) and stronger separation between western and eastern regional compositions (KLD = 0.122), suggesting that structural differences are expressed through coordinated shifts across multiple classes rather than extreme changes in a single class.

These results confirm that both disturbance type and ecoregion contribute to differences in overall morphological composition at the site level. However, these between-group comparisons indicate whether overall morphological distributions differ between categories, but they do not identify which specific morphological classes contribute to those differences or whether morphological structures are consistently expressed among sites within the same disturbance category. The following section shifts the focus from between-group differences to the assessment of within-disturbance structural consistency.

### 3.3 Morphological structures consistency and variability among disturbance types

Morphological structures were examined to determine whether consistent patterns exist among disturbance types by evaluating variability in structural composition across individual sites within the same disturbance category. Rather than comparing average proportions between wildfire and harvesting sites, this analysis focuses on the degree of internal heterogeneity within each disturbance group. Consistent structural patterns indicate that a given disturbance type produces a characteristic regeneration pattern, whereas high variability suggests that site-specific conditions and local variability dominate in shaping post-disturbance structure through time.

Multivariate analyses were applied to site-level morphological compositions derived from three-dimensional voxel segmentation to evaluate both overall group differences and within-group structural variability. A two-factor multivariate analysis of variance (MANOVA) was conducted to assess the effects of disturbance type, ecoregion, and their interaction on

multivariate morphological composition. Results indicated significant main effects of disturbance type (Wilks' lambda = 0.44, $p = 0.023$) and ecoregion (Wilks' lambda = 0.36, $p = 0.004$), indicating that both disturbance processes and regional context significantly influenced overall morphological structure. However, the interaction between disturbance type and ecoregion was not statistically significant (Wilks' lambda = 0.71, $p = 0.494$), suggesting that the influence of disturbance on morphological composition remained consistent across regions. These results indicate that disturbance type and ecoregion independently affected multivariate morphological composition, but their effects did not interact.

MANOVA confirms differences in multivariate group centroids, but it does not measure structural consistency within groups. Therefore, multivariate dispersion analyses were conducted to directly evaluate morphological consistency among disturbance vectors. Morphological consistency was quantified using multivariate dispersion (PERMDISP), based on Bray–Curtis dissimilarity of morphological proportion profiles. Distances to group centroids represent within-group variability, with lower distances indicating greater structural consistency.

PERMDISP results showed that wildfire-disturbed sites exhibited lower distances to the group centroid than harvested sites Figure 22 , indicating greater within-group consistency in morphological structure following wildfire disturbance. In contrast, harvested sites displayed higher dispersion, reflecting greater heterogeneity in post-disturbance morphology. Permutation tests confirmed that differences in dispersion between disturbance types were statistically significant ($p < 0.05$), supporting the interpretation that disturbance type influences morphological consistency.

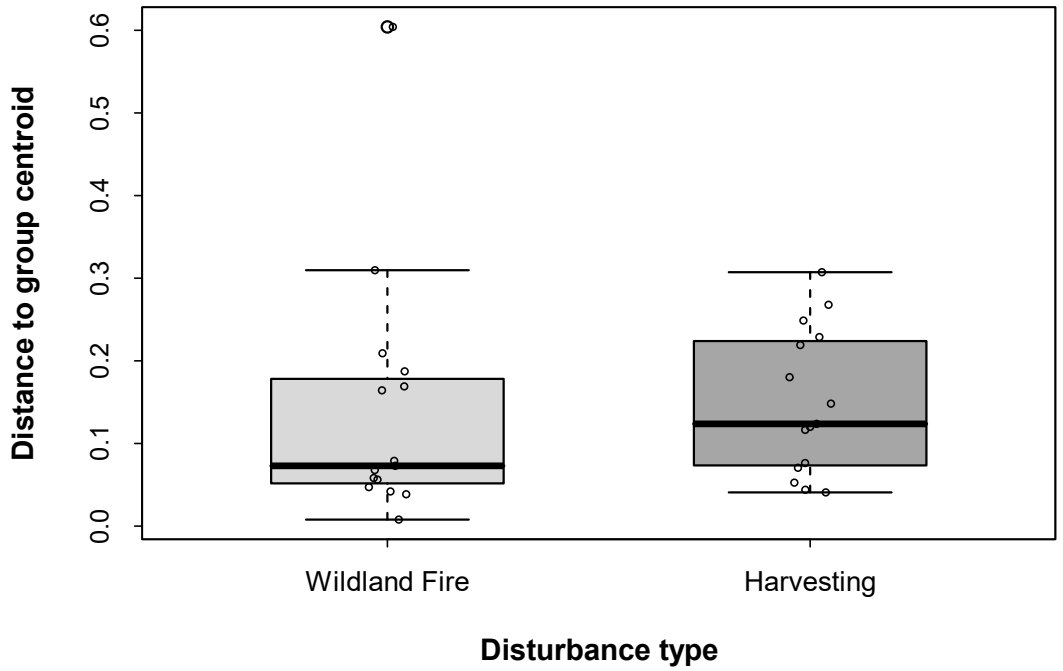


Figure 22. Multivariate dispersion of morphological structure by disturbance type (wildfire and harvesting), showing distances of sites to their respective group centroids.

Ecoregion dispersion analysis showed smaller differences between western and eastern sites Figure 23. Median distances to the centroid were slightly higher for eastern sites, indicating marginally greater variability. However, substantial overlap in interquartile ranges suggests that within-group variability is broadly similar across regions. These results indicate that regional factors influence structural variability, but less strongly than disturbance processes. Disturbance type, therefore, appears to play the dominant role in determining morphological consistency.

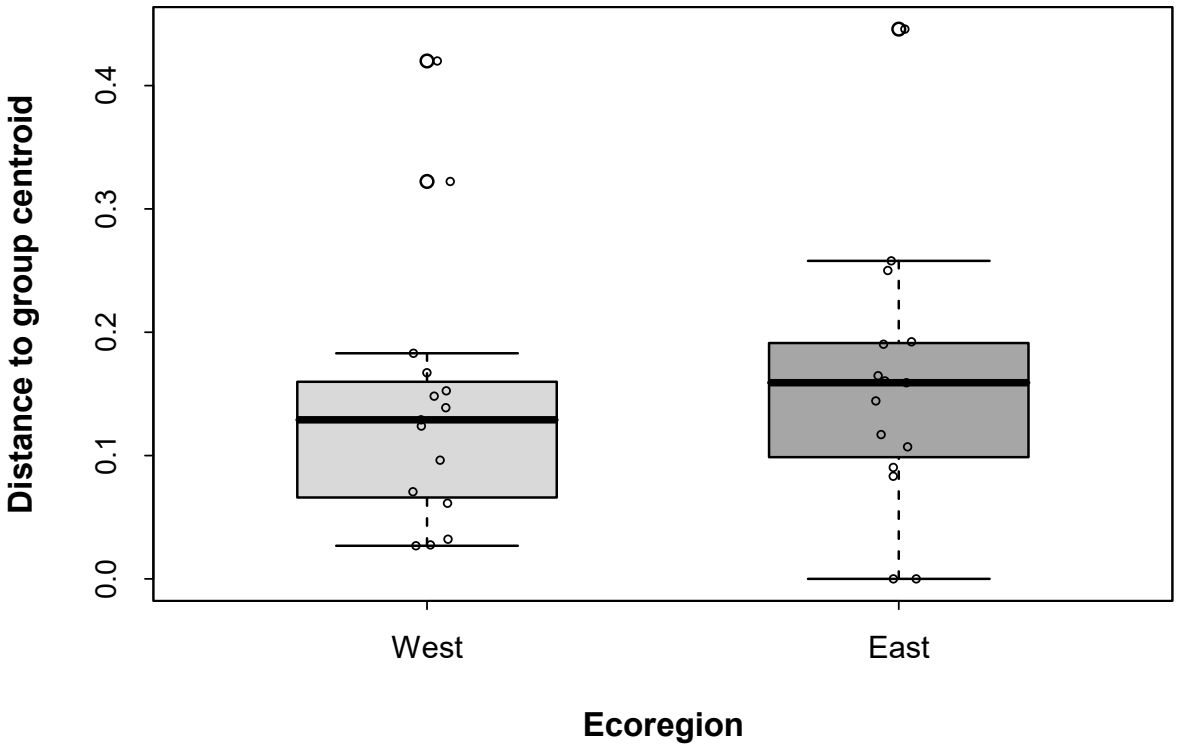


Figure 23. Multivariate dispersion of morphological structure by western and eastern ecoregions, showing distances of sites to their respective group centroids.

To further examine how disturbance and regional context jointly influence structural variability, multivariate dispersion was evaluated across four disturbance–ecoregion subgroups (Fire–West, Fire–East, Harvest–West, and Harvest–East). This analysis assessed whether variability in morphological structure differs among these combined categories. Differences in distances to group centroids represent variation in structural consistency across subgroups.

Results show that wildfire sites in both regions are closer to the centroid, indicating greater structural consistency, whereas harvested sites exhibit greater dispersion, reflecting greater variability in post-disturbance morphology. Differences between western and eastern subgroups are present but less pronounced than those observed between disturbance types, reinforcing the dominant role of disturbance processes in shaping structural consistency.

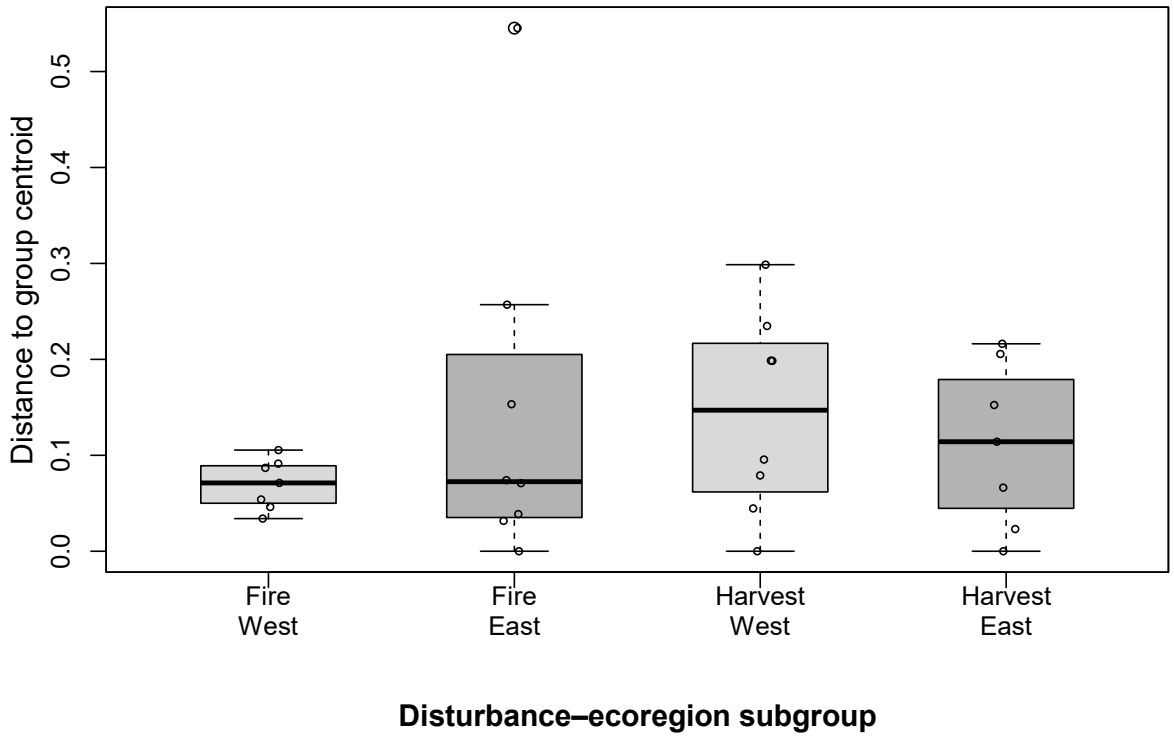


Figure 24. Multivariate dispersion of morphological structure across disturbance–ecoregion subgroups, showing distances of sites to group centroids for fire–west, fire–east, harvest–west, and harvest–east ecoregions.

Principal Coordinates Analysis (PCoA)(Gower, 1966) provided a visual representation of multivariate morphological relationships among sites (Figure 25). Sites grouped by disturbance type showed substantial overlap but moderate spatial separation, with wildfire sites appearing more tightly clustered around their centroid. whereas harvested sites show a greater spread, indicating higher variability. This pattern is consistent with dispersion results, suggesting that wildfire disturbances produce more structurally consistent outcomes compared to harvesting. PCoA by ecoregion (Figure 26) also showed considerable overlap between eastern and western sites, with only limited separation. This indicates that regional differences in morphological structure are less pronounced than the variability associated with disturbance type.

Together, these results indicate that morphological structures are not equally consistent among disturbance types. While both wildfire and harvesting influence the overall morphological composition, wildfire-disturbed sites exhibit greater internal consistency, whereas harvesting produces more heterogeneous morphological outcomes.

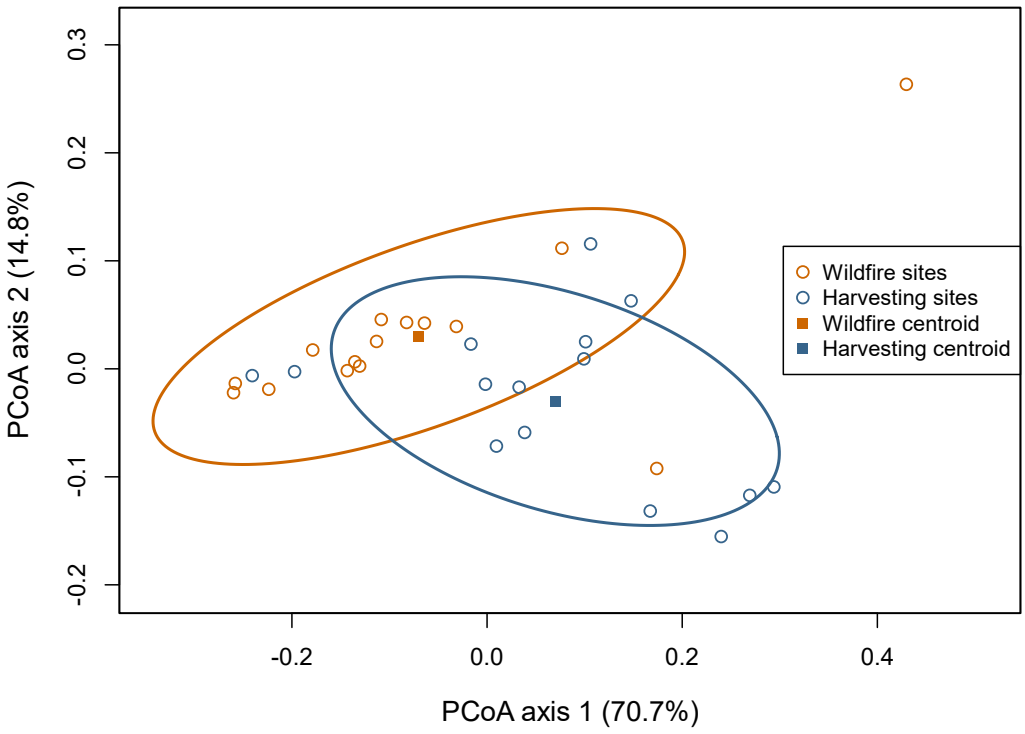


Figure 25. PCoA ordination of morphological regeneration profiles by disturbance types.

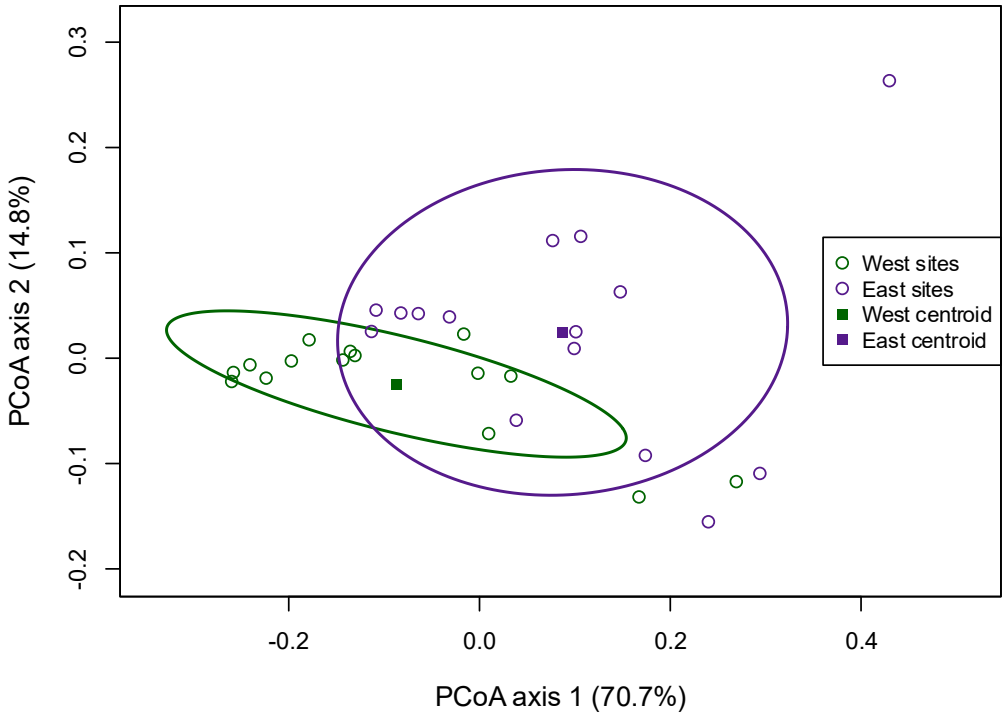


Figure 26. PCoA ordination of morphological regeneration profiles by ecoregions.

### 3.4 Contribution of the temporal dimension

The incorporation of time as a third axis in the voxel segmentation revealed temporal patterns that are not apparent in single-year or two-dimensional analyses. By extending the analysis across consecutive years, it becomes possible to observe how morphological classes develop, persist, or diminish following disturbance. This temporal perspective captures the progression of landscape structure rather than a single static condition.

Across all sites, the inclusion of temporal depth altered the distribution of several morphological classes. MASS remained the dominant structural component throughout the study period, while BOND increased in relative contribution in multiple sites over time. In contrast, CRUMB, CIRCUIT, and VOID-VOLUME exhibited greater variability, with intermittent increases and decreases across years. These classes were more sensitive to temporal fluctuations and did not follow a consistent trajectory across all sites.

Figure 27 shows temporal trajectories of morphological class composition for wildfire and harvested sites from 1990 to 2000. In wildfire sites (Figure 27a-b), 1990 is characterized by high contributions from SKIN, CIRCUIT, and BOND. MASS becomes evident from 1991 and increases between 1993 and 1996, declines in 1997, increases again in 1998, decreases in 1999, and is reduced in 2000. SKIN remains present throughout the time series and varies in magnitude, with higher values in 1994, 1996, and 1998. CRUMB and ANTENNA are more prominent between 1990 and 1992 and decline after 1993. BOND and CIRCUIT persist across multiple years and show intermittent increases, particularly between 1995 and 1998. In proportional terms, wildfire sites show high initial contributions from SKIN, CIRCUIT, and BOND in 1990. MASS increases after 1991 and occupies a larger proportion between 1993 and 1996, followed by fluctuations through 1999 and a reduced contribution in 2000. SKIN maintains moderate proportions across all years, while CIRCUIT and BOND increase intermittently. CRUMB and ANTENNA decline after the early years.

In harvested sites (Figure 27c–d), 1990 is similarly dominated by SKIN, CIRCUIT, and BOND. MASS becomes evident from 1991, increases between 1993 and 1995, declines in 1996, and varies through 1999. SKIN remains present across all years, with fluctuations in magnitude. CRUMB, CIRCUIT, and VOID-related classes remain present throughout the time series, with higher contributions between 1991 and 1994 and again between 1997 and 1999. BOND contributed strongly for several years. In proportion, harvested sites show a more distributed contribution across classes. MASS increases after 1991 but does not dominate across all years

and declines toward 2000. SKIN maintains moderate contributions throughout. BOND and CIRCUIT contribute substantial proportions across multiple years, particularly between 1994 and 1999. CRUMB and VOID-related classes remain present at lower but consistent proportions across the time series.

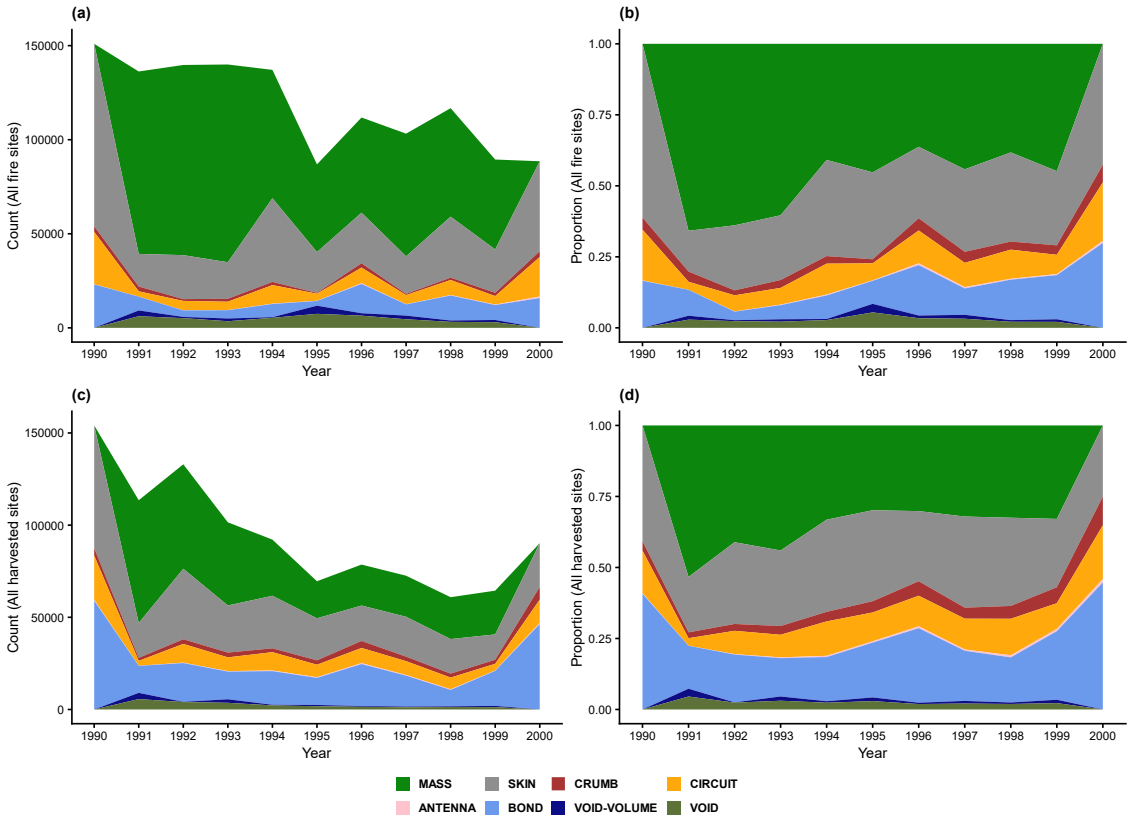


Figure 27. Temporal trajectories of morphological class composition from 1990 to 2000 for all wildfire and harvested sites. Stacked area charts show changes in mean counts and proportions of morphological classes through time: (a) wildfire counts, (b) wildfire proportions, (c) harvested counts, and (d) harvested proportions.

Temporal trajectories of morphological class composition differ between western and eastern wildfire sites in the Ontario Managed Boreal Forest (Figure 28). In both ecoregions, MASS is absent in 1990 and becomes evident from 1991 onward, after which it constitutes the largest class across most years. In western sites (Figure 28a–b), MASS increases in 1991, remains high through 1994, declines in 1995, increases again between 1996 and 1998, and decreases in 1999. SKIN is present throughout the time series and contributes substantially across all years, with lower values in 1991 and 1993 and higher values in 1994, 1996, and 1998. CIRCUIT and BOND are present across multiple years in western sites, with increases in 1990, 1995, 1998, and 2000. CRUMB and ANTENNA are more evident in the early years (1990–

1992) and remain low thereafter. In proportional terms, MASS increases from 1991, followed by fluctuations through time, while SKIN maintains a consistent contribution. CIRCUIT and BOND increase intermittently but remain lower than core classes.

Eastern wildfire sites (Figure 28c–d) show a different pattern. MASS increases from 1991, declines between 1992 and 1995, increases in 1996, declines in 1997, and increases again from 1998 to 2000. SKIN remains present across all years, with higher contributions in 1990, 1994, and 1996. BOND contributed strongly for several years, particularly in 1990, 1996, and 2000. CIRCUIT is present throughout and increases in 1994, 1996, and 2000. CRUMB remains present across multiple years and is more evident than in Western sites.

In proportion, MASS increases after 1991 but varies across years in eastern sites. SKIN maintains moderate-to-high contributions throughout the time series. BOND and CIRCUIT contributed larger proportions than in Western sites between 1994 and 2000. CRUMB also remains present across several years.

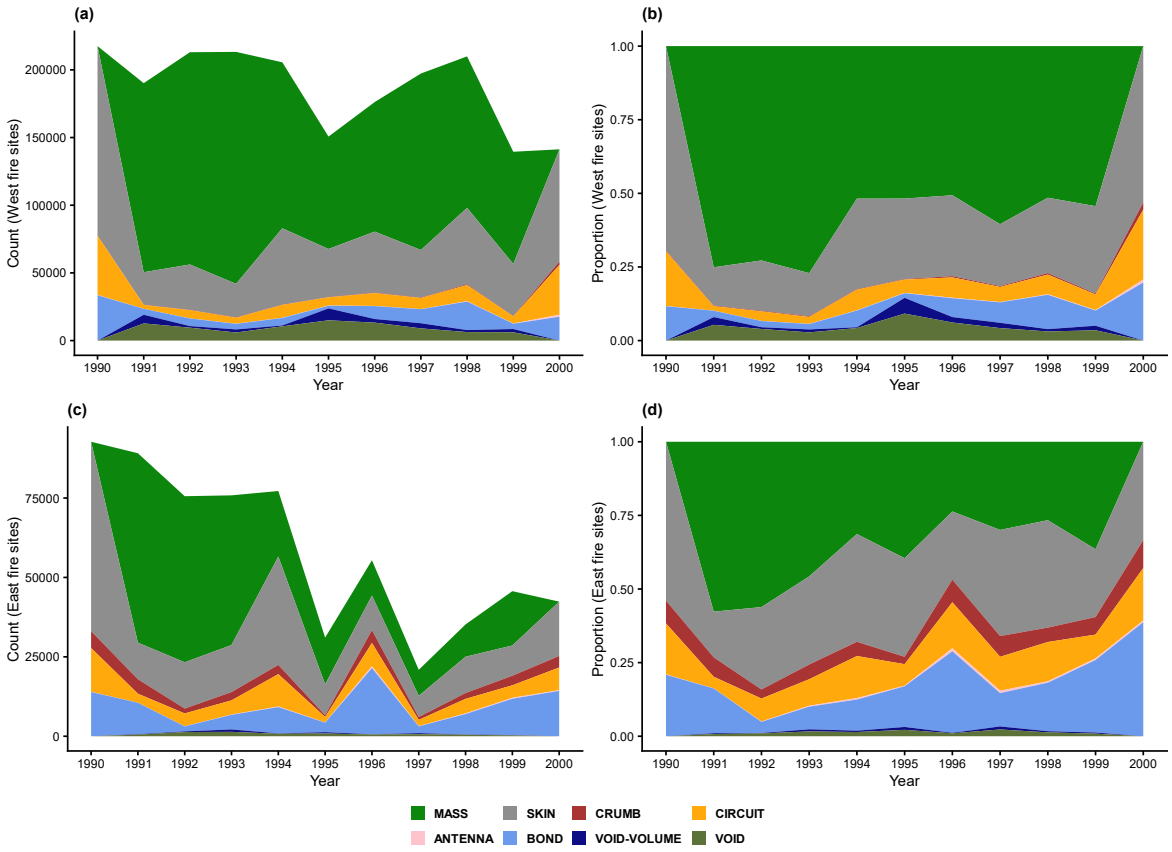


Figure 28. Temporal trajectories of morphological class composition from 1990 to 2000 across wildfire sites stratified by ecoregion. Stacked area charts show mean counts and proportions of morphological classes for western wildfire sites ((a) counts, (b) proportions) and eastern wildfire sites ((c) counts, (d) proportions).

Patterns of morphological class composition across harvested sites vary between western and eastern ecoregions (Figure 29). In western harvested sites (Figure 29a–b), the time series begins in 1990 with contributions distributed across multiple classes. From 1991 onward, MASS became evident and varied across years, with higher counts in 1992, 1994, and 1998, followed by a decline toward 1999 and absence in 2000. SKIN is present throughout the series and shows substantial variation, with higher counts in 1992 and 1994 and reduced values after 1995. BOND and CIRCUIT occur across most years, with noticeable increases in 1994 and again in 2000. CRUMB remains low but present across several years, while ANTENNA is minimal. VOID and VOID-VOLUME are present at low levels across the time series. In proportional terms, Western sites show a shift after 1991, with increasing contributions from MASS, SKIN, and BOND. Between 1993 and 1998, SKIN and BOND maintain relatively higher proportions, while CIRCUIT increases intermittently. By 2000, BOND becomes more prominent in proportion, accompanied by increases in CIRCUIT and CRUMB.

In eastern harvested sites (Figure 29c–d), MASS also emerges from 1991 and varies across years, with increases in 1992 and 1993, declines between 1994 and 1998, and absence in 2000. SKIN contributes substantially to early years and fluctuates through time. BOND shows strong contributions in several years, particularly 1996 and 2000. CIRCUIT and CRUMB are present across most years with moderate counts, while ANTENNA remains minimal.

In proportion, eastern sites show greater contributions from BOND and CIRCUIT relative to MASS. BOND is prominent between 1995 and 1997 and again in 2000. MASS contributes after 1991 but declines toward 1999 and is not evident in 2000. SKIN maintains moderate proportions across years, while CIRCUIT and CRUMB persist from 1993 onward. VOID and VOID-VOLUME remain low but consistent.

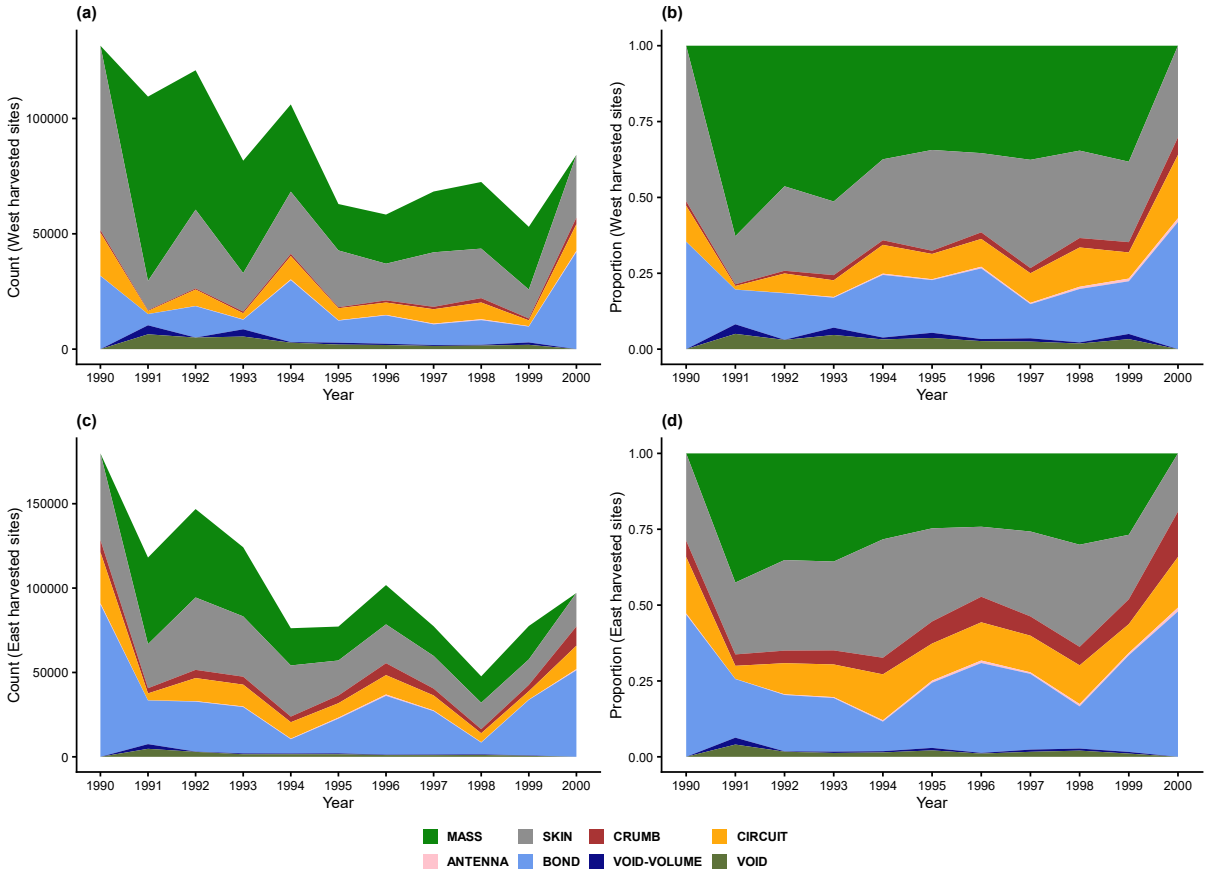


Figure 29. Temporal trajectories of morphological class composition from 1990 to 2000 across harvested sites stratified by ecoregion. Stacked area charts show mean counts and proportions of morphological classes for western harvested sites ((a) counts, (b) proportions) and eastern harvested sites ((c) counts, (d) proportions).

Variation in temporal trajectories among individual wildfire sites is shown in Figure *30* - Figure *34*. A general pattern emerged across all sites, 1990 shows higher contributions from SKIN, CIRCUIT, and BOND, while MASS becomes evident from 1991 onward. From 1991 to 1994, several sites (Figure 30, Figure 31 ) show increases in MASS, followed by fluctuations through the remaining years. In many sites, MASS decreases around 1995, increases again between 1996 and 1998, and declines toward 1999, with reduced contribution in 2000.

SKIN is present across all years and sites and shows substantial variability, with higher contributions in 1994, 1996, and 1998 at several sites. CRUMB and ANTENNA are more evident in the early years (1990–1992) and decline at most sites after 1993, although small contributions persist in some sites in later years (e.g., FS08, FS14).

CIRCUIT and BOND are present throughout the time series across all sites and exhibit intermittent increases. In several sites (e.g., Figure 32 and Figure 33 ), CIRCUIT increases during intermediate years such as 1994, 1996, and 1998. BOND shows notable increases in later

years in some sites, particularly toward 1998–2000 (e.g., FS08, FS09, FS11). VOID and VOID-VOLUME remain low across all sites but are present intermittently.

In proportional terms, MASS accounts for a large share of the composition at most sites since 1991, although its dominance varies. Some sites (e.g., Figure 30, Figure 34) show consistently higher proportions of MASS across multiple years, while others (e.g., Figure 33) show greater contributions from BOND and CIRCUIT in intermediate and later years. SKIN maintains moderate proportions across all sites and years. CRUMB and ANTENNA decline after the early years, while CIRCUIT and BOND contribute intermittently, particularly between 1994 and 2000.

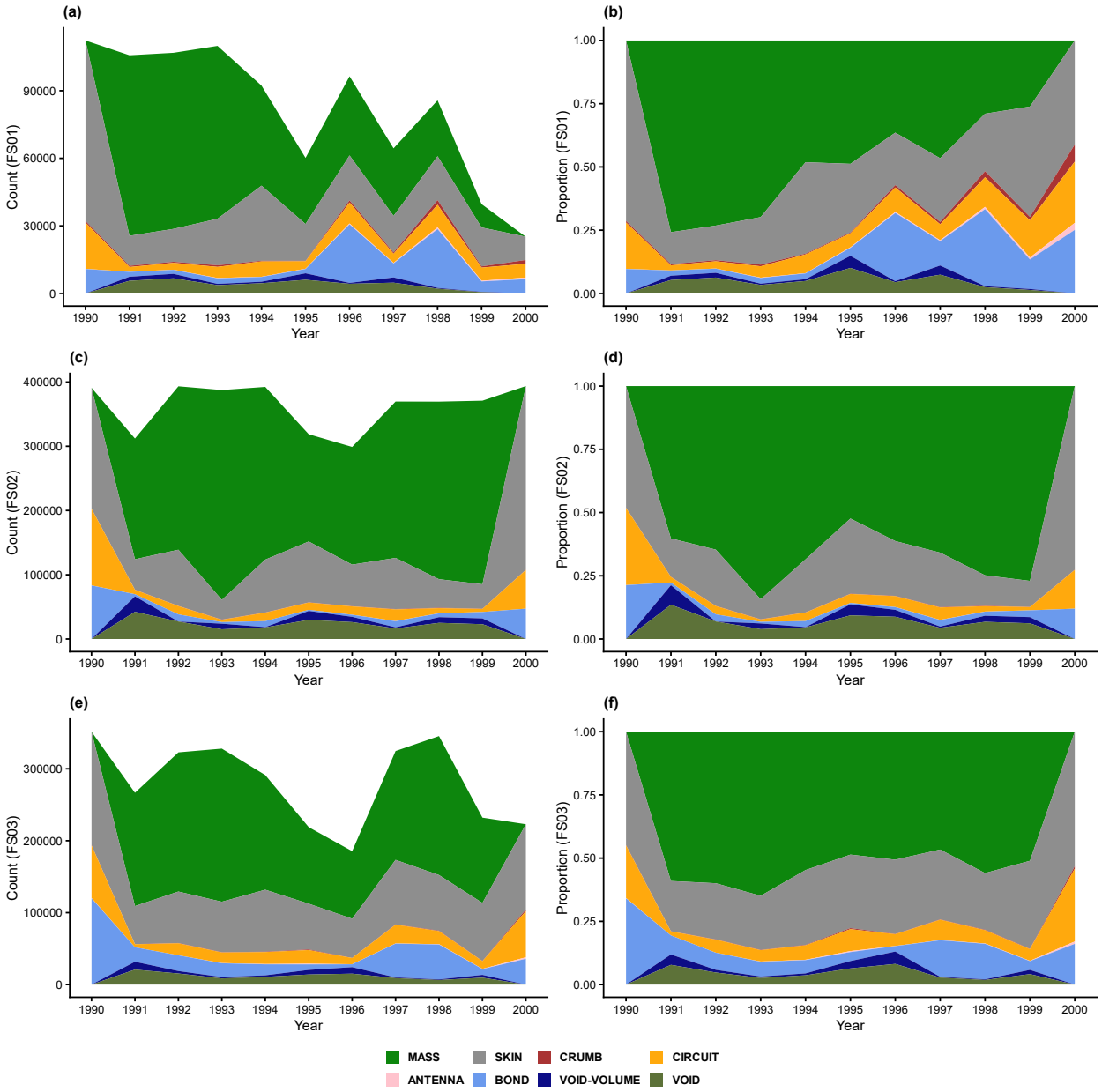


Figure 30. Temporal trajectories of morphological class composition for wildfire sites FS01–FS03 over the study period (1990–2000). Panels (a), (c), and (e) show counts, and panels (b), (d), and (f) show proportions for each site.

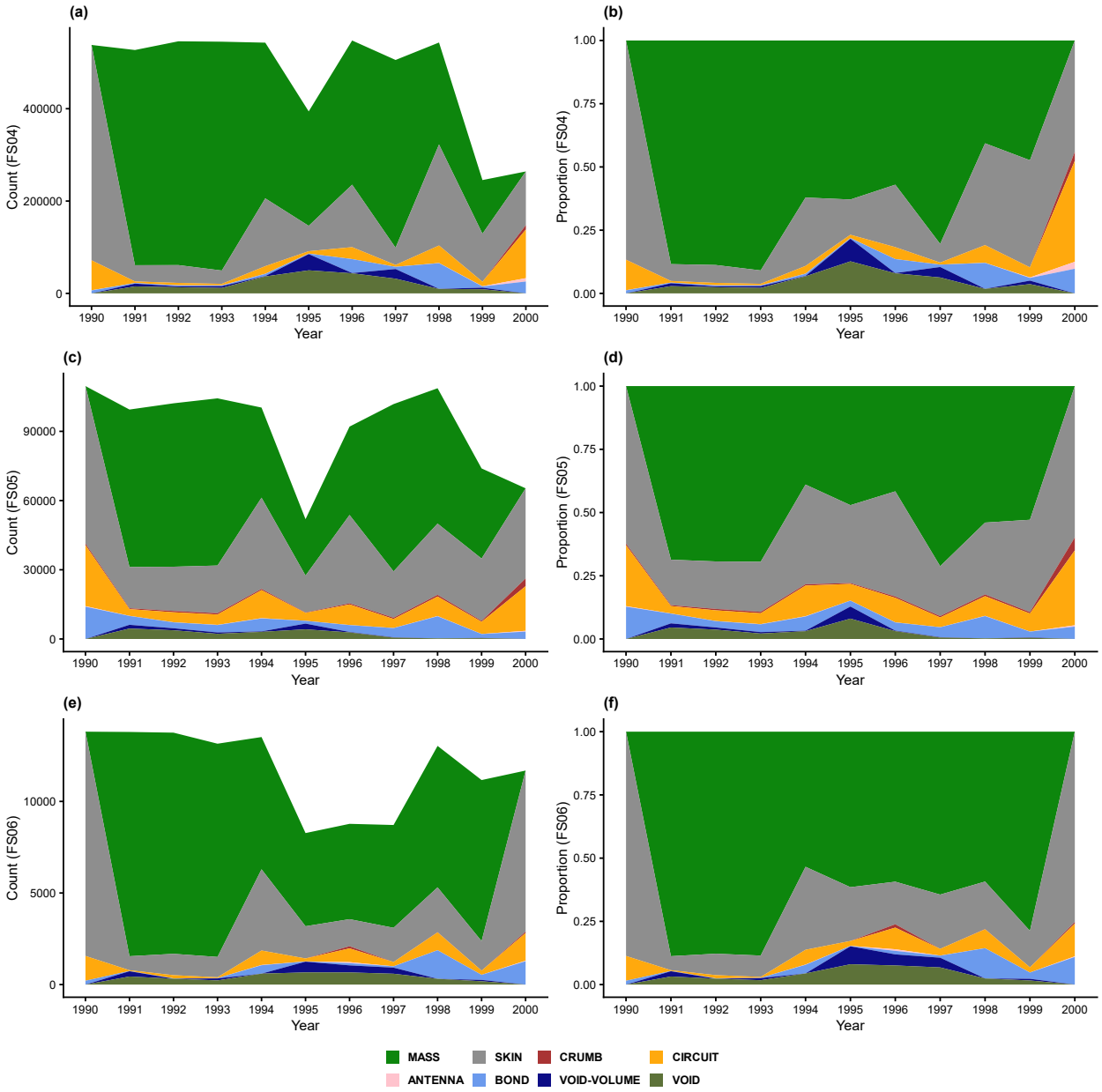


Figure 31. Temporal trajectories of morphological class composition for wildfire sites FS04–FS06 over the study period (1990–2000). Panels (a), (c), and (e) show counts, and panels (b), (d), and (f) show proportions for each site.

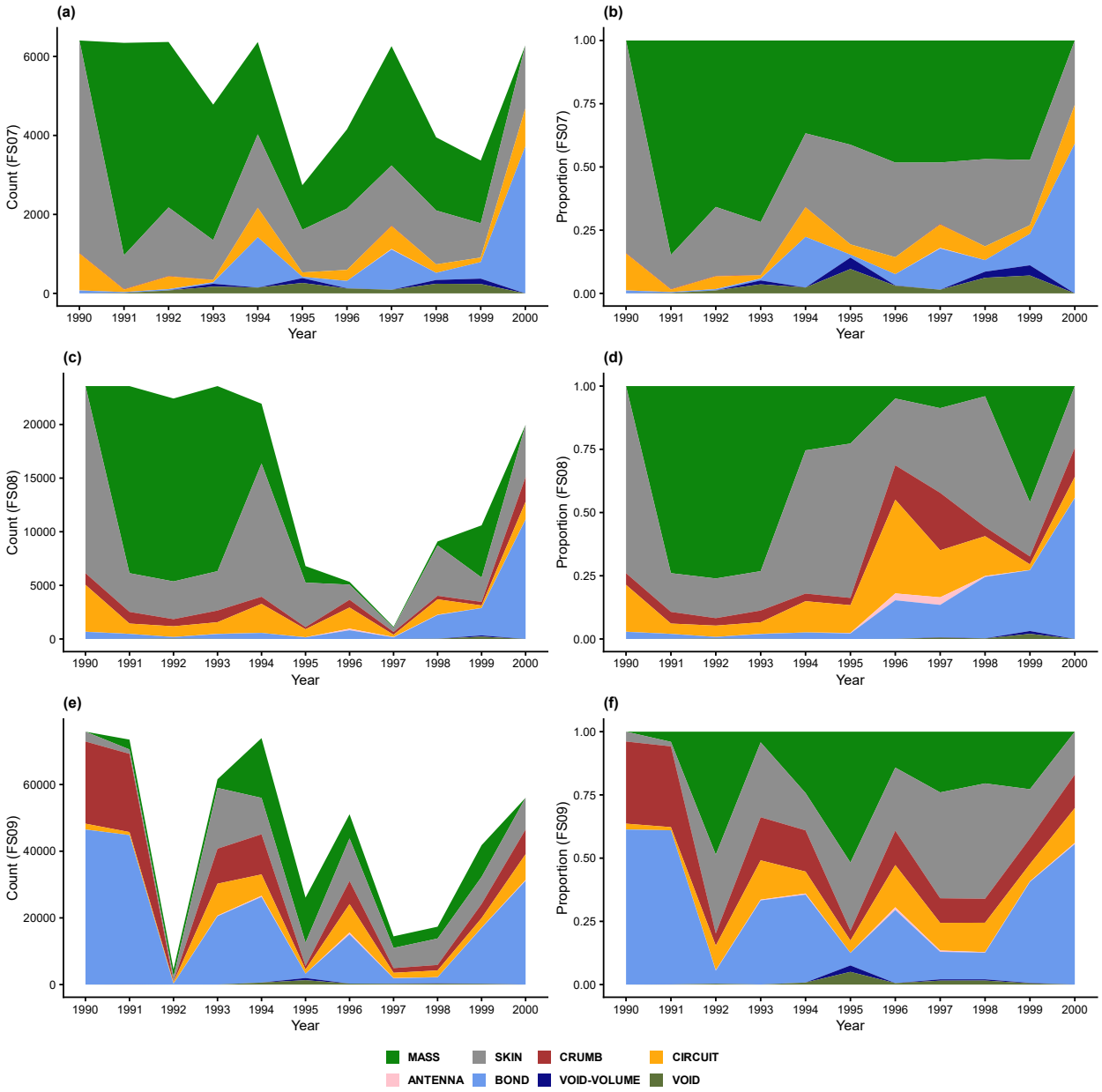


Figure 32. Temporal trajectories of morphological class composition for wildfire sites FS07–FS09 over the study period (1990–2000). Panels (a), (c), and (e) show counts, and panels (b), (d), and (f) show proportions for each site.

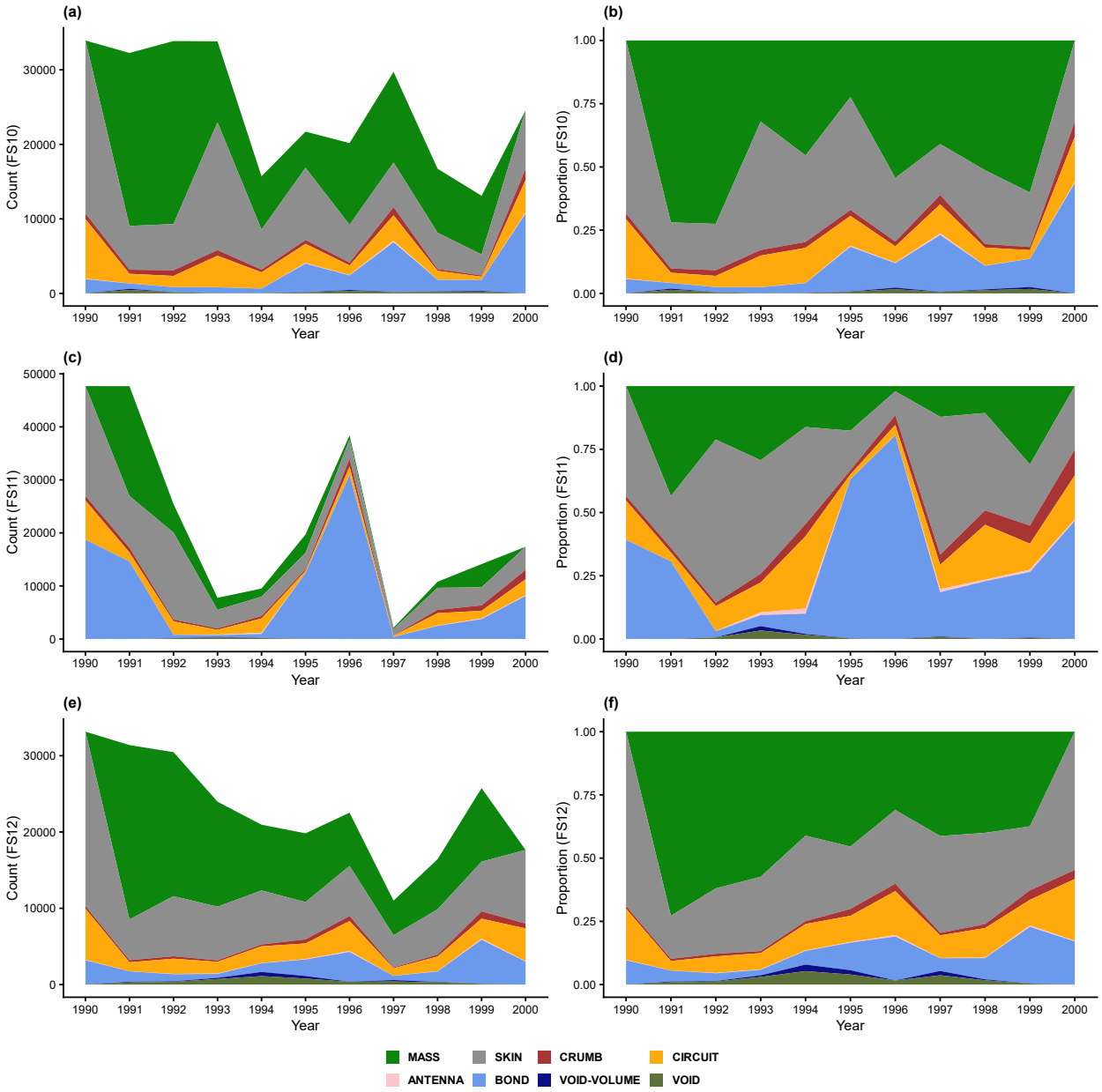


Figure 33. Temporal trajectories of morphological class composition for wildfire sites FS10–FS12 over the study period (1990–2000). Panels (a), (c), and (e) show counts, and panels (b), (d), and (f) show proportions for each site.

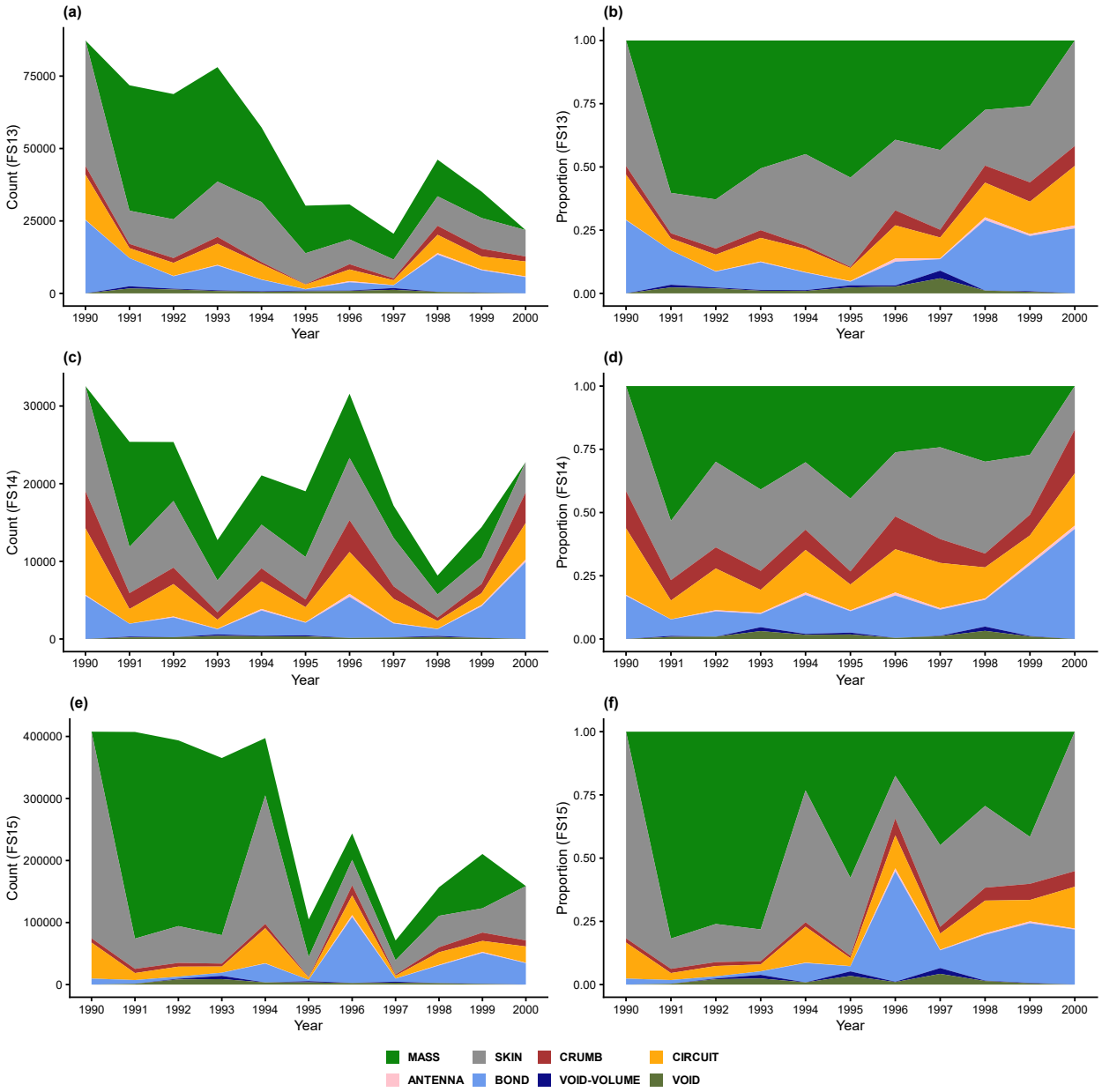


Figure 34. Temporal trajectories of morphological class composition for wildfire sites FS13–FS15 over the study period (1990–2000). Panels (a), (c), and (e) show counts, and panels (b), (d), and (f) show proportions for each site.

Temporal trajectories for individual harvested sites are shown in Figure 33-Figure 37 and display substantial variability across sites and years. In 1990, higher contributions from SKIN, CIRCUIT, and BOND are observed across most sites, while MASS becomes more evident from 1991 onward. From 1991 to 1994, several sites (e.g., Figure 35) show increases in MASS, although this pattern is inconsistent. In many sites, MASS fluctuates rather than increasing steadily, with noticeable reductions around 1995–1997 and increases again toward

1998. In some sites (e.g., Figure 37 and Figure 38 ), MASS remains lower for extended periods, with other classes contributing more prominently.

SKIN is present across all years and all harvested sites and exhibits substantial variability, with higher contributions in 1993, 1995, and 1997 at multiple sites. CRUMB and ANTENNA are more evident in the early years (1990–1992) but persist longer at several harvested sites than at wildfire sites, with visible contributions extending into later years (e.g., HS08, HS12, HS15). CIRCUIT and BOND show pronounced variability across sites and years. CIRCUIT increases intermittently, particularly in mid to later years (e.g., 1994, 1996, and 1998). BOND shows notable increases in several sites in later years, especially toward 1998–2000 ( Figure 39). VOID and VOID-VOLUME remain low overall but are intermittently present across multiple years.

In proportional terms, MASS occupies a large share of the composition at many sites after 1991 but shows greater fluctuations than at wildfire sites. Some sites (Figure 36) exhibit relatively high proportions of MASS across multiple years, while others (Figure 37 and Figure 38 ) show higher proportional contributions from BOND and CIRCUIT, particularly in intermediate and later years. SKIN maintains moderate proportions across all sites and years. CRUMB and ANTENNA decline after the early years but remain present in several sites. CIRCUIT and BOND contribute intermittently and, in some cases, dominate proportions in later years.

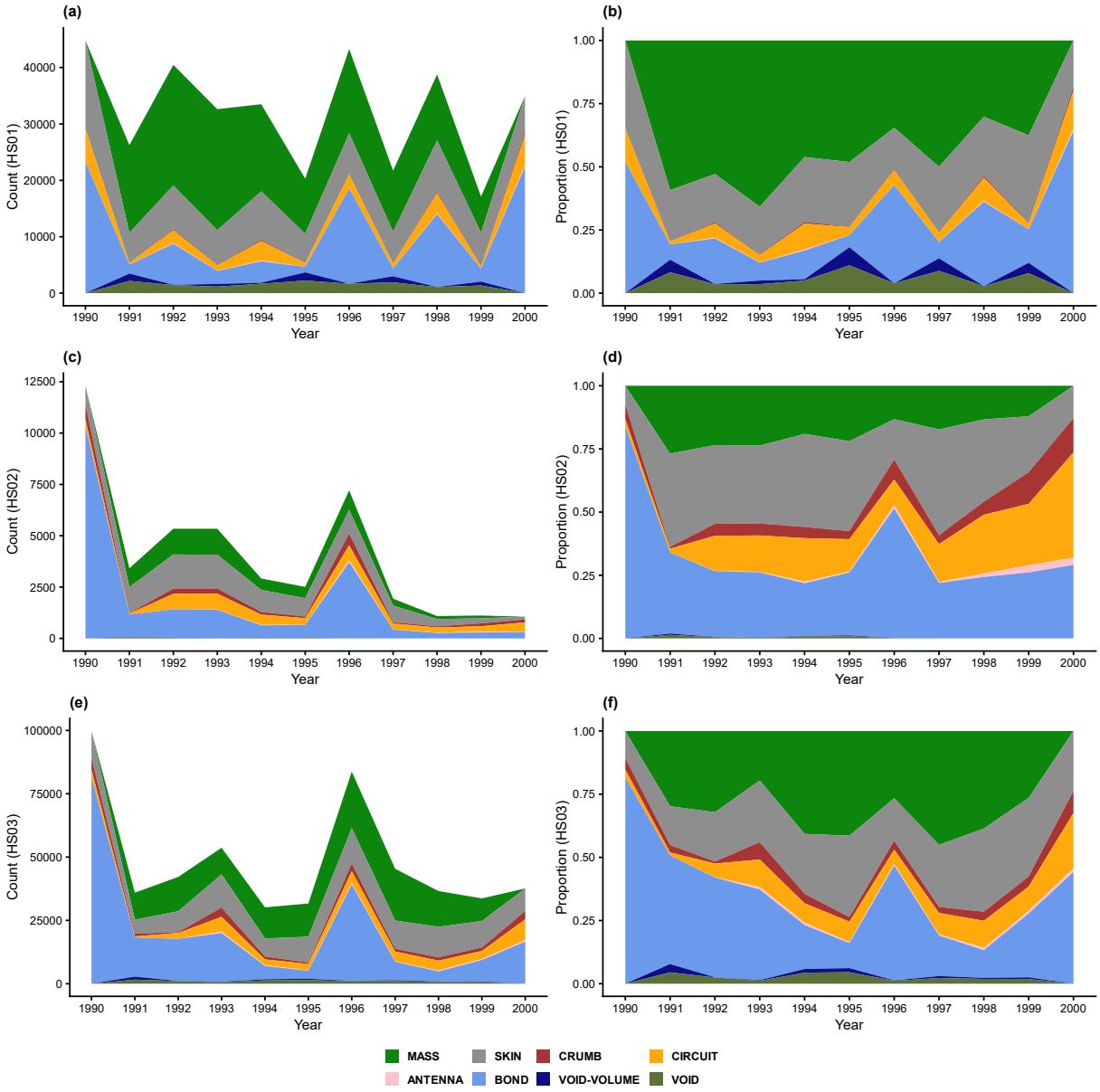


Figure 35. Temporal trajectories of morphological class composition for wildfire sites HS01–HS03 over the study period (1990–2000). Panels (a), (c), and (e) show counts, and panels (b), (d), and (f) show proportions for each site.

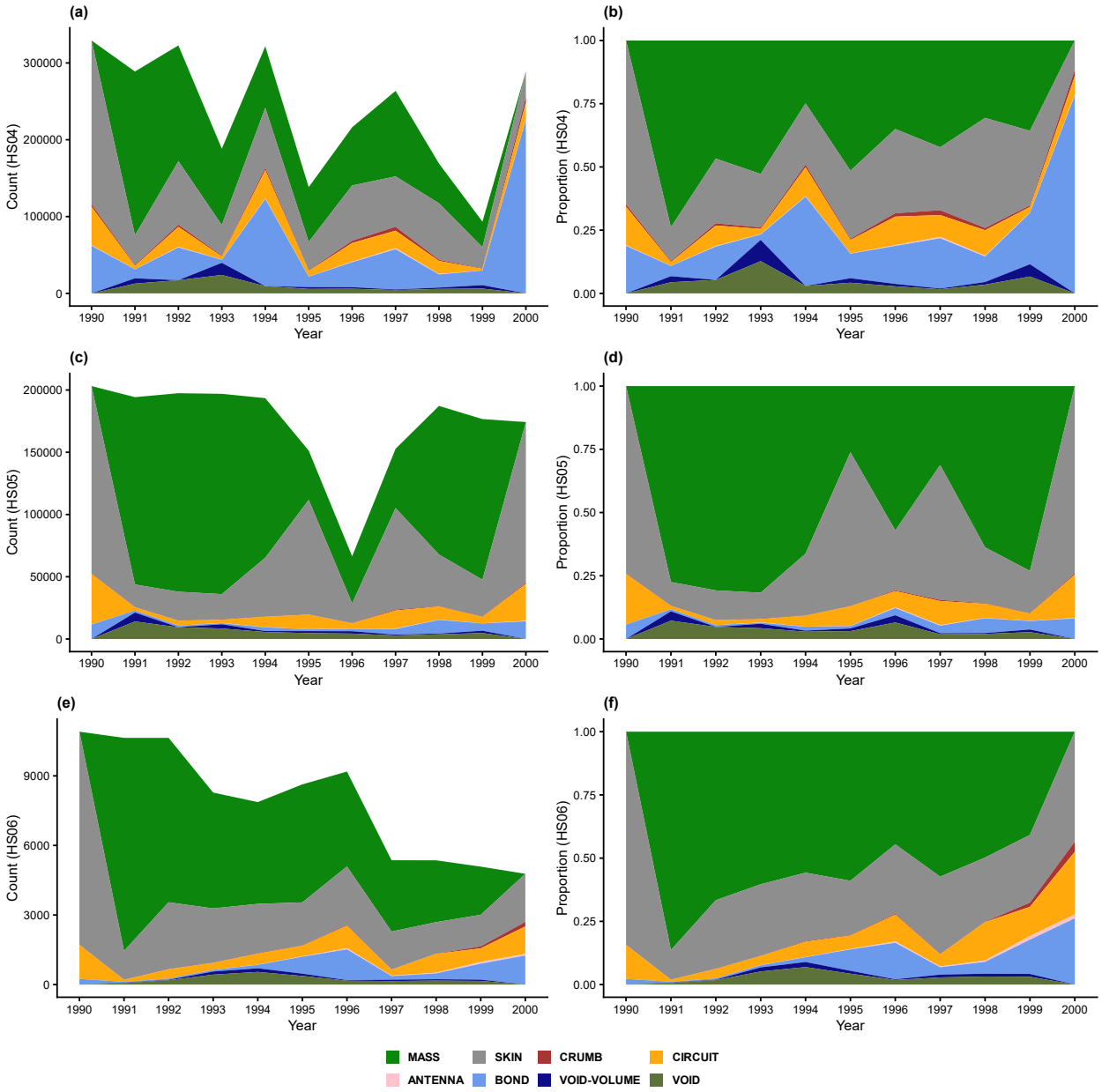


Figure 36. Temporal trajectories of morphological class composition for wildfire sites HS04–HS06 over the study period (1990–2000). Panels (a), (c), and (e) show counts, and panels (b), (d), and (f) show proportions for each site.

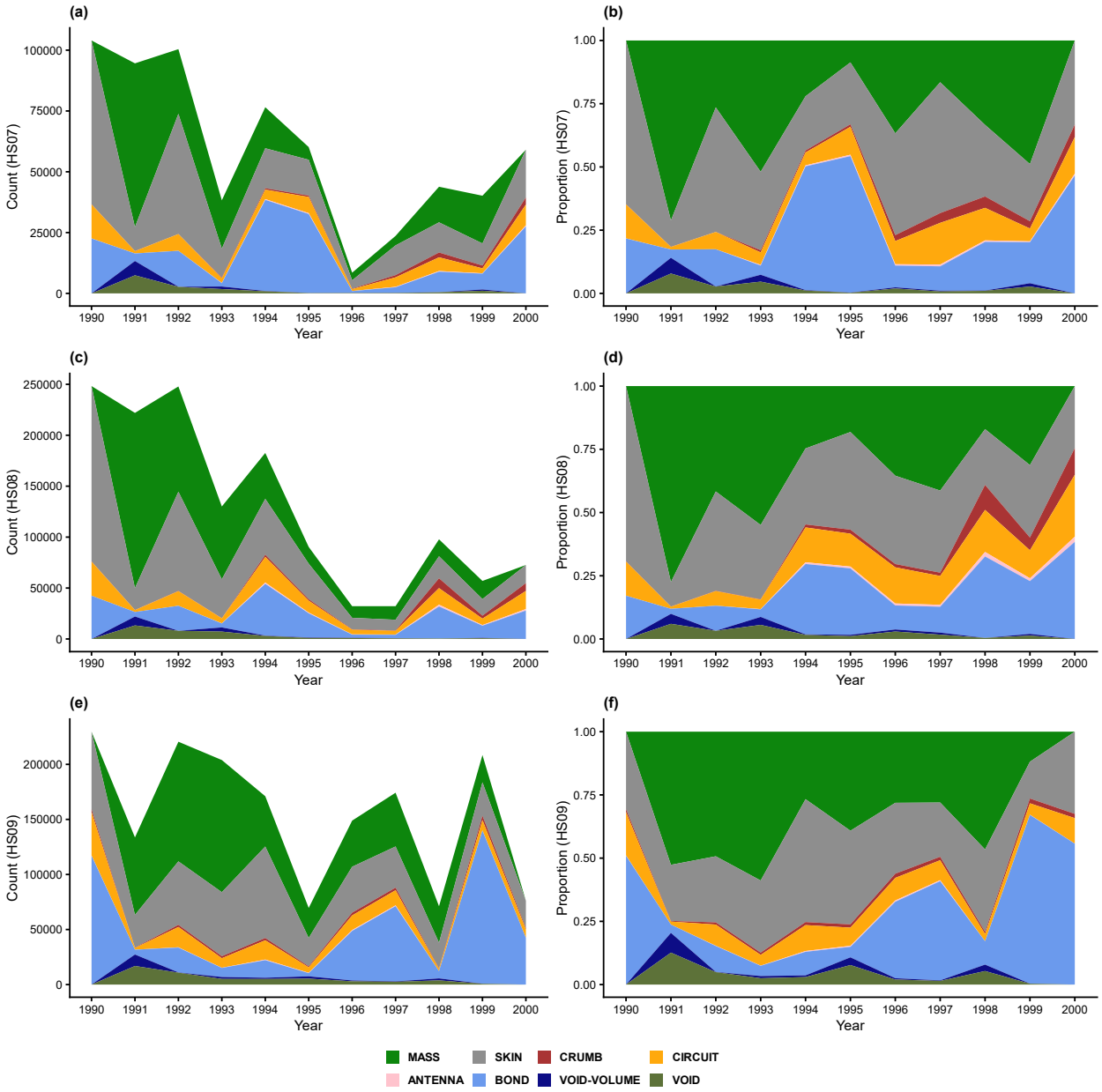


Figure 37. Temporal trajectories of morphological class composition for wildfire sites HS07–HS09 over the study period (1990–2000). Panels (a), (c), and (e) show counts, and panels (b), (d), and (f) show proportions for each site.

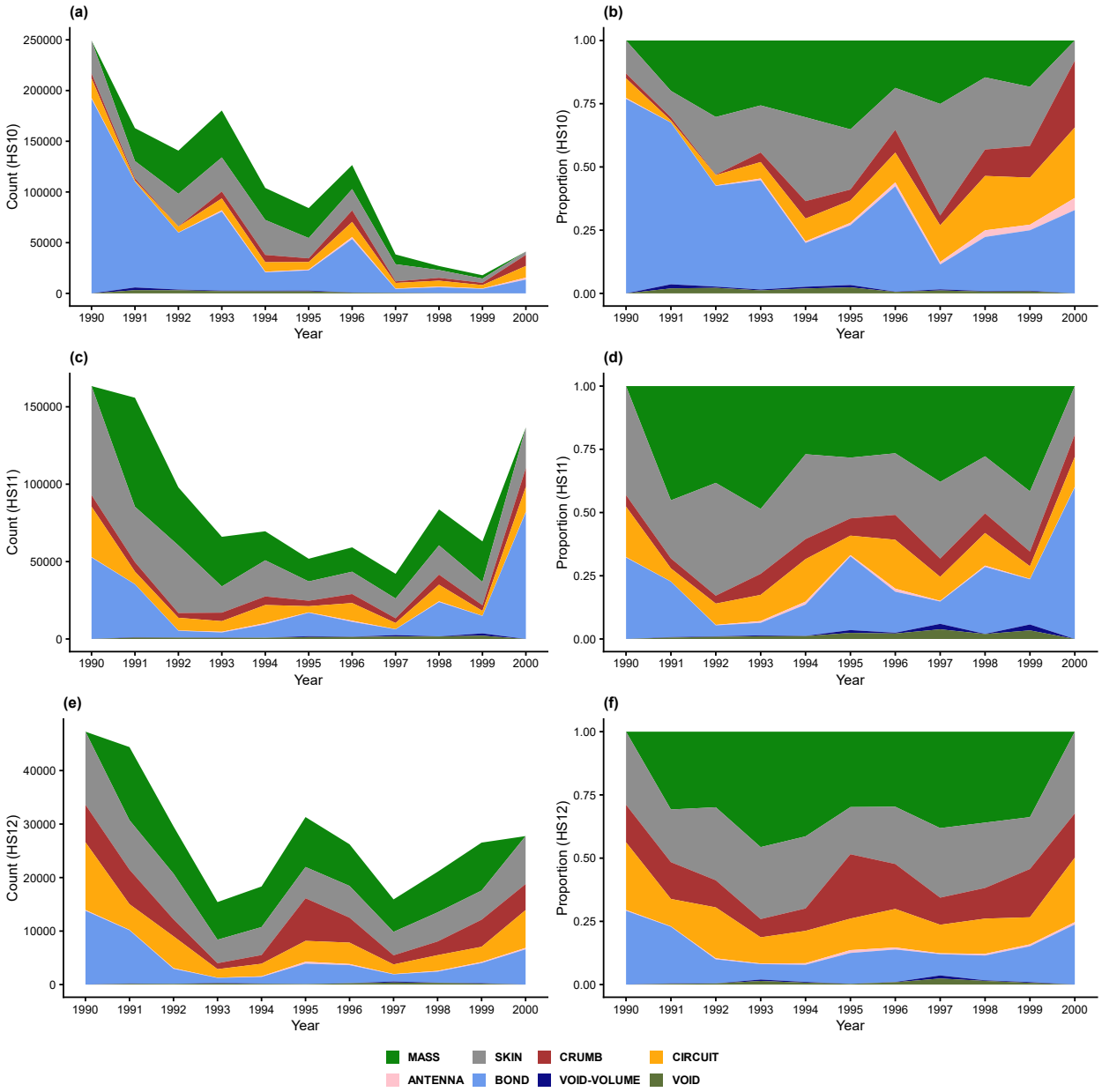


Figure 38. Temporal trajectories of morphological class composition for wildfire sites HS10–HS12 over the study period (1990–2000). Panels (a), (c), and (e) show counts, and panels (b), (d), and (f) show proportions for each site.

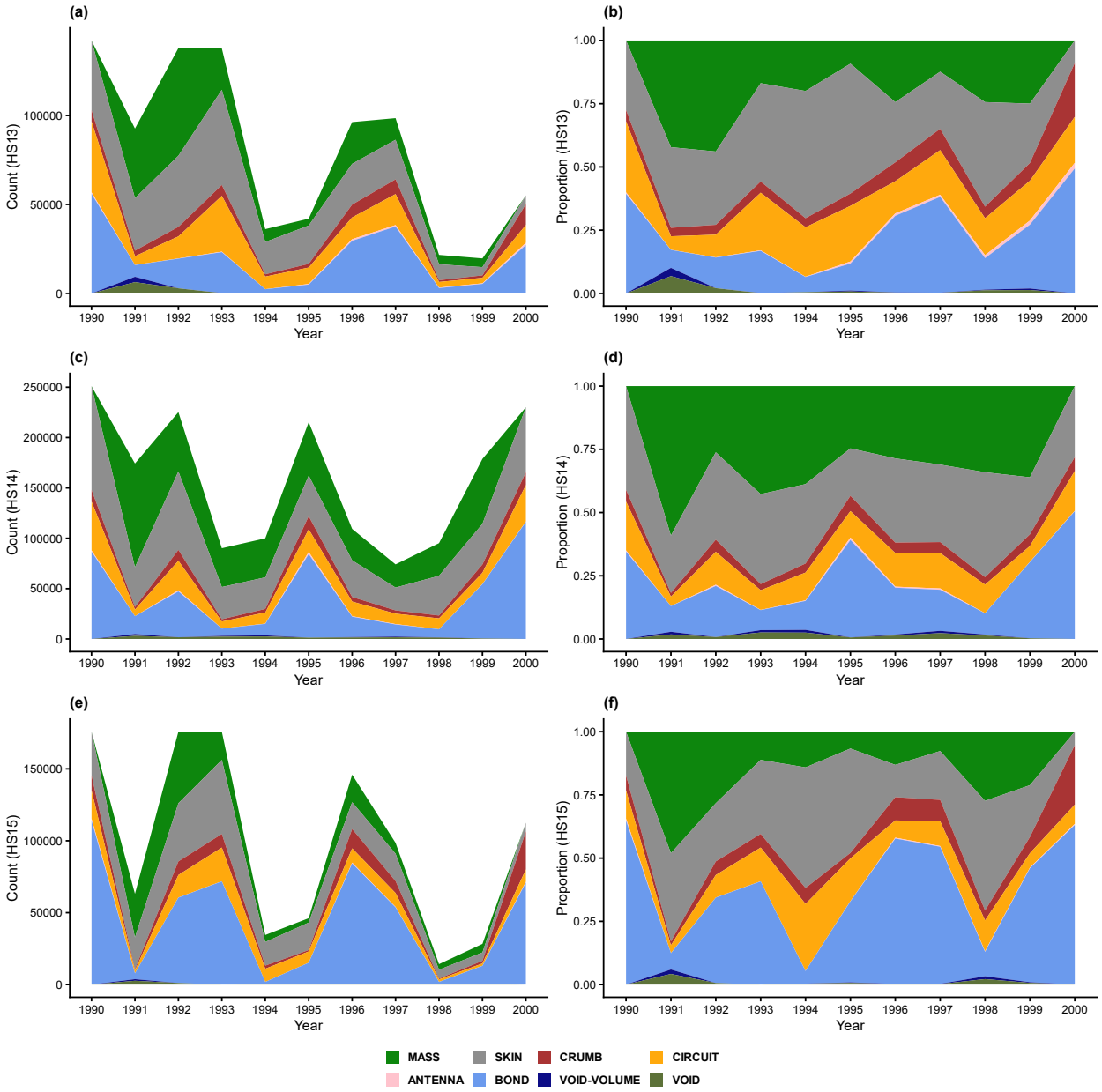


Figure 39. Temporal trajectories of morphological class composition for wildfire sites HS13–HS15 over the study period (1990–2000). Panels (a), (c), and (e) show counts, and panels (b), (d), and (f) show proportions for each site.

# 4 Discussion

## 4.1 Disturbance type effects on regeneration structures

The discussion focuses on how disturbance vectors and regional context influence three-dimensional landscape morphology and the implications of observed structural consistency and variability for understanding regeneration dynamics.

This study examined whether wildfire and harvesting produce different morphological structures, and whether these differences are consistent across eastern and western boreal ecoregions. The results indicate that although aggregated morphological proportions, as tested using the Chi-Square test of homogeneity of proportions, appear broadly similar across disturbance types, meaningful structural differences emerge when examined at the site-level and multivariate scales.

Univariate analyses revealed that wildfire-disturbed sites had significantly higher proportions of MASS structures, whereas harvested sites had significantly higher proportions of BOND structures. MASS structures represent internally cohesive, spatially continuous regeneration patterns, suggesting that wildfire disturbance promotes the consolidation of structural development during early regeneration. In contrast, the prominence of BOND structures in harvested sites indicates increased connectivity between fragmented components, a pattern consistent with landscapes shaped by anthropogenic disturbance. These findings align with established ecological theory distinguishing natural and managed disturbance regimes. Natural disturbances such as wildfire tend to remove vegetation more uniformly across space, allowing regeneration to proceed through relatively continuous successional pathways.

Harvesting, by contrast, introduces sharp spatial boundaries, retention patches, skid trails, and access corridors that disrupt spatial continuity and promote structurally heterogeneous outcomes (Franklin et al., 2002). The elevated presence of connectivity-related and void-associated morphological classes in harvested sites observed in this study is consistent with these mechanisms. Void-related classes (VOID and VOID-VOLUME) were also more prevalent in harvested landscapes, reflecting increased internal gaps and temporal discontinuities in vegetation recovery. Previous studies have shown that managed forest landscapes often exhibit higher fragmentation and internal edge density than naturally disturbed forests, even when total disturbed area is similar (Perera et al., 2008; Bouchard & Pothier, 2011; Dragotescu & Kneeshaw, 2012), and long-term landscape analyses indicate increasing edge density and

declining core forest cover across boreal ecozones influenced by disturbance patterns (Pickell et al., 2016). The present results extend these observations by demonstrating that such differences are detectable using three-dimensional morphological segmentation derived from time-series NDVI data, rather than traditional two-dimensional land-cover metrics.

Although contingency-based Chi-square tests of homogeneity of proportions suggested no statistically significant differences in the aggregated proportion of the morphological distributions between wildfire and harvesting, this apparent similarity masks important structural contrasts at the site level. Aggregation across sites can obscure variability and compensatory differences among morphological classes, particularly when changes are distributed across multiple elements rather than concentrated in a single class. The statistically significant MANOVA results confirm that wildfire and harvesting differ in their overall multivariate morphological configuration, indicating that disturbance effects are expressed through coordinated shifts across multiple structural components rather than through large changes in any single class.

Regional context further influenced morphological structure, with several classes exhibiting significant differences between eastern and western boreal ecoregions. Eastern sites tended to show a higher representation of fragmented and transitional structures, whereas western sites exhibited a higher proportion of cohesive and void-related classes. These patterns likely reflect underlying ecological gradients in climate, productivity, and disturbance history across the boreal zone (McGarigal et al., 2000).

However, the fact that regional differences were less pronounced in wildfire-disturbed sites than in harvested sites suggests that natural disturbance processes may impose a stronger structural signal that partially overrides regional variability. Larger and more contiguous fires in the western boreal region remain dominated by MASS, reflecting extensive cohesive disturbance footprints through time. In eastern regions, regeneration often proceeds through smaller and less contiguous disturbance patterns, causing MASS to decline and partition into other morphological classes such as SKIN, BOND, CRUMB, or CIRCUIT as recovery progresses. These differences in fire size, spatial continuity, and post-fire regeneration pathways may shape how morphology evolves across regions, while still producing an overall wildfire signal that is more consistent than the structurally prescribed patterns associated with harvesting.

Harvesting follows a more spatially prescribed and operationally constrained pattern, with cutblock geometry, retained patches, road networks, and management practices shaping disturbance structure at finer spatial scales. Because these managed patterns interact directly with local environmental conditions such as soils, moisture regimes, productivity, and species composition, regional ecological differences may remain more strongly expressed in harvested landscapes. As regeneration proceeds, these constraints can produce more variable transitions among morphological classes, with some sites retaining fragmented or connector-dominated structures for longer periods, while others consolidate more quickly into MASS. Consequently, harvested sites may display clearer east–west contrasts than wildfire-disturbed sites.

Overall, the results addressing the disturbance-type effects on regeneration structures indicate that wildfire and harvesting produce distinguishable morphological structures at the site level, even when aggregated distributions appear similar. Disturbance type influences not only the relative abundance of individual morphological classes, but also the multivariate configuration of post-disturbance structure. These findings highlight the importance of moving beyond aggregated composition metrics and incorporating spatially explicit, multivariate approaches when evaluating post-disturbance regeneration patterns in boreal forest systems.

### 4.2 Structural consistency and variability within disturbance types across regions

The structural consistency and variability within disturbance types and ecoregions were examined to determine whether post-disturbance morphological structures are consistent among sites affected by the same disturbance vector. Whereas disturbance-type effects on regeneration structures focused on differences in average structural composition between wildfire and harvesting, this question addressed within-group variability, asking whether a given disturbance process produces a characteristic and repeatable morphological structure across time and space. Assessing structural consistency is critical for understanding the effects of disturbance on all sites and evaluating whether disturbance vectors impose predictable constraints on boreal forest regeneration.

Multivariate dispersion analysis revealed a clear contrast in morphological consistency between disturbance vectors. Sites affected by wildfire exhibited lower distances to the group centroid than harvested sites, indicating reduced within-group variability and greater internal consistency in post-disturbance morphological structure. This result suggests that wildfire tends

to generate a relatively stable three-dimensional regeneration configuration across sites, despite differences in disturbance footprint size, local site conditions, or landscape context.

The greater consistency observed among wildfire-disturbed sites is consistent with ecological theory describing wildfire as a dominant natural disturbance that imposes strong, spatially extensive controls on forest structure. Stand-replacing fires often restructure broad areas within a single disturbance event, although the resulting burn pattern may remain spatially heterogeneous, effectively resetting structural conditions and initiating regeneration through comparable patterns of post-disturbance structural recovery through time (Kuuluvainen, 2009; Seidl & Turner, 2022).

As a result, post-fire regeneration begins immediately after burning, when removal of canopy cover increases the amount of sunlight reaching the forest floor, while combustion and ash deposition can increase short-term nutrient availability (Certini, 2005; Johnstone et al., 2016). These conditions favour rapid growth of grasses, herbs, and shrubs during the early years after disturbance, often producing a strong vegetation signal (Bond-Lamberty et al., 2002; Goetz et al., 2006). As recovery continues, tree seedlings and saplings increase in abundance and height, gradually overtopping the early ground and shrub layer (Johnstone et al., 2010). Over time, developing tree cover becomes the dominant structural component, producing more continuous and cohesive regeneration patterns (French et al., 2008). The present findings support this interpretation by showing that wildfire-driven regeneration exhibited not only distinct morphological composition, but also lower multivariate dispersion in three-dimensional structural form.

In contrast, harvested sites displayed substantially greater multivariate dispersion, indicating higher heterogeneity in morphological structure among sites affected by the same disturbance type. In other words, sites within the harvesting group differed more from one another in their overall morphological composition than wildfire-disturbed sites. This likely reflects differences in harvest design and management, including cutblock size and shape, retained patches, access roads, site preparation, and post-harvest treatments, as well as variation in local conditions such as soils, moisture availability, and pre-disturbance stand composition. Harvesting therefore produced a broader range of regeneration patterns through time rather than a single, consistent structural signature. Similar effects of forest management on structural heterogeneity and spatial pattern have been reported even where overall disturbance intensity is

comparable (Franklin et al., 2002; McGarigal & Marks, 1995). The elevated dispersion observed in harvested sites in this study reflects this diversity of management practices and highlights the complexity of anthropogenic disturbance effects on landscape morphology.

Visual patterns in the Principal Coordinates Analysis further support these conclusions. Wildfire-disturbed sites clustered more tightly around their centroid in multivariate space, whereas harvested sites were more broadly distributed. Although ordination techniques do not directly test dispersion, the observed clustering patterns are consistent with the PERMDISP results and provide an intuitive representation of structural consistency and variability. Together, these findings indicate that differences between disturbance vectors extend beyond shifts in mean morphological composition to include fundamental differences in the predictability and coherence of post-disturbance structural development.

Regional context also influenced morphological consistency, though its effect was secondary to that of disturbance type. Differences in dispersion between eastern and western boreal ecoregions were detectable but smaller than those observed between wildfire and harvesting. This suggests that while climatic gradients, species composition, and productivity influence regeneration trajectories, disturbance processes exert a stronger control over the degree of internal structural coherence. Similar conclusions have been reported in landscape-scale studies, where disturbance regimes often outweigh regional variability in shaping spatial structure and pattern (Riitters et al., 2007).

Importantly, the distinction between wildfire and harvesting in terms of morphological consistency has implications for forest management strategies that aim to emulate natural disturbance regimes. While harvesting may approximate certain compositional aspects of wildfire disturbance, the greater heterogeneity observed among harvested sites suggests that current management practices may not fully reproduce the structural regularity associated with natural fire-driven regeneration. This finding highlights the value of three-dimensional morphological analysis for evaluating the extent to which managed disturbances replicate natural structural outcomes, particularly during early stages of forest recovery.

Overall, the results on structural consistency and variability across disturbance types and ecoregions demonstrate that morphological structures are not equally consistent among disturbance vectors. Wildfire disturbance produces more internally coherent and repeatable regeneration patterns, whereas harvesting leads to greater variability in three-dimensional

structural configuration across sites. These findings complement the results of disturbance-type effects on regeneration structures by showing that disturbance type influences not only average morphological composition but also the stability and predictability of post-disturbance structural expression. Together, they underscore the importance of considering both composition and variability when assessing post-disturbance forest dynamics.

### 4.3 Values of the contribution of the temporal dimension

Treating time as the vertical axis in the three-dimensional voxel analysis provided a clearer interpretation of post-disturbance regeneration. Instead of analyzing each year as an independent map, annual layers were connected within a continuous space–time structure. This made it possible to examine how disturbed areas changed from year to year, including whether they retained internal continuity, became more fragmented, developed stronger edge structure, or remained connected through time. Regeneration could therefore be interpreted as a dynamic process rather than a single condition observed at a single time.

The stacked area charts illustrate this contribution by showing how morphological class composition changed across the study period. Changes in class proportions do not simply indicate vegetation cover. Instead, they describe changes in the spatial organization of disturbed areas during recovery. When MASS increases during the internal years of the disturbed area, MASS retains stronger core continuity across consecutive time layers. When MASS declines, those cohesive core areas contract or break apart as regeneration reduces the disturbed footprint. In contrast, increases in SKIN indicate that edge structure is becoming more prominent relative to the core area, while higher CRUMB indicates persistence of small, isolated, disturbed patches. Increases in BOND and CIRCUIT show that disturbed areas may no longer form one compact core, but remain connected through bridges or looped structures

A key contribution of the temporal approach is that it shows why morphological classes change through time. The first and final years of the study period represent a structural boundary. In the first year, MASS cannot occur because a fully enclosed three-dimensional core has not yet formed across neighbouring time layers. Similarly, MASS cannot occur in the final year because no subsequent annual layer exists to complete the temporal neighbourhood required for an interior core.

Within those internal years (1991-1999), the figures show how regeneration progressed through structural reorganization. Periods of higher MASS (1991-1994) indicate that the original disturbance pattern remained broad and spatially cohesive. Subsequent declines in MASS indicate that vegetation regeneration has reduced the extent of disturbed areas. Where BOND increased while MASS declined, formerly continuous disturbed structures were becoming partitioned but still retained connectivity between core areas. Where the CIRCUIT increased, disturbed areas formed more complex, connected configurations rather than a single dominant interior block. Rising SKIN relative to MASS indicates increasing edge influence, which is expected when disturbed patches become smaller or more subdivided through time.

Differences between disturbance types are clearer when viewed in this temporal context. Wildfire sites generally showed smoother shifts in class composition, with more coherent changes through time and lower variability among sites. This suggests that wildfire often creates broader disturbance footprints that then contract progressively during recovery. Harvested sites showed greater variation in the timing and magnitude of class changes, with stronger persistence of BOND, CIRCUIT, SKIN, and CRUMB in several years. This is consistent with managed landscapes, retained patches, access roads, site preparation, and post-harvest treatments, which together create a wider range of structural outcomes.

Regional contrasts were also more apparent through time. In the western boreal region, larger and more contiguous disturbance events were more frequently associated with MASS during disturbed years, indicating broader, more cohesive disturbed structures. In the eastern region, MASS often declined earlier and was more frequently accompanied by SKIN, BOND, CRUMB, or CIRCUIT, suggesting smaller or less continuous disturbance patterns and faster subdivision of disturbed areas during recovery.

These patterns are difficult to identify from static two-dimensional analyses alone. A single-year map may show increasing vegetation greenness, but it cannot reveal whether recovery is occurring through contraction of a large core area, fragmentation into smaller patches, or persistence of connected disturbed structures. Sites with similar annual spectral values may therefore represent very different structural histories.

Overall, representing time directly in the segmentation showed that regeneration was not a single end condition, but a continuous process of structural change. Differences between

disturbance types and ecoregions were expressed not only in overall composition but also in how disturbed landscapes regenerate over time.

### 4.4 Implications for boreal regeneration assessment

The combined findings from this research on how boreal forest recovers after disturbance by fire and harvesting, using 3D morphological segmentation, have important implications for assessing post-disturbance regeneration in boreal forest systems. Traditional two-dimensional metrics often emphasize area-based measures or class proportions, which may obscure meaningful differences in internal structure and variability. By incorporating three-dimensional morphological segmentation, this study demonstrates that regeneration outcomes differ not only in composition but also in spatial coherence and consistency.

The greater morphological consistency observed following wildfire suggests that natural disturbance processes may produce more predictable structural outcomes than anthropogenic disturbances. This has implications for forest management and monitoring, particularly in contexts where harvesting is intended to emulate natural disturbance regimes. The observed heterogeneity in harvested sites indicates that current practices may not fully replicate the structural characteristics of wildfire-driven regeneration, at least within the temporal window examined.

Furthermore, the presence of significant regional effects highlights the need to interpret disturbance outcomes within their ecological context. While the disturbance vector is a primary driver of morphological structure, regional conditions influence the expression and variability of regeneration patterns and should be considered in comparative assessments.

## 5 Conclusions

The objective of this study was to determine whether boreal forest stands disturbed by wildfire and forest harvesting regenerate differently when recovery is evaluated using a three-dimensional morphological framework that explicitly incorporates time. By stacking annual disturbance states into voxel cubes and segmenting them into structural classes, regeneration was examined as a connected spatial-temporal process rather than as a sequence of separate yearly maps. This provided an alternative to conventional two-dimensional assessments, which often describe vegetation recovery solely in terms of spectral change.

The results indicate that wildfire and harvesting do not produce identical regeneration structures after disturbance. Although some aggregated summaries suggested broad similarities, the overall analyses showed clear differences in structural organization. Wildfire sites were more strongly associated with MASS, reflecting larger, more cohesive areas that persisted over time. Harvested sites showed higher representation of BOND and related transitional classes, indicating greater subdivision, reconnection, and structural heterogeneity during recovery. These findings suggest that similar amounts of vegetation return do not necessarily represent the same regeneration pathway.

The findings also showed differences in consistency among sites. Wildfire locations generally followed more consistent structural trajectories, whereas harvested locations showed greater variability. This likely reflects the more standardized ecological processes that follow fire compared with the wider range of harvesting practices, site preparation methods, residual stand conditions, and local management histories that influence post-harvest recovery. Regeneration outcomes are therefore shaped not only by disturbance type, but also by how disturbance is expressed on the ground.

Regional contrasts were also evident. Western boreal sites more frequently retained cohesive structures, whereas eastern sites showed greater proportions of subdivided and transitional forms. These differences suggest that regeneration cannot be interpreted independently of the ecological setting. Climate, soils, species composition, moisture conditions, and disturbance history likely influence how post-disturbance structure develops through time. Disturbance type is important, but it operates within a broader regional context.

A further contribution of this thesis is methodological. The development of *morphpy* from the original R implementation created a scalable and reproducible workflow for analyzing

large voxel datasets. More broadly, this research demonstrates that time can be incorporated directly into morphological segmentation to evaluate forest recovery as a dynamic structural process involving persistence, fragmentation, reconnection, enclosure, and consolidation across successive years. This expands the analytical possibilities for remote sensing studies of disturbance and recovery.

Several limitations should be acknowledged. The study examined an eleven-year recovery period and relied on NDVI-based binary classifications of disturbed and non-disturbed conditions. While appropriate for detecting broad patterns of disturbance persistence and recovery, this simplification does not capture all dimensions of post-disturbance change or the full range of ecological conditions present on the landscape. Future research could extend the monitoring period, incorporate additional spectral indicators, and test the method across other forest regions and disturbance contexts.

In conclusion, this study showed that disturbance type and ecoregional setting both influence post-disturbance regeneration in Ontario's boreal forest. Wildfire and harvesting may each initiate recovery, but they do so through different structural pathways that remain detectable when regeneration is examined through a three-dimensional morphological lens. The thesis, therefore, contributes both a new analytical approach and new ecological evidence for evaluating whether managed disturbance replicates the structural outcomes of natural disturbance.

## 6 References


Acil, N., Sadler, J. P., Senf, C., Suvanto, S., & Pugh, T. A. M. (2024). Landscape patterns in stand-replacing disturbances across the world's forests. *Nature Sustainability*, *8*(1), 86–98. https://doi.org/10.1038/s41893-024-01450-3

Ahmed, O. S., Wulder, M. A., White, J. C., Hermosilla, T., Coops, N. C., & Franklin, S. E. (2017). Classification of annual non-stand replacing boreal forest change in Canada using Landsat time series: A case study in northern Ontario. *Remote Sensing Letters*, *8*(1), 29–37. https://doi.org/10.1080/2150704X.2016.1233371

Araya, Y. H., Remmel, T. K., & Perera, A. H. (2015). Residual vegetation patches within natural boreal wild fires: characterizing by pattern metrics, land cover expectations and proximity to firebreak features. *Geomatica (Ottawa)*, *69*(4), 395-. https://doi.org/10.5623/cig2015-402

Arseneault, D. (2001). Impact of fire behavior on postfire forest development in a homogeneous boreal landscape. *Canadian Journal of Forest Research*, *31*(8), 1367–1374. https://doi.org/10.1139/x01-065

Baltsavias, E. P. (1999). Airborne laser scanning: Basic relations and formulas. *ISPRS Journal of Photogrammetry and Remote Sensing*, *54*(2–3), 199–214. https://doi.org/10.1016/S0924-2716(99)00015-5

Banin, L. F., Raine, E. H., Rowland, L. M., Chazdon, R. L., Smith, S. W., Rahman, N. E. B., Butler, A., Philipson, C., Applegate, G. G., Axelsson, E. P., Budiharta, S., Chua, S. C., Cutler, M. E. J., Elliott, S., Gemita, E., Godoong, E., Graham, L. L. B., Hayward, R. M., Hector, A., … Burslem, D. F. R. P. (2023). The road to recovery: A synthesis of outcomes from ecosystem restoration in tropical and sub-tropical Asian forests. *Philosophical Transactions of the Royal Society B: Biological Sciences*, *378*(1867), 20210090. https://doi.org/10.1098/rstb.2021.0090

Banskota, A., Kayastha, N., Falkowski, M. J., Wulder, M. A., Froese, R. E., & White, J. C. (2014). Forest Monitoring Using Landsat Time Series Data: A Review. *Canadian Journal of Remote Sensing*, *40*(5), 362–384. https://doi.org/10.1080/07038992.2014.987376

Bartels, S. F., Chen, H. Y. H., Wulder, M. A., & White, J. C. (2016). Trends in post-disturbance recovery rates of Canada's forests following wildfire and harvest. *Forest Ecology and Management*, *361*, 194–207. https://doi.org/10.1016/j.foreco.2015.11.015

Bergeron, J. A. C., Pinzon, J., Odsen, S., Bartels, S., Macdonald, S. E., & Spence, J. R. (2017). Ecosystem memory of wildfires affects resilience of boreal mixedwood biodiversity after retention harvest. *Oikos*, *126*(12), 1738–1747. https://doi.org/10.1111/oik.04208

Bergeron, K. S.-H. P., Richard T. Corlett, Yves (Ed.). (2015). *Routledge Handbook of Forest Ecology*. Routledge. https://doi.org/10.4324/9781315818290

Bergeron, Y., Flannigan, M., Gauthier, S., Leduc, A., & Lefort, P. (2004). Past, Current and Future Fire Frequency in the Canadian Boreal Forest: Implications for Sustainable Forest Management. *AMBIO: A Journal of the Human Environment*, *33*(6), 356–360. https://doi.org/10.1579/0044-7447-33.6.356

Bergeron, Y., Harvey, B., Leduc, A., & Gauthier, S. (1999). Forest management guidelines based on natural disturbance dynamics: Stand- and forest-level considerations. *The Forestry Chronicle*, *75*(1), 49–54. https://doi.org/10.5558/tfc75049-1

Best, I. N., Brown, L., Elkin, C., Finnegan, L., McClelland, C. J. R., & Johnson, C. J. (2024). Cut vs. fire: A comparative study of the temporal effects of timber harvest and wildfire on

ecological indicators of the boreal forest. *Landscape Ecology*, *39*(4), 81. https://doi.org/10.1007/s10980-024-01882-4

Birch, M., Zwiep, S., Coops, N. C., Dean, A., Kavlin, M., & Seifert, F. M. (2025, January 20). *Monitoring forest disturbance recovery using metrics derived from multi-spectral satellite time-series: Introducing the spectral recovery open-source package with European and Canadian use cases*. https://doi.org/10.5194/egusphere-egu24-13697

Blanco, J. A., Welham, C., Kimmins, J. P. (Hamish), Seely, B., & Mailly, D. (2009). Guidelines for modeling natural regeneration in boreal forests. *The Forestry Chronicle*, *85*(3), 427–439. https://doi.org/10.5558/tfc85427-3

Bonannella, C., Chirici, G., Travaglini, D., Pecchi, M., Vangi, E., D'Amico, G., & Giannetti, F. (2022). Characterization of Wildfires and Harvesting Forest Disturbances and Recovery Using Landsat Time Series: A Case Study in Mediterranean Forests in Central Italy. *Fire*, *5*(3), 68. https://doi.org/10.3390/fire5030068

Bond-Lamberty, B., Wang, C., & Gower, S. T. (2002). Aboveground and belowground biomass and sapwood area allometric equations for six boreal tree species of northern Manitoba. *Canadian Journal of Forest Research*, *32*(8), 1441–1450. https://doi.org/10.1139/x02-063

Bouchard, M., & Pothier, D. (2011). Long-term influence of fire and harvesting on boreal forest age structure and forest composition in eastern Québec. *Forest Ecology and Management*, *261*(4), 811–820. https://doi.org/10.1016/j.foreco.2010.11.020

Bradshaw, C. J. A., & Warkentin, I. G. (2015). Global estimates of boreal forest carbon stocks and flux. *Global and Planetary Change*, *128*, 24–30. https://doi.org/10.1016/j.gloplacha.2015.02.004

Brandt, J. P., Flannigan, M. D., Maynard, D. G., Thompson, I. D., & Volney, W. J. A. (2013). An introduction to Canada's boreal zone: Ecosystem processes, health, sustainability, and environmental issues INTRODUCTION. *ENVIRONMENTAL REVIEWS*, *21*(4), 207–226. https://doi.org/10.1139/er-2013-0040

Brassard, B. W., & Chen, H. Y. H. (2006). Stand Structural Dynamics of North American Boreal Forests. *Critical Reviews in Plant Sciences*, *25*(2), 115–137. https://doi.org/10.1080/07352680500348857

Bray, J. R., & Curtis, J. T. (1957). An Ordination of the Upland Forest Communities of Southern Wisconsin. *Ecological Monographs*, *27*(4), 325–349. https://doi.org/10.2307/1942268

Burton, P. J., Messier, C., Adamowicz, W. L., & Kuuluvainen, T. (2006). Sustainable management of Canada's boreal forests: Progress and prospects. *Écoscience*, *13*(2), 234–248. https://doi.org/10.2980/i1195-6860-13-2-234.1

Celebrezze, J. V., Franz, M. C., Andrus, R. A., Stahl, A. T., Steen-Adams, M., & Meddens, A. J. H. (2024). A fast spectral recovery does not necessarily indicate post-fire forest recovery. *Fire Ecology*, *20*(1), 54. https://doi.org/10.1186/s42408-024-00288-6

Certini, G. (2005). Effects of fire on properties of forest soils: A review. *Oecologia*, *143*(1), 1–10. https://doi.org/10.1007/s00442-004-1788-8

Cohen, W. B., & Goward, S. N. (2004). Landsat's Role in Ecological Applications of Remote Sensing. *BioScience*, *54*(6), 535. https://doi.org/10.1641/0006-3568(2004)054%255B0535:LRIEAO%255D2.0.CO;2

Csardi, G., & Nepusz, T. (2005). *The igraph software package for complex network research*.

Dandois, J. P., & Ellis, E. C. (2013). High spatial resolution three-dimensional mapping of vegetation spectral dynamics using computer vision. *Remote Sensing of Environment*, *136*, 259–276. https://doi.org/10.1016/j.rse.2013.04.005

De Groot, W. J., Flannigan, M. D., & Cantin, A. S. (2013). Climate change impacts on future boreal fire regimes. *Forest Ecology and Management*, *294*, 35–44. https://doi.org/10.1016/j.foreco.2012.09.027

Donato, D. C., Campbell, J. L., & Franklin, J. F. (2012). Multiple successional pathways and precocity in forest development: Can some forests be born complex? *Journal of Vegetation Science*, *23*(3), 576–584. https://doi.org/10.1111/j.1654-1103.2011.01362.x

Dragotescu, I., & Kneeshaw, D. (2012). A comparison of residual forest following fires and harvesting in boreal forests in Quebec, Canada. *Silva Fennica*, *46*(3). https://doi.org/10.14214/sf.47

Forest, B. (1993). *Fire and Vegetation Dynamics: Studies from the North American*.

Forest Canada. (1994). Forest Management in Ontario. *Forest Management in Ontario*. https://forestscanada.ca/en/page/forest-management-in-ontario

Franklin, J. F., Spies, T. A., Pelt, R. V., Carey, A. B., Thornburgh, D. A., Berg, D. R., Lindenmayer, D. B., Harmon, M. E., Keeton, W. S., Shaw, D. C., Bible, K., & Chen, J. (2002). Disturbances and structural development of natural forest ecosystems with silvicultural implications, using Douglas-fir forests as an example. *Forest Ecology and Management*, *155*(1–3), 399–423. https://doi.org/10.1016/S0378-1127(01)00575-8

Frelich, L. (2016). Forest dynamics. *F1000Research*, *5*, 183. https://doi.org/10.12688/f1000research.7412.1

French, N. H. F., Kasischke, E. S., Hall, R. J., Murphy, K. A., Verbyla, D. L., Hoy, E. E., & Allen, J. L. (2008). Using Landsat data to assess fire and burn severity in the North American boreal forest region: An overview and summary of results. *International Journal of Wildfire*, *17*(4), 443. https://doi.org/10.1071/WF08007

García, M., North, P., Viana-Soto, A., Stavros, N. E., Rosette, J., Martín, M. P., Franquesa, M., González-Cascón, R., Riaño, D., Becerra, J., & Zhao, K. (2020). Evaluating the potential of LiDAR data for fire damage assessment: A radiative transfer model approach. *Remote Sensing of Environment*, *247*, 111893. https://doi.org/10.1016/j.rse.2020.111893

Gauthier, S., Bernier, P., Kuuluvainen, T., Shvidenko, A. Z., & Schepaschenko, D. G. (2015). Boreal forest health and global change. *Science*, *349*(6250), 819–822. https://doi.org/10.1126/science.aaa9092

Girona, M. M., Morin, H., Gauthier, S., & Bergeron, Y. (Eds.). (2023). *Boreal forests in the face of climate change: Sustainable management*. Springer.

Goetz, S. J., Fiske, G. J., & Bunn, A. G. (2006). Using satellite time-series data sets to analyze fire disturbance and forest recovery across Canada. *Remote Sensing of Environment*, *101*(3), 352–365. https://doi.org/10.1016/j.rse.2006.01.011

Golden, D. M., Audet, C., & Smith, M. A. (Peggy). (2015). "Blue-ice": Framing climate change and reframing climate change adaptation from the indigenous peoples' perspective in the northern boreal forest of Ontario, Canada. *Climate and Development*, *7*(5), 401–413. https://doi.org/10.1080/17565529.2014.966048

Gower, J. C. (1966). Some Distance Properties of Latent Root and Vector Methods Used in Multivariate Analysis. *Biometrika*, *53*(3/4), 325. https://doi.org/10.2307/2333639

Greene, D. F., Zasada, J. C., Sirois, L., Kneeshaw, D., Morin, H., Charron, I., & Simard, M. J. (1999). A review of the regeneration dynamics of north american boreal forest tree species. *Canadian Journal of Forest Research-Revue Canadienne De Recherche Forestiere*, *29*(6), 824–839.

Groot, A., Man, R., & Wood, J. (2009). Spatial and temporal patterns of Populus tremuloides regeneration in small forest openings in northern Ontario. *The Forestry Chronicle*, *85*(4), 548–557. https://doi.org/10.5558/tfc85548-4

Halofsky, J. E., Peterson, D. L., & Harvey, B. J. (2020). Changing wildfire, changing forests: The effects of climate change on fire regimes and vegetation in the Pacific Northwest, USA. *Fire Ecology*, *16*(1), 4. https://doi.org/10.1186/s42408-019-0062-8

Hargis, C. D., Bissonette, J. A., & David, J. L. (1998). The behavior of landscape metrics commonly used in the study of habitat fragmentation. *Landscape Ecology*, (13), 167–186.

Harper, K. A., Lesieur, D., Bergeron, Y., & Drapeau, P. (2004). Forest structure and composition at young fire and cut edges in black spruce boreal forest. *Canadian Journal of Forest Research*, *34*(2), 289–302. https://doi.org/10.1139/x03-279

Harris, C. R., Millman, K. J., Van Der Walt, S. J., Gommers, R., Virtanen, P., Cournapeau, D., Wieser, E., Taylor, J., Berg, S., Smith, N. J., Kern, R., Picus, M., Hoyer, S., Van Kerkwijk, M. H., Brett, M., Haldane, A., Del Río, J. F., Wiebe, M., Peterson, P., … Oliphant, T. E. (2020). Array programming with NumPy. *Nature*, *585*(7825), 357–362. https://doi.org/10.1038/s41586-020-2649-2

Hayes, D. J., Butman, D. E., Domke, G. M., Fisher, J. B., Neigh, C. S. R., & Welp, L. R. (2022). Boreal forests. In *Balancing Greenhouse Gas Budgets* (pp. 203–236). Elsevier. https://doi.org/10.1016/B978-0-12-814952-2.00025-3

He, L., Hong, L., & Zhu, A.-X. (2024). An Improved LandTrendr Algorithm for Forest Disturbance Detection Using Optimized Temporal Trajectories of the Spectrum: A Case Study in Yunnan Province, China. *Forests*, *15*(9), 1539. https://doi.org/10.3390/f15091539

Hermosilla, T., Wulder, M. A., White, J. C., Coops, N. C., & Hobart, G. W. (2015). An integrated Landsat time series protocol for change detection and generation of annual gap-free surface reflectance composites. *Remote Sensing of Environment*, *158*, 220–234. https://doi.org/10.1016/j.rse.2014.11.005

Hermosilla, T., Wulder, M. A., White, J. C., Coops, N. C., Hobart, G. W., & Campbell, L. B. (2016). Mass data processing of time series Landsat imagery: Pixels to data products for forest monitoring. *International Journal of Digital Earth*, *9*(11), 1035–1054. https://doi.org/10.1080/17538947.2016.1187673

Hunter, J. D. (2007). Matplotlib: A 2D Graphics Environment. *Computing in Science & Engineering*, *9*(3), 90–95. https://doi.org/10.1109/MCSE.2007.55

Jayen, K., Leduc, A., & Bergeron, Y. (2006). Effect of fire severity on regeneration success in the boreal forest of northwest quebec, canada. *Ecoscience*, *13*(2), 143–151.

Johnstone, J. F., Allen, C. D., Franklin, J. F., Frelich, L. E., Harvey, B. J., Higuera, P. E., Mack, M. C., Meentemeyer, R. K., Metz, M. R., Perry, G. L., Schoennagel, T., & Turner, M. G. (2016). Changing disturbance regimes, ecological memory, and forest resilience. *Frontiers in Ecology and the Environment*, *14*(7), 369–378. https://doi.org/10.1002/fee.1311

Johnstone, J. F., Chapin, F. S., Hollingsworth, T. N., Mack, M. C., Romanovsky, V., & Turetsky, M. (2010). Fire, climate change, and forest resilience in interior AlaskaThis article is one of a selection of papers from The Dynamics of Change in Alaska's Boreal Forests: Resilience and Vulnerability in Response to Climate Warming. *Canadian Journal of Forest Research*, *40*(7), 1302–1312. https://doi.org/10.1139/X10-061

Jorgenson, J.-P. S., Ken Baldwin, Pavel Krestov, Torre. (2015). Boreal Forests. In *Routledge Handbook of Forest Ecology*. Routledge.

Kennedy, R. E., Yang, Z., & Cohen, W. B. (2010). Detecting trends in forest disturbance and recovery using yearly Landsat time series: 1. LandTrendr — Temporal segmentation algorithms. *Remote Sensing of Environment*, *114*(12), 2897–2910. https://doi.org/10.1016/j.rse.2010.07.008

Kullback, S., & Leibler, R. A. (1951). On Information and Sufficiency. *The Annals of Mathematical Statistics*, *22*(1), 79–86. https://doi.org/10.1214/aoms/1177729694

Kurz, W. A., Shaw, C. H., Boisvenue, C., Stinson, G., Metsaranta, J., Leckie, D., Dyk, A., Smyth, C., & Neilson, E. T. (2013). Carbon in Canada's boreal forest—A synthesis. *Environmental Reviews*, *21*(4), 260–292. https://doi.org/10.1139/er-2013-0041

Kuuluvainen, T. (2009). Forest Management and Biodiversity Conservation Based on Natural Ecosystem Dynamics in Northern Europe: The Complexity Challenge. *AMBIO: A Journal of the Human Environment*, *38*(6), 309–315. https://doi.org/10.1579/08-A-490.1

Kuuluvainen, T., Angelstam, P., Frelich, L., Jõgiste, K., Koivula, M., Kubota, Y., Lafleur, B., & Macdonald, E. (2021). Natural Disturbance-Based Forest Management: Moving Beyond Retention and Continuous-Cover Forestry. *Frontiers in Forests and Global Change*, *4*, 629020. https://doi.org/10.3389/ffgc.2021.629020

Kuuluvainen, T., & Gauthier, S. (2018). Young and old forest in the boreal: Critical stages of ecosystem dynamics and management under global change. *Forest Ecosystems*, *5*(1), 26. https://doi.org/10.1186/s40663-018-0142-2

Lafortezza, R., Corry, R. C., Sanesi, G., & Brown, R. D. (2005). Quantitative approaches to landscape spatial planning: Clues from landscape ecology. *WIT Transactions on Ecology and the Environment*, *84*.

Lausch, A., Blaschke, T., Haase, D., Herzog, F., Syrbe, R.-U., Tischendorf, L., & Walz, U. (2015). Understanding and quantifying landscape structure – A review on relevant process characteristics, data models and landscape metrics. *Ecological Modelling*, *295*, 31–41. https://doi.org/10.1016/j.ecolmodel.2014.08.018

Legendre, P., Legendre, L., Legendre, L., & Legendre, L. (1998). *Numerical ecology* (2nd English ed). Elsevier.

Lemprière, T. C., Kurz, W. A., Hogg, E. H., Schmoll, C., Rampley, G. J., Yemshanov, D., McKenney, D. W., Gilsenan, R., Beatch, A., Blain, D., Bhatti, J. S., & Krcmar, E. (2013). Canadian boreal forests and climate change mitigation. *Environmental Reviews*, *21*(4), 293–321. https://doi.org/10.1139/er-2013-0039

Lesmeister, D. B., Davis, R. J., & Rockweit, J. T. (2025). Resolving conservation conflict through fire refugia: Integrating landscape resilience into forest management. *Journal of Environmental Management*, *393*, 126974. https://doi.org/10.1016/j.jenvman.2025.126974

Liu, B., Liang, Y., He, H. S., Liu, Z., Ma, T., & Wu, M. M. (2022). Wildfire affects boreal forest resilience through post-fire recruitment in Northeastern China. *Ecological Indicators*, *145*, 109705. https://doi.org/10.1016/j.ecolind.2022.109705

Mackey, B., Campbell, C., Norman, P., Hugh, S., DellaSala, D. A., Malcolm, J. R., Desrochers, M., & Drapeau, P. (2023). Assessing the Cumulative Impacts of Forest Management on Forest Age Structure Development and Woodland Caribou Habitat in Boreal Landscapes: A Case Study from Two Canadian Provinces. *Land*, *13*(1), 6. https://doi.org/10.3390/land13010006

McGarigal, K., & Marks, B. J. (1995). *FRAGSTATS: Spatial pattern analysis program for quantifying landscape structure.* (PNW-GTR-351; p. PNW-GTR-351). U.S. Department of Agriculture, Forest Service, Pacific Northwest Research Station. https://doi.org/10.2737/PNW-GTR-351

McGarigal, K., Stafford, S., & Cushman, S. (2000). *Multivariate Statistics for Wildlife and Ecology Research*. Springer New York. https://doi.org/10.1007/978-1-4612-1288-1

McKinney, W. (2010). *Data Structures for Statistical Computing in Python*. 56–61. https://doi.org/10.25080/Majora-92bf1922-00a

McRae, D. J., Duchesne, L. C., Freedman, B., Lynham, T. J., & Woodley, S. (2001). Comparisons between wildfire and forest harvesting and their implications in forest management. *Environmental Reviews*, *9*(4), 223–260. https://doi.org/10.1139/a01-010

Ministry of Natural Resources. (2013). *Emulating natural disturbances: Clearcut silviculture in Ontario*.

Nguyen-Xuan, T., Bergeron, Y., Simard, D., Fyles, J. W., & Paré, D. (2000). The importance of forest floor disturbance in the early regeneration patterns of the boreal forest of western and central Quebec: A wildfire versus logging comparison. *Canadian Journal of Forest Research*, *30*(9), 1353–1364. https://doi.org/10.1139/x00-067

Nowosad, J., & Stepinski, T. F. (2019). Information theory as a consistent framework for quantification and classification of landscape patterns. *Landscape Ecology*, *34*(9), 2091–2101. https://doi.org/10.1007/s10980-019-00830-x

O'Farrell, P. J., & Anderson, P. M. (2010). Sustainable multifunctional landscapes: A review to implementation. *Current Opinion in Environmental Sustainability*, *2*(1–2), 59–65. https://doi.org/10.1016/j.cosust.2010.02.005

OMNR. (2001). Forest Management Guide for Natural Disturbance Pattern Emulation. *Forest Management Guide for Natural Disturbance Pattern Emulation, Version 3.1. Ont. Min. Nat. Res., Queen's Printer for Ontario, Toronto. 40 p.*

Ontario Ministry of Northern Development, Mines, Natural Resources and Forestry. (2021). *State of Ontario's Natural Resources Forests 2021*.

Ouellette, M., Remmel, T. K., & Perera, A. H. (2020). *A spatial database of historical wildfire and timber harvest in the boreal Area of the Undertaking of Ontario: The methodological framework* (Science and Research Technical Report TR-37; p. 31 + appendix). Ontario Ministry of Natural Resources and Forestry, Science and Research Branch. http://www.borealdb.ca

Pascual, C., García-Abril, A., Cohen, W. B., & Martín-Fernández, S. (2010). Relationship between LiDAR-derived forest canopy height and Landsat images. *International Journal of Remote Sensing*, *31*(5), 1261–1280. https://doi.org/10.1080/01431160903380656

Pasquarella, V. J., Arévalo, P., Bratley, K. H., Bullock, E. L., Gorelick, N., Yang, Z., & Kennedy, R. E. (2022). Demystifying LandTrendr and CCDC temporal segmentation. *International Journal of Applied Earth Observation and Geoinformation*, *110*, 102806. https://doi.org/10.1016/j.jag.2022.102806

Perera, A., Buse, L., & Weber, M. (Eds.). (2008). *Emulating Natural Forest Landscape Disturbances: Concepts and Applications*. Columbia University Press. https://doi.org/10.7312/pere12916

Perera, A. H., & Cui, W. (2010). Emulating natural disturbances as a forest management goal: Lessons from fire regime simulations. *Forest Ecology and Management*, *259*(7), 1328–1337. https://doi.org/10.1016/j.foreco.2009.03.018

Pickell, P. D., Andison, D. W., & Coops, N. C. (2013). Characterizations of anthropogenic disturbance patterns in the mixedwood boreal forest of Alberta, Canada. *Forest Ecology and Management*, *304*, 243–253. https://doi.org/10.1016/j.foreco.2013.04.031

Pickell, P. D., Coops, N. C., Gergel, S. E., Andison, D. W., & Marshall, P. L. (2016). Evolution of Canada's Boreal Forest Spatial Patterns as Seen from Space. *PLOS ONE*, *11*(7), e0157736. https://doi.org/10.1371/journal.pone.0157736

Plotly Technologies Inc. (2015). *Collaborative data science Publisher: Plotly Technologies Inc* [Computer software]. https://plot.ly

Remmel, T. K. (2020). Distributions of Hyper-Local Configuration Elements to Characterize, Compare, and Assess Landscape-Level Spatial Patterns. *Entropy*, *22*(4), 420. https://doi.org/10.3390/e22040420

Remmel, T. K. (2022). Extending morphological pattern segmentation to 3D voxels. *Landscape Ecology*. https://doi.org/10.1007/s10980-021-01384-7

Remmel, T. K., & Csillag, F. (2003). When are two landscape pattern indices significantly different? *Journal of Geographical Systems*, *5*(4), 331–351. https://doi.org/10.1007/s10109-003-0116-x

Remmel, T. K., Ouellette, M., & Wu, W. J. (2023). A boreal wildfire and harvesting database with ensemble confidence attributes for Ontario (1972-2021+). *INTERNATIONAL JOURNAL OF APPLIED EARTH OBSERVATION AND GEOINFORMATION*, *117*, 103199. https://doi.org/10.1016/j.jag.2023.103199

Riitters, K. H., O'Neill, R. V., Hunsaker, C. T., Wickham, J. D., Yankee, D. H., Timmins, S. P., Jones, K. B., & Jackson, B. L. (1995). A factor analysis of landscape pattern and structure metrics. *Landscape Ecology*, *10*(1), 23–39. https://doi.org/10.1007/BF00158551

Riitters, K. H., Vogt, P., Soille, P., Kozak, J., & Estreguil, C. (2007). Neutral model analysis of landscape patterns from mathematical morphology. *Landscape Ecology*, *22*(7), 1033–1043. https://doi.org/10.1007/s10980-007-9089-3

Riitters, K., Vogt, P., Soille, P., & Estreguil, C. (2009). Landscape patterns from mathematical morphology on maps with contagion. *Landscape Ecology*, *24*, 699–709.

Robbins, P. (2007). *Encyclopedia of Environment and Society*. SAGE Publications, Inc. https://doi.org/10.4135/9781412953924

Rouse, C. (1986). *Fire effects in northeastern forests: Jack pine.* (NC-GTR-106; p. NC-GTR-106). U.S. Department of Agriculture, Forest Service, North Central Forest Experiment Station. https://doi.org/10.2737/NC-GTR-106

Rouse, J, W., Jr., Haas, R. H., Schell, J. A., & Deering, D. W. (1974). Monitoring Vegetation Systems in the Great Plains with Erts. *Third Earth Resources Technology Satellite-1 Symposium- Volume I: Technical Presentations. NASA SP-351, Compiled and Edited by Stanley C. Freden, Enrico P. Mercanti, and Margaret A. Becker, 1994 Pages,* p.309.

Salgado, L., Alvarez, M. G., Díaz, A. M., Gallego, J. R., & Forján, R. (2024). Impact of wildfire recurrence on soil properties and organic carbon fractions. *Journal of Environmental Management*, *354*, 120293. https://doi.org/10.1016/j.jenvman.2024.120293

Schindler, S., Poirazidis, K., & Wrbka, T. (2008). Towards a core set of landscape metrics for biodiversity assessments: A case study from Dadia National Park, Greece. *Ecological Indicators*, *8*(5), 502–514. https://doi.org/10.1016/j.ecolind.2007.06.001

Schroeder, T. A., Wulder, M. A., Healey, S. P., & Moisen, G. G. (2011). Mapping wildfire and clearcut harvest disturbances in boreal forests with Landsat time series data. *Remote Sensing of Environment*, *115*(6), 1421–1433. https://doi.org/10.1016/j.rse.2011.01.022

Seidl, R., Honkaniemi, J., Aakala, T., Aleinikov, A., Angelstam, P., Bouchard, M., Boulanger, Y., Burton, P. J., De Grandpré, L., Gauthier, S., Hansen, W. D., Jepsen, J. U., Jõgiste, K., Kneeshaw, D. D., Kuuluvainen, T., Lisitsyna, O., Makoto, K., Mori, A. S., Pureswaran, D. S., … Senf, C. (2020). Globally consistent climate sensitivity of natural disturbances across boreal and temperate forest ecosystems. *Ecography*, *43*(7), 967–978. https://doi.org/10.1111/ecog.04995

Seidl, R., Rammer, W., & Spies, T. A. (2014). Disturbance legacies increase the resilience of forest ecosystem structure, composition, and functioning. *Ecological Applications*, *24*(8), 2063–2077. https://doi.org/10.1890/14-0255.1

Seidl, R., Thom, D., Kautz, M., Martin-Benito, D., Peltoniemi, M., Vacchiano, G., Wild, J., Ascoli, D., Petr, M., Honkaniemi, J., Lexer, M. J., Trotsiuk, V., Mairota, P., Svoboda, M., Fabrika, M., Nagel, T. A., & Reyer, C. P. O. (2017). Forest disturbances under climate change. *Nature Climate Change*, *7*(6), 395–402. https://doi.org/10.1038/nclimate3303

Seidl, R., & Turner, M. G. (2022). Post-disturbance reorganization of forest ecosystems in a changing world. *Proceedings of the National Academy of Sciences - PNAS*, *119*(28), 1-e2202190119. https://doi.org/10.1073/pnas.2202190119

Sharpe, M., Hwang, H., Schroeder, D., Ryu, S. R., & Lieffers, V. J. (2017). Prescribed fire as a tool to regenerate live and dead serotinous jack pine (Pinus banksiana) stands. *International Journal of Wildfire*, *26*(6), 478–484. https://doi.org/10.1071/WF17046

Soille, P. (2004). Segmentation. In P. Soille, *Morphological Image Analysis* (pp. 267–292). Springer Berlin Heidelberg. https://doi.org/10.1007/978-3-662-05088-0_9

Soille, P., & Vogt, P. (2009). Morphological segmentation of binary patterns. *Pattern Recognition Letters*, *30*(4), 456–459. https://doi.org/10.1016/j.patrec.2008.10.015

Soille, P., & Vogt, P. (2022). Morphological spatial pattern analysis: open source release. *The International Archives of the Photogrammetry, Remote Sensing and Spatial Information Sciences*, *XLVIII-4/W1-2022*, 427–433. https://doi.org/10.5194/isprs-archives-XLVIII-4-W1-2022-427-2022

Thompson, I. D., Perera, A., & Euler, D. (2000). *Ecology of a managed terrestrial landscape: Patterns and processes of forest landscapes in Ontario*. Published by UBC Press in cooperation with the Ontario Ministry of Natural Resources.

Tompalski, P., Coops, N. C., White, J. C., Goodbody, T. R. H., Hennigar, C. R., Wulder, M. A., Socha, J., & Woods, M. E. (2021). Estimating Changes in Forest Attributes and Enhancing Growth Projections: A Review of Existing Approaches and Future Directions Using Airborne 3D Point Cloud Data. *Current Forestry Reports*, *7*(1), 1–24. https://doi.org/10.1007/s40725-021-00135-w

Turkington, R. (2001). Boreal Forest Ecosystems. In *Encyclopedia of Biodiversity* (pp. 521–532). Elsevier. https://doi.org/10.1016/B0-12-226865-2/00036-5

Turner, M. G. (1989). *Landscape ecology: The Effect of Pattern on Process*.

Turner, M. G. (2005). Landscape Ecology: What Is the State of the Science? *Annual Review of Ecology, Evolution, and Systematics*, *36*(1), 319–344. https://doi.org/10.1146/annurev.ecolsys.36.102003.152614

Vahedifard, F., Abdollahi, M., Leshchinsky, B. A., Stark, T. D., Sadegh, M., & AghaKouchak, A. (2024). Interdependencies Between Wildfire-Induced Alterations in Soil Properties, Near-Surface Processes, and Geohazards. *Earth and Space Science*, *11*(2), e2023EA003498. https://doi.org/10.1029/2023EA003498

Vankat, J. L. (2002). Boreal and Temperate Forests. In John Wiley & Sons, Ltd (Ed.), *eLS* (1st ed.). Wiley. https://doi.org/10.1038/npg.els.0003738

Vogelmann, J. E., Gallant, A. L., Shi, H., & Zhu, Z. (2016). Perspectives on monitoring gradual change across the continuity of Landsat sensors using time-series data. *Remote Sensing of Environment*, *185*, 258–270. https://doi.org/10.1016/j.rse.2016.02.060

Vogt, P., Riitters, K. H., Estreguil, C., Kozak, J., & Wade, T. G. (2007). Mapping spatial patterns with morphological image processing. *Landscape Ecology*, *22*(2), 171–177.

Walker, W. S., Gorelik, S. R., Baccini, A., Aragon-Osejo, J. L., Josse, C., Meyer, C., Macedo, M. N., Augusto, C., Rios, S., Katan, T., De Souza, A. A., Cuellar, S., Llanos, A., Zager, I., Mirabal, G. D., Solvik, K. K., Farina, M. K., Moutinho, P., & Schwartzman, S. (2020). The role of forest conversion, degradation, and disturbance in the carbon dynamics of Amazon indigenous territories and protected areas. *Proceedings of the National Academy of Sciences*, *117*(6), 3015–3025. https://doi.org/10.1073/pnas.1913321117

Wells, J. V., Dawson, N., Culver, N., Reid, F. A., & Morgan Siegers, S. (2020). The State of Conservation in North America's Boreal Forest: Issues and Opportunities. *Frontiers in Forests and Global Change*, *3*, 90. https://doi.org/10.3389/ffgc.2020.00090

Westoby, M. J., Brasington, J., Glasser, N. F., Hambrey, M. J., & Reynolds, J. M. (2012). 'Structure-from-Motion' photogrammetry: A low-cost, effective tool for geoscience applications. *Geomorphology*, *179*, 300–314. https://doi.org/10.1016/j.geomorph.2012.08.021

White, J. C., Hermosilla, T., & Wulder, M. A. (2023). Pre-fire measures of boreal forest structure and composition inform interpretation of post-fire spectral recovery rates. *FOREST ECOLOGY AND MANAGEMENT*, *537*, 120948. https://doi.org/10.1016/j.foreco.2023.120948

White, J. C., Hermosilla, T., Wulder, M. A., & Coops, N. C. (2022). Mapping, validating, and interpreting spatio-temporal trends in post-disturbance forest recovery. *Remote Sensing of Environment*, *271*, 112904. https://doi.org/10.1016/j.rse.2022.112904

Wu, J. (2004). Effects of changing scale on landscape pattern analysis: Scaling relations. *Landscape Ecology*, *19*(2), 125–138. https://doi.org/10.1023/B:LAND.0000021711.40074.ae

Wu, J. (2013). Landscape Ecology. In R. Leemans (Ed.), *Ecological Systems* (pp. 179–200). Springer New York. https://doi.org/10.1007/978-1-4614-5755-8_11

Wu, W. J., Remmel, T. K., & Ouellette, M. (2025). Overlapping Landsat Scene Classifications and Focal Context to Identify Boreal Disturbance Mapping Uncertainty. *Geographical Analysis*, gean.12422. https://doi.org/10.1111/gean.12422

Wulder, M. A., White, J. C., Nelson, R. F., Næsset, E., Ørka, H. O., Coops, N. C., Hilker, T., Bater, C. W., & Gobakken, T. (2012). Lidar sampling for large-area forest characterization: A review. *Remote Sensing of Environment*, *121*, 196–209. https://doi.org/10.1016/j.rse.2012.02.001

Zhang, B., Prober, S. M., O'Donnell, A., Gosper, C. R., Fischer, F., Zdunic, K., & Jucker, T. (2025). Long-term recovery of canopy 3D structural diversity following wildfires in the world's largest temperate woodland. *Proceedings of the Royal Society B: Biological Sciences*, *292*(2059), 20251095. https://doi.org/10.1098/rspb.2025.1095

# 7 Appendix A: Development notes for the *morphpy* 3D morphological segmentation algorithm

The *morphpy* codebase is organized into two main scripts: `morph3d.py` and `utils.py`. The core segmentation logic resides in `morph3d.py`, while `utils.py` contains supporting functions used for preprocessing, neighbour identification, and visualization. This separation allows the main algorithm to remain readable and focused, while common operations are handled in reusable components

This appendix presents the full *morphpy* segmentation script, morph3d.py, used to perform 3D morphological classification, and explains the *morphpy* codebase's structure and how the segmentation algorithm operates. The code is presented as a complete script, and the development note provides a technical description of the implementation to support it.

The overall execution flow begins in `morph3d()`, which calls several helper functions from utils.py at different stages of the segmentation process. All outputs are assembled and returned by morph3d() at the end of execution. The script *morph3d.py* implements the full three-dimensional morphological segmentation pipeline. Its central function, `morph3d()`, accepts a three-dimensional NumPy array named `DATACUBE`, where values of 1 represent the feature of interest and values of 0 represent background. The array is interpreted as a volumetric structure, with the first two dimensions representing space and the third dimension representing depth, which in this study corresponds to time.

The function begins by validating the input cube to ensure that it is numeric, three-dimensional, and strictly binary. This validation step prevents malformed inputs from propagating errors through later stages of the algorithm. Once validated, the input cube is padded by one voxel on all sides. This padding allows neighbour checks to be performed safely at the boundaries of the original array without requiring special edge handling logic. Each voxel in the original cube is then assigned a unique identifier. These identifiers are used to track voxel relationships during graph construction and segmentation. Several working arrays are initialized at this stage, including arrays for object labels, core labels, expanded core labels, and final morphology codes.

Neighbour relationships are computed using six-directional connectivity. For each voxel, orthogonal neighbours in the positive and negative $x$, $y$, and $t$ directions are identified. These neighbour relationships are filtered to retain only valid connections between foreground voxels.

The resulting voxel pairs are used to construct an undirected graph in which nodes represent voxels and edges represent direct adjacency. The graph is decomposed into connected components, each representing a discrete object in the volume. These components are processed independently to prevent interactions between unrelated structures. Each voxel is assigned an object identifier corresponding to the connected component to which it belongs.

Morphological classification proceeds in a fixed sequence. Voxels with six neighbouring foreground connections are first identified as MASS and assigned code 2. These voxels represent fully enclosed interior regions. SKIN voxels are then identified as foreground voxels adjacent to MASS voxels but not part of the core and are assigned code 3. Objects that contain neither MASS nor SKIN voxels are classified entirely as CRUMB, representing isolated or minimal structures, and assigned code 4.

All remaining foreground voxels that have not yet been classified are temporarily labelled as CONNECTOR voxels with code 5. At this stage, all remaining unclassified background voxels are explicitly labelled as OUTSIDE with code 1 to complete the base classification. Connector voxels are then refined into ANTENNA, BOND, or CIRCUIT classes based on their connectivity. ANTENNA voxels form chains that connect to a single core region and terminate without linking to another core. These are identified by removing core-related voxels from the graph and analysing the remaining subgraphs. Single-voxel connectors are handled explicitly to avoid misclassification. ANTENNA voxels are assigned code 6. BOND voxels are identified next. These form structural bridges between two or more distinct core regions. Core regions are first identified and assigned unique core identifiers. Connector subgraphs that link multiple cores are then classified as BOND and assigned code 7. Any neighbouring connector voxels that are directly adjacent to BOND voxels are re-evaluated to ensure consistent classification.

Connector voxels that are neither ANTENNA nor BOND are retained as CIRCUIT voxels and assigned code 5. These typically represent closed loops or internal filament structures that do not function as branches or bridges. Void detection is performed after all foreground structures have been classified. A flood-fill procedure is applied to the padded array to identify background regions that are reachable from the exterior. Any background voxels that remain enclosed after this process are classified as VOID-VOLUME and assigned code 8. Finally, SKIN voxels that directly border VOID-VOLUME regions are reclassified as VOID and assigned code 9, distinguishing internal boundaries from external surfaces. morph3d

Once classification is complete, summary statistics are generated. These include voxel counts and relative percentages for each morphological class. Optional three-dimensional visualizations can be produced at intermediate and final stages of the algorithm. The function concludes by returning a structured output object containing the classified voxel array, summary tables, graph objects, diagnostic arrays, and runtime metrics.

## 8 Appendix B: *morphpy* core segmentation algorithm

```
def _fmt_bytes(n):
    for unit in ("B", "KB", "MB", "GB", "TB"):
        if n < 1024 or unit == "TB":
            return f"{n:.2f} {unit}"
        n /= 1024


import numpy as np
from collections import deque

#Supporting Functions
NBRS6 = [
    (1, 0, 0), (-1, 0, 0),
    (0, 1, 0), (0, -1, 0),
    (0, 0, 1), (0, 0, -1),
]


def _flood_fill_outside_to_neg1(vv):
    X, Y, Z = vv.shape
    q = deque()

    for x in [0, X - 1]:
        for y in range(Y):
            for z in range(Z):
                q.append((x, y, z))
    for x in range(X):
        for y in [0, Y - 1]:
            for z in range(Z):
                q.append((x, y, z))
    for x in range(X):
        for y in range(Y):
            for z in [0, Z - 1]:
                q.append((x, y, z))

    checked = np.zeros(vv.shape, dtype=bool)

    while q:
        x, y, z = q.popleft()
        if checked[x, y, z]:
            continue
        checked[x, y, z] = True

        if vv[x, y, z] == 0:
            vv[x, y, z] = -1

        if vv[x, y, z] == -1:
            for dx, dy, dz in NBRS6:
                nx, ny, nz = x + dx, y + dy, z + dz
```

```
                if 0 <= nx < X and 0 <= ny < Y and 0 <= nz < Z and not checked[nx, ny, nz]:
                    if vv[nx, ny, nz] in (-1, 0):
                        q.append((nx, ny, nz))

    return vv


def _collect_connected_zero_region(enclosed_mask, start):
    X, Y, Z = enclosed_mask.shape
    q = deque([start])
    checked_local = {start}
    region = []

    while q:
        x, y, z = q.popleft()
        region.append((x, y, z))

        for dx, dy, dz in NBRS6:
            nx, ny, nz = x + dx, y + dy, z + dz
            if 0 <= nx < X and 0 <= ny < Y and 0 <= nz < Z:
                if enclosed_mask[nx, ny, nz] and (nx, ny, nz) not in checked_local:
                    checked_local.add((nx, ny, nz))
                    q.append((nx, ny, nz))

    return region


def _validate_and_build_void_shell(region, datacube, voidvolume_bg):
    X, Y, Z = datacube.shape
    shell1 = set()

    # Build immediate shell around the 0-region
    for x, y, z in region:
        for dx, dy, dz in NBRS6:
            nx, ny, nz = x + dx, y + dy, z + dz

            if not (0 <= nx < X and 0 <= ny < Y and 0 <= nz < Z):
                return False, set()

            if datacube[nx, ny, nz] == 1:
                shell1.add((nx, ny, nz))

    if len(shell1) == 0:
        return False, set()

    # Candidate VOID shell must itself be internal, not exposed to outside
    for x, y, z in shell1:
        for dx, dy, dz in NBRS6:
            nx, ny, nz = x + dx, y + dy, z + dz
            if 0 <= nx < X and 0 <= ny < Y and 0 <= nz < Z:
                if voidvolume_bg[nx, ny, nz] == -1:
```

```
                    return False, set()

    return True, shell1


def _find_valid_void_regions(datacube):
    """
    Returns:
      valid_void_mask: bool mask for VOID-VOLUME voxels
      void_shell_mask: bool mask for immediate valid VOID shell voxels
      voidvolume_bg: flood-filled background cube cropped to original size
    """
    dimx, dimy, dimz = datacube.shape

    # padded background cube for flood fill
    lrgdatacube = np.zeros((dimx + 2, dimy + 2, dimz + 2), dtype=int)
    lrgdatacube2 = lrgdatacube - 1
    lrgdatacube[1:-1, 1:-1, 1:-1] = datacube
    lrgdatacube2[1:-1, 1:-1, 1:-1] = datacube

    # flood fill true outside
    voidvolume = _flood_fill_outside_to_neg1(lrgdatacube2.copy())
    voidvolume = voidvolume[1:-1, 1:-1, 1:-1]

    enclosed_mask = (voidvolume == 0)

    valid_void_mask = np.zeros_like(enclosed_mask, dtype=bool)
    void_shell_mask = np.zeros_like(enclosed_mask, dtype=bool)
    checked = np.zeros_like(enclosed_mask, dtype=bool)

    starts = np.argwhere(enclosed_mask)
    for sx, sy, sz in starts:
        if checked[sx, sy, sz]:
            continue

        region = _collect_connected_zero_region(enclosed_mask, (sx, sy, sz))
        for rx, ry, rz in region:
            checked[rx, ry, rz] = True

        is_valid, shell1 = _validate_and_build_void_shell(region, datacube, voidvolume)

        if is_valid:
            for rx, ry, rz in region:
                valid_void_mask[rx, ry, rz] = True
            for vx, vy, vz in shell1:
                void_shell_mask[vx, vy, vz] = True

    return valid_void_mask, void_shell_mask, voidvolume


def morph3d(
```

```
    DATACUBE=None,
    VERBOSE=False,
    PLOT=False,
    FINALPLOT=True,
    PLOTIDS=None,
    AUTOSAVE=True,
    SAVE_DIR="morph_outputs",
    SAVE_PREFIX="morph3d",
    SAVE_DPI=300,
    YEARS=None,
    SITE_ID="site",
    SAVE_MORPH_ARRAY=True,
):

    import os
    import time
    import psutil
    import igraph as ig
    import matplotlib.pyplot as plt
    from mpl_toolkits.mplot3d.art3d import Poly3DCollection
    from mpl_toolkits.mplot3d import Axes3D
    import numpy as np
    import pandas as pd
    import networkx as nx
    from pathlib import Path
    from datetime import datetime
    from itertools import product
    from .utils import morph3dlinks, morph3dplot, morph3dprep, validate_data_cube, arraytrim

    timestamp = datetime.now().strftime("%Y%m%d_%H%M%S")
    if AUTOSAVE:
        run_folder = Path(SAVE_DIR) / f"{SAVE_PREFIX}_{SITE_ID}_{timestamp}"
        run_folder.mkdir(parents=True, exist_ok=True)
    else:
        run_folder = None
    def _savepath(name: str):
        if not AUTOSAVE or run_folder is None:
            return None
        return str(run_folder / f"{SAVE_PREFIX}_{SITE_ID}_{name}_{timestamp}.svg")

    _proc = psutil.Process(os.getpid())
    _start_ts = time.time()
    _start_ts_str = time.strftime("%Y-%m-%d %H:%M:%S", time.localtime(_start_ts))
    _start_rss = _proc.memory_info().rss
    try:
        _peak = getattr(_proc.memory_full_info(), "peak_wset", None) or getattr(
            _proc.memory_full_info(), "peak_rss", None
        )
    except Exception:
        _peak = None
```

```
valid_data = validate_data_cube(datacube=DATACUBE)
if not valid_data:
    print("ERROR: Invalid Data Cube Provided")

if VERBOSE:
    print("\nInsetting 3D data cube into a larger array to handle edge effects")

dimdatacube = DATACUBE.shape

lrgdatacube = np.zeros(
    (dimdatacube[0] + 2, dimdatacube[1] + 2, dimdatacube[2] + 2), dtype=int
)
lrgdatacube2 = lrgdatacube - 1
lrgdatacube[1:dimdatacube[0] + 1, 1:dimdatacube[1] + 1, 1:dimdatacube[2] + 1] = DATACUBE
lrgdatacube2[1:dimdatacube[0] + 1, 1:dimdatacube[1] + 1, 1:dimdatacube[2] + 1] = DATACUBE

if VERBOSE:
    print("\n\n    Performing initializations of: voxelID, objectID, coreCode, and morphCode arrays")

voxelID = np.arange(1, np.prod(DATACUBE.shape) + 1).reshape(DATACUBE.shape)
objectID = np.zeros_like(voxelID)
coreCode = np.zeros_like(objectID)
expandedCoreCode = np.copy(coreCode)
morphCode = np.zeros_like(objectID)

if VERBOSE:
    print("\n   Computing neighbours")

neighbour = morph3dlinks(VOLOBJ=lrgdatacube, VOXELIDS=voxelID)
neighbourtab = neighbour.iloc[:, 1:8].copy()

goodIDs = voxelID[DATACUBE == 1]
for row in range(neighbourtab.shape[0]):
    neighbourtab.iloc[row, ~neighbourtab.iloc[row].isin(goodIDs)] = 0

newneighbourtab = neighbourtab.iloc[:, 0].to_frame()
newneighbourtab = pd.concat([newneighbourtab] * 6, ignore_index=True)
vectorised_data = neighbourtab.iloc[:, 1:7].values.flatten("F")
newneighbourtab = pd.concat(
    [newneighbourtab, pd.Series(vectorised_data, name="Flatten_data")], axis=1
)

sorted_rows = np.apply_along_axis(np.sort, axis=1, arr=newneighbourtab)
unique_rows_mask = ~pd.DataFrame(sorted_rows).duplicated(keep="first")
newneighbourtab = newneighbourtab[unique_rows_mask]

if VERBOSE:
    print("\n  Generating network graph object")

import networkx as nx
maingraph = nx.from_pandas_edgelist(
```

```
    newneighbourtab,
    source="VOXELIDS",
    target="Flatten_data",
    create_using=nx.Graph(),
)

if 0 in maingraph.nodes():
    cutgraph = maingraph.copy()
    cutgraph.remove_node(0)
else:
    cutgraph = maingraph.copy()

connected_components = nx.connected_components(cutgraph)
decompgraph = [cutgraph.subgraph(component).copy() for component in connected_components]

if VERBOSE:
    print("\n  There are", len(decompgraph), "discrete objects in this graph")
    print("\n  Initiating the 3D morphological segmentation")

for uq, cluster in enumerate(decompgraph):
    b = list(cluster)
    numvoxels = len(b)
    for vox in range(numvoxels):
        objectID[voxelID == b[vox]] = uq + 1

if PLOT:
    objmask = np.where(objectID > 0, 10, 0).astype(np.uint8)
    morphs = morph3dprep(objmask)
    morph3dplot(
        morphs,
        plot_codes=[10],
        show_skin=False,
        show_outside=False,
        CELLID=None if not PLOTIDS else PLOTIDS,
        LEGEND=False,
        ORIGTRANSP=False,
        title="Objects IDs",
        save_path=_savepath("ObjectMask"),
        save_dpi=SAVE_DPI,
    )

# ------------ MASS (CODE = 2) ------------
if VERBOSE:
    print("\n\n  Identifying MASS voxels")

for uq, g in enumerate(decompgraph, start=1):
    deg = dict(g.degree())
    sel = [node for node, d in deg.items() if d == 6]

    if VERBOSE:
        print(f"\n    Processing unique object {uq} of {len(decompgraph)}")
```

```
        if sel:
            print(f"      There are {len(sel)} MASS voxels in this unique object")
        else:
            print("      There are no MASS voxels in this unique object")

    for node in sel:
        morphCode[voxelID == node] = 2

if PLOT:
    plotmorph = np.zeros_like(morphCode)
    plotmorph[morphCode == 2] = 2
    morphs = morph3dprep(plotmorph)
    morph3dplot(
        morphs,
        CELLID=PLOTIDS,
        LEGEND=False,
        ORIGTRANSP=False,
        title="MASS Voxels",
        save_path=_savepath("MASS"),
        save_dpi=SAVE_DPI,
    )

# ------------ SKIN (CODE = 3) ------------
if VERBOSE:
    print("\n\n  Identifying SKIN voxels")

for components in nx.connected_components(cutgraph):
    subgraph = cutgraph.subgraph(components)
    component_degree = dict(subgraph.degree())
    massIDS = [key for key, value in component_degree.items() if value == 6]
    numMASS = len(massIDS)

    if numMASS > 0:
        for massID in massIDS:
            MASSneigh = list(subgraph.neighbors(massID))
            MASSneigh = [neighbor for neighbor in MASSneigh if neighbor not in massIDS]

            if MASSneigh:
                for newrep in range(len(MASSneigh)):
                    morphCode[voxelID == MASSneigh[newrep]] = 3

# ------------ CRUMB (CODE = 4) ------------
allMASS = voxelID[morphCode == 2]
allSKIN = voxelID[morphCode == 3]

if VERBOSE:
    print("\n\n  Identifying CRUMB voxels")

for uq in range(len(decompgraph)):
    print(f"Processing unique object {uq+1} of {len(decompgraph)}")
    if len(decompgraph[uq]) == 1:
```

```
        print("Object has only 1 voxel, thus it is a CRUMB")
        morphCode[voxelID == list(decompgraph[uq])[0]] = 4
    else:
        curVoxels = list(decompgraph[uq])
        print(f"object has more than 1 voxels. It has: {len(curVoxels)}")
        if any(vox in allMASS for vox in curVoxels):
            print("Not a CRUMB since it connects to a MASS")
        else:
            if any(vox in allSKIN for vox in curVoxels):
                print("Not a CRUMB since it connects to a SKIN")
            else:
                print(f"There are {len(curVoxels)} CRUMB voxels in this object")
                for rep in range(len(curVoxels)):
                    morphCode[voxelID == curVoxels[rep]] = 4

if PLOT:
    plotmorph = np.zeros_like(morphCode)
    plotmorph[morphCode == 4] = 4
    morphs = morph3dprep(plotmorph)
    morph3dplot(
        morphs,
        CELLID=PLOTIDS,
        LEGEND=False,
        ORIGTRANSP=False,
        title="CRUMB Voxels",
        save_path=_savepath("CRUMB"),
        save_dpi=SAVE_DPI,
    )

# ------------ CONNECTOR (CODE = 5) ------------
if VERBOSE:
    print("\n\n  Identifying CONNECTOR voxels")

morphCode[(DATACUBE > 0) & (morphCode == 0)] = 5
morphCode[morphCode == 0] = 1

if VERBOSE:
    print(f"\n    There are {len(voxelID[morphCode == 5])} generic CONNECTOR voxels")
    print("\n\n  Identifying OUTSIDE voxels")
    print(f"\n    There are {len(voxelID[morphCode == 1])} OUTSIDE voxels")

# ------------ ANTENNA (CODE = 6) ------------
if VERBOSE:
    print("\n\n  Identifying ANTENNA voxels")

MASSVoxels = voxelID[morphCode == 2]
SKINVoxels = voxelID[morphCode == 3]
CONNECTORVoxels = voxelID[morphCode == 5]

for obj in range(len(decompgraph)):
    if VERBOSE:
```

```
    print(f"\n    Processing object {obj + 1} of {len(decompgraph)} in gph.")

MassVoxelsInObject = [v for v in MASSVoxels if v in decompgraph[obj]]
SkinVoxelsInObject = [v for v in SKINVoxels if v in decompgraph[obj]]
ConnectorVoxelsInObject = [v for v in CONNECTORVoxels if v in decompgraph[obj]]

if VERBOSE:
    print("\n    MassVoxelsInObject:", MassVoxelsInObject)
    print("      SkinVoxelsInObject:", SkinVoxelsInObject)
    print("      ConnectorVoxelsInObject:", ConnectorVoxelsInObject)

if len(MassVoxelsInObject) > 0:
    if VERBOSE:
        print(f"\n      Object {obj + 1}: There are MASS and SKIN voxels to delete")

    gph2 = decompgraph[obj].copy()
    gph2.remove_nodes_from(MassVoxelsInObject)
    gph3 = gph2.copy()
    gph3.remove_nodes_from(SkinVoxelsInObject)

    if VERBOSE:
        print("\n      Decomposing...")

    gph4 = [gph3.subgraph(c).copy() for c in nx.connected_components(gph3)]
    numSubparts = len(gph4)

    if VERBOSE:
        print(f"\n      The decomposed graph now has {numSubparts} sub parts")

    for connector, subgraph in enumerate(gph4):
        if VERBOSE:
            print(f"\n\n        On sub part {connector + 1} of {numSubparts}")

        ConnectorVoxelsInSubGraph = [v for v in CONNECTORVoxels if v in subgraph.nodes]

        if VERBOSE:
            print(f"           Vertices: {list(subgraph.nodes)}")

        if len(gph4[connector].nodes) == 1:
            if VERBOSE:
                print("\n          Single voxel antenna")

            voxID = int(next(iter(gph4[connector].nodes)))
            locco = np.argwhere(voxelID == voxID)
            morphCode[tuple(locco[0])] = 6

            loc = np.argwhere(voxelID == voxID)
            counter = 0
            directions = NBRS6

            for dx, dy, dz in directions:
```

```
                    neighbor_loc = (loc[0][0] + dx, loc[0][1] + dy, loc[0][2] + dz)
                    if (
                        0 <= neighbor_loc[0] < dimdatacube[0]
                        and 0 <= neighbor_loc[1] < dimdatacube[1]
                        and 0 <= neighbor_loc[2] < dimdatacube[2]
                    ):
                        neighbor_val = morphCode[neighbor_loc]
                        if neighbor_val == 2:
                            counter += 1

                if counter == 1:
                    morphCode[voxelID == ConnectorVoxelsInSubGraph] = 6
                else:
                    morphCode[voxelID == ConnectorVoxelsInSubGraph] = 5

                checkcounter = 0
                for dx, dy, dz in directions:
                    neighbor_loc = (loc[0][0] + dx, loc[0][1] + dy, loc[0][2] + dz)
                    if (
                        0 <= neighbor_loc[0] < dimdatacube[0]
                        and 0 <= neighbor_loc[1] < dimdatacube[1]
                        and 0 <= neighbor_loc[2] < dimdatacube[2]
                    ):
                        neighbor_val = morphCode[neighbor_loc]
                        if neighbor_val == 3:
                            checkcounter += 1

                if checkcounter == 1:
                    morphCode[tuple(locco[0])] = 6

        if VERBOSE:
            print("\n      Done with object", obj + 1)

    else:
        if VERBOSE:
            print("\n      There are no MASS and SKIN voxels; therefore there are no possible connectors to process")
            print("\n      Done with object", obj + 1)

if VERBOSE:
    print("\n\n  Finished identifying ANTENNA voxels\n")

# ------------ BOND (CODE = 7) ------------
if VERBOSE:
    print("\n\n  Identifying BOND voxels")
    print("\n    Identifying unique cores of MASS voxels")

for _, obj_graph in enumerate(decompgraph):
    MASSVoxels = voxelID[morphCode == 2]
    MassVoxelsInObj = [v for v in MASSVoxels if v in obj_graph.nodes]

    if len(MassVoxelsInObj) > 0:
```

```
        if VERBOSE:
            print("\n    Need to provide unique IDs to each core of MASS")

        obj_core_graph = obj_graph.copy()
        notMASS = [int(v) for v in obj_graph.nodes if v not in MassVoxelsInObj]
        obj_core_graph.remove_nodes_from(notMASS)

        components = list(nx.connected_components(obj_core_graph))
        numcores = len(components)

        if VERBOSE:
            print(f"\n    There are {numcores} core MASSES in this object")

        for _, core_nodes in enumerate(components):
            coreID = coreCode.max() + 1
            MassInCore = list(core_nodes)

            for voxel in MassInCore:
                coreCode[voxelID == voxel] = coreID

            expandedCoreCode[np.isin(voxelID, MassInCore)] = coreID

            inclSKIN = set()
            for voxel in MassInCore:
                neighbors = list(obj_graph.neighbors(voxel))
                inclSKIN.update(neighbors)

            MASSSKIN = set(inclSKIN)
            inclfirstconnector = set()
            for voxel in MASSSKIN:
                neighbors = list(obj_graph.neighbors(voxel))
                inclfirstconnector.update(neighbors)

            combined = np.unique(list(MASSSKIN.union(inclfirstconnector)))

            for voxel in combined:
                expandedCoreCode[voxelID == voxel] = coreID
    else:
        if VERBOSE:
            print("\n    No MASS in this object; therefore no cores")

print("\n\n  Cores, if present have been identified and coded\n")

if PLOT:
    plotmorph = expandedCoreCode
    morphs = morph3dprep(plotmorph)
    morph3dplot(
        morphs,
        CELLID=PLOTIDS,
        LEGEND=False,
        ORIGTRANSP=False,
```

```
        title="Expanded CORE Voxels",
    )
    print("Expanded CORE Voxels")

if VERBOSE:
    print("\n\n  Starting secondary test for ANTENNA detection")

for obj in range(len(decompgraph)):
    if VERBOSE:
        print(f"\n\n  ANTENNA FIX object: {obj + 1}")

    has_mass = np.any((morphCode == 2) & (objectID == obj + 1))
    if not has_mass:
        if VERBOSE:
            print(f"Object {obj+1} has no MASS, skipping")
        continue

    if VERBOSE:
        print(f"Object {obj+1} has MASS, processing")

    possible = voxelID[(morphCode == 5) & (expandedCoreCode == 0) & (objectID == obj + 1)]
    allinobj = list(decompgraph[obj].nodes)
    to_delete = [node for node in allinobj if node not in possible]

    tmpgph = decompgraph[obj].copy()
    tmpgph.remove_nodes_from(to_delete)
    subgraphs = list(nx.connected_components(tmpgph))

    if VERBOSE:
        print(f"Object has {len(subgraphs)} possible ANTENNA to test for connectivity")

    for subgraph_nodes in subgraphs:
        subgraph = tmpgph.subgraph(subgraph_nodes).copy()
        if len(subgraph.nodes) <= 1:
            continue

        endpoints = [node for node, degree in subgraph.degree if degree == 1]
        if VERBOSE:
            print(f"Subgraph endpoints: {endpoints}")

        plugpoints = {ep: list(maingraph.neighbors(ep)) for ep in endpoints}
        if not plugpoints:
            continue

        tab = {ep: plugpoints[ep] for ep in endpoints}
        tab2 = {
            ep: [expandedCoreCode[voxelID == n] if n in voxelID else 0 for n in neighbors]
            for ep, neighbors in tab.items()
        }

        cores_linked = {int(core) for neighbors in tab2.values() for core in neighbors if core > 0}
```

```
        if len(cores_linked) == 1:
            rowsums = [sum(1 for core in neighbors if core > 0) for neighbors in tab2.values()]
            if sum(rowsums) == 1:
                for node in subgraph.nodes:
                    morphCode[voxelID == node] = 6

        elif len(cores_linked) > 1:
            for node in subgraph.nodes:
                morphCode[voxelID == node] = 7

            if VERBOSE:
                print("An update of CIRCUIT to BOND is required")

            for node in subgraph.nodes:
                loc = np.where(voxelID == node)
                neighbors = {
                    "xlow": morphCode[loc[0] - 1, loc[1], loc[2]] if loc[0] > 0 else 0,
                    "xhigh": morphCode[loc[0] + 1, loc[1], loc[2]] if loc[0] < dimdatacube[0] - 1 else 0,
                    "ylow": morphCode[loc[0], loc[1] - 1, loc[2]] if loc[1] > 0 else 0,
                    "yhigh": morphCode[loc[0], loc[1] + 1, loc[2]] if loc[1] < dimdatacube[1] - 1 else 0,
                    "zlow": morphCode[loc[0], loc[1], loc[2] - 1] if loc[2] > 0 else 0,
                    "zhigh": morphCode[loc[0], loc[1], loc[2] + 1] if loc[2] < dimdatacube[2] - 1 else 0,
                }
                for key, val in neighbors.items():
                    if val == 5:
                        indices = {
                            "xlow": (loc[0] - 1, loc[1], loc[2]),
                            "xhigh": (loc[0] + 1, loc[1], loc[2]),
                            "ylow": (loc[0], loc[1] - 1, loc[2]),
                            "yhigh": (loc[0], loc[1] + 1, loc[2]),
                            "zlow": (loc[0], loc[1], loc[2] - 1),
                            "zhigh": (loc[0], loc[1], loc[2] + 1),
                        }
                        morphCode[indices[key]] = 7

if PLOT:
    plotmorph = np.zeros_like(morphCode)
    plotmorph[morphCode == 6] = 6
    morphs = morph3dprep(plotmorph)
    morph3dplot(
        morphs,
        CELLID=PLOTIDS,
        LEGEND=False,
        ORIGTRANSP=False,
        title="ANTENNA Voxels",
        save_path=_savepath("ANTENNA"),
        save_dpi=SAVE_DPI,
    )

if PLOT:
```

```
    plotmorph = np.zeros_like(morphCode)
    plotmorph[morphCode == 7] = 7
    morphs = morph3dprep(plotmorph)
    morph3dplot(
        morphs,
        CELLID=PLOTIDS,
        LEGEND=False,
        ORIGTRANSP=False,
        title="BOND Voxels",
        save_path=_savepath("BOND"),
        save_dpi=SAVE_DPI,
    )

if PLOT:
    plotmorph = np.zeros_like(morphCode)
    plotmorph[morphCode == 5] = 5
    morphs = morph3dprep(plotmorph)
    morph3dplot(
        morphs,
        CELLID=PLOTIDS,
        LEGEND=False,
        ORIGTRANSP=False,
        title="CIRCUIT Voxels",
        save_path=_savepath("CIRCUIT"),
        save_dpi=SAVE_DPI,
    )

# ------------ VOID-VOLUME (CODE = 8) + VOID (CODE = 9) ------------
if VERBOSE:
    print("\n\nIdentifying VOID-VOLUME and VOID voxels")

valid_void_mask, void_shell_mask, voidvolume = _find_valid_void_regions(DATACUBE)

# There cannot be VOID-VOLUME without VOID
# so assign both together only for validated regions
morphCode[valid_void_mask] = 8

object_codes = {2, 3, 4, 5, 6, 7}
morphCode[void_shell_mask & np.isin(morphCode, list(object_codes))] = 9

if PLOT:
    plotmorph = np.zeros_like(morphCode)
    plotmorph[morphCode == 8] = 8
    morphs = morph3dprep(plotmorph)
    morph3dplot(
        morphs,
        CELLID=PLOTIDS,
        LEGEND=False,
        ORIGTRANSP=False,
        title="VOID-VOLUME Voxels",
        save_path=_savepath("VOIDVOLUME"),
```

```
        save_dpi=SAVE_DPI,
    )

if PLOT:
    plotmorph = np.zeros_like(morphCode)
    plotmorph[morphCode == 9] = 9
    morphs = morph3dprep(plotmorph)
    morph3dplot(
        morphs,
        CELLID=PLOTIDS,
        LEGEND=False,
        ORIGTRANSP=False,
        title="VOID Voxels",
        save_path=_savepath("VOID"),
        save_dpi=SAVE_DPI,
    )

if PLOT:
    plotmorph = np.zeros_like(morphCode)
    plotmorph[morphCode == 3] = 3
    morphs = morph3dprep(plotmorph)
    morph3dplot(
        morphs,
        CELLID=PLOTIDS,
        LEGEND=False,
        ORIGTRANSP=False,
        title="SKIN Voxels",
        save_path=_savepath("SKIN"),
        save_dpi=SAVE_DPI,
    )

# ------------ FINISHING UP ------------
descriptions = [
    "OUTSIDE", "MASS", "SKIN", "CRUMB",
    "CIRCUIT", "ANTENNA", "BOND", "VOID-VOLUME", "VOID"
]
summaries = []

for code in range(1, 10):
    n_voxels = np.sum(morphCode == code)
    percentage = (n_voxels / np.max(voxelID)) * 100
    summaries.append([code, descriptions[code - 1], n_voxels, percentage])

summaries_df = pd.DataFrame(
    summaries,
    columns=["Code", "Description", "NVoxels", "Percentage"],
)

if VERBOSE:
    print("\n\nSummary of Morphology Codes:\n")
    print(summaries_df)
```

```
    print("\n")

if FINALPLOT:
    morphs = morph3dprep(morphCode, orig=False, FINAL=False)
    morph3dplot(
        morphs,
        CELLID=PLOTIDS,
        LEGEND=False,
        ORIGTRANSP=False,
        title="3D Morphology",
        save_path=_savepath("3D_Morphology"),
        save_dpi=SAVE_DPI,
        full_shape=morphCode.shape,
    )
    print("3D Morphology")

_end_ts = time.time()
_end_ts_str = time.strftime("%Y-%m-%d %H:%M:%S", time.localtime(_end_ts))
_elapsed = _end_ts - _start_ts
_end_rss = _proc.memory_info().rss
try:
    _peak_now = getattr(_proc.memory_full_info(), "peak_wset", None) or getattr(
        _proc.memory_full_info(), "peak_rss", None
    )
    if _peak_now:
        _peak = max((_peak or 0), _peak_now)
except Exception:
    pass

RunMetrics = {
    "start_time_str": _start_ts_str,
    "end_time_str": _end_ts_str,
    "elapsed_seconds": float(f"{_elapsed:.3f}"),
    "start_rss_bytes": int(_start_rss),
    "end_rss_bytes": int(_end_rss),
    "peak_rss_bytes": int(_peak) if _peak is not None else None,
    "start_rss_hr": _fmt_bytes(_start_rss),
    "end_rss_hr": _fmt_bytes(_end_rss),
    "peak_rss_hr": _fmt_bytes(_peak) if _peak is not None else None,
}

if VERBOSE:
    print("\n--- Run Metrics ---")
    print(f"Start:   {RunMetrics['start_time_str']}")
    print(f"End:     {RunMetrics['end_time_str']}")
    print(f"Elapsed: {RunMetrics['elapsed_seconds']} s")
    print(f"RSS:     {RunMetrics['start_rss_hr']} → {RunMetrics['end_rss_hr']}")
    if RunMetrics["peak_rss_hr"] is not None:
        print(f"Peak RSS (best-effort): {RunMetrics['peak_rss_hr']}")
    print("-----------------------------------------------------------------")
```

```
    morphCode_xyz = morphCode.copy()

    outobj = {
        "OriginalData": DATACUBE,
        "Graph": decompgraph,
        "VoxelIDs": voxelID,
        "ObjectID": objectID,
        "Morphology": morphCode_xyz,
        "Cores": coreCode,
        "ExpCores": expandedCoreCode,
        "Summary": summaries_df,
        "Egg": maingraph,
        "Bgrnd": lrgdatacube2,
        "VOIDvolume": voidvolume,
        "RunMetrics": RunMetrics,
    }
#Autosaving the 3D Morphology Array
    if AUTOSAVE and SAVE_MORPH_ARRAY and run_folder is not None:
        cube = np.asarray(morphCode_xyz).astype(int)
        if YEARS is None:
            YEARS = list(range(cube.shape[0]))
        T_expected = len(YEARS)
        shape = cube.shape
        time_axes = [ax for ax, n in enumerate(shape) if n == T_expected]
        if not time_axes:
            raise ValueError(
                f"None of the morphology cube dimensions match len(YEARS)={T_expected}. "
                f"Morphology shape is {shape}. Check YEARS or cube orientation."
            )
        t_axis = time_axes[0]
        cube_txy = np.moveaxis(cube, t_axis, 0)
        T, X, Y = cube_txy.shape
        blocks = []
        for ti in range(T):
            grid = pd.DataFrame(cube_txy[ti])
            blocks.append(grid)
            blocks.append(pd.DataFrame([[np.nan] * Y]))
        stacked = pd.concat(blocks, ignore_index=True)
        years_start = YEARS[0]
        years_end = YEARS[-1]
        out_csv = run_folder / f"{SITE_ID}_morph_codes_PUREGRID_{years_start}_{years_end}_{timestamp}.csv"
        stacked.to_csv(out_csv, index=False, header=False)
        map_rows = []
        row = 1
        for yr in YEARS:
            start = row
            end = row + (X - 1)
            map_rows.append([yr, start, end])
            row = end + 2
        map_df = pd.DataFrame(map_rows, columns=["Year", "StartRow", "EndRow"])
        map_csv = run_folder / f"{SITE_ID}_PUREGRID_row_map_{years_start}_{years_end}_{timestamp}.csv"
```

```
    map_df.to_csv(map_csv, index=False)
    outobj["MorphologyCSV"] = str(out_csv)
    outobj["MorphologyRowMapCSV"] = str(map_csv)
    outobj["RunFolder"] = str(run_folder)
    if VERBOSE:
        print("Morphology array saved:", out_csv)
        print("Row map saved:", map_csv)

return outobj
```

# 9 Appendix C. Development notes for the *morphpy* supporting code (utils)

The script utils.py provides supporting functions used throughout the segmentation pipeline. These functions do not make classification decisions. Instead, they enable preprocessing, neighbour identification, and visualization.

The function `validate_data_cube()` checks that the input array is a NumPy array, numeric, three-dimensional, and binary. This function is called at the start of `morph3d()` to ensure input integrity.

The function `arraytrim()` removes empty planes of background voxels from the edges of a three-dimensional array. This is useful when working with site-based voxel cubes that contain large margins of zeros. Trimming reduces memory usage and improves computational efficiency without altering the structural connectivity.

Neighbour relationships are constructed using the `morph3dlinks()` function. This function shifts voxel identifier arrays in six orthogonal directions to identify adjacent voxels. The results are assembled into a tabular format, with each row corresponding to a foreground voxel and its potential neighbours. This table forms the basis for graph construction in morph3d.py.

Visualization support is provided through the functions `morph3dprep()` and `morph3dplot()`. The `morph3dprep()` function converts a three-dimensional array into a tabular format suitable for plotting, with explicit *x*, *y*, and *t* coordinates. The `morph3dplot()` function renders three-dimensional voxel plots using consistent colour schemes for each morphological class. Options are provided to control transparency, background style, wireframe display, and axis scaling, allowing voxels to be displayed as geometrically accurate cubes.

Plotting functions are optional and can be disabled during execution. This allows the segmentation algorithm to be applied efficiently in automated or large-scale processing environments where visual output is unnecessary.

## 10 Appendix D. *morphpy* supporting code (utils)

```
import igraph as ig
import matplotlib.pyplot as plt

from matplotlib.colors import to_rgba
from mpl_toolkits.mplot3d.art3d import Poly3DCollection
import numpy as np
import pandas as pd
import plotly.graph_objects as go


def arraytrim(VOLOBJ):
    # Store the dimensions of the input 3D array
    dimx, dimy, dimz = VOLOBJ.shape

    # Prepare vectors that will indicate which planes to trim
    trimx = np.full(dimx, -1)
    trimy = np.full(dimy, -1)
    trimz = np.full(dimz, -1)

    # Identify which planes need to be cut and update the appropriate vectors for X, Y, Z dimensions
    for plane in range(dimx):
        if np.sum(VOLOBJ[plane, :, :]) == 0:
            trimx[plane] = plane
    for plane in range(dimy):
        if np.sum(VOLOBJ[:, plane, :]) == 0:
            trimy[plane] = plane
    for plane in range(dimz):
        if np.sum(VOLOBJ[:, :, plane]) == 0:
            trimz[plane] = plane

    # Identify low-end indices for performing the trimming
    xindexlow = next((i for i, x in enumerate(trimx) if x == -1), dimx)
    yindexlow = next((i for i, y in enumerate(trimy) if y == -1), dimy)
    zindexlow = next((i for i, z in enumerate(trimz) if z == -1), dimz)

    # Identify high-end indices for performing the trimming
    xindexhigh = next((i for i, x in enumerate(trimx[::-1]) if x == -1), dimx)
    yindexhigh = next((i for i, y in enumerate(trimy[::-1]) if y == -1), dimy)
    zindexhigh = next((i for i, z in enumerate(trimz[::-1]) if z == -1), dimz)

    xindexhigh = dimx - xindexhigh - 1
    yindexhigh = dimy - yindexhigh - 1
    zindexhigh = dimz - zindexhigh - 1
```

```
    # Correct for null dimensions when trimming is not required
    if xindexlow == dimx:
        xindexlow = 0
    if yindexlow == dimy:
        yindexlow = 0
    if zindexlow == dimz:
        zindexlow = 0

    if xindexhigh == -1:
        xindexhigh = dimx - 1
    if yindexhigh == -1:
        yindexhigh = dimy - 1
    if zindexhigh == -1:
        zindexhigh = dimz - 1

    # Perform and return the subset
    return VOLOBJ[xindexlow:xindexhigh + 1, yindexlow:yindexhigh + 1, zindexlow:zindexhigh + 1]


def validate_data_cube(datacube):
    # First check if data provided is a numpy array
    if isinstance(datacube, np.ndarray):
        # If data is a numpy array
        # # Check if the array is numeric
        if np.issubdtype(datacube.dtype, np.number):
            #If array is numeric, check if the array is 3 dimensional
            if datacube.ndim == 3:
                # Finally check if array is binary
                if np.all(np.logical_or(datacube == 0, datacube == 1)):
                    print("\n\n Data passes all tests \n\n")
                    return True
                else:
                    print("\n\n ERROR 004 - Input data does not contain proper 0,1 binary data.\n\n")
                    return False
            else:
                print("\n\nERROR 003 - Input data is not a 3D array.\n\n")
                return False
        else:
            print("\n\nERROR 001 - Input data is not numeric.\n\n")
            return False
    else:
        print("\n\nERROR 002 - Input data is not a numpy array.\n\n")
        return False
```

```
def morph3dlinks(VOLOBJ=None, VOXELIDS=None, VERBOSE=False):

    """
    Performs 3D Morphological Segmentation on a volumetric object.

    Parameters:
    - VOLOBJ: 3D numpy array (0 for background, 1 for object of interest)
    - VOXELIDS: 3D numpy array of the same shape as VOLOBJ
    - VERBOSE: Boolean, if True, prints additional information

    Returns:
    - DataFrame: Pandas DataFrame containing the results of the segmentation
    """

    if VERBOSE:
        print(f"\nStarting 3D Morphological Segmentation on object: {VOLOBJ}.\n")

    # Store dimensions of the expanded array
    lrgarraydim = VOLOBJ.shape

    # Initialize shifting arrays to zeros
    up = np.zeros_like(VOLOBJ)
    down = np.zeros_like(VOLOBJ)
    left = np.zeros_like(VOLOBJ)
    right = np.zeros_like(VOLOBJ)
    forward = np.zeros_like(VOLOBJ)
    backward = np.zeros_like(VOLOBJ)

    lrgvoxelIDS = np.zeros_like(VOLOBJ)
    lrgvoxelIDS[1:lrgarraydim[0]-1, 1:lrgarraydim[1]-1, 1:lrgarraydim[2]-1] = VOXELIDS

    # Shift down
    down[:, :, 1:lrgarraydim[2]-1] = lrgvoxelIDS[:, :, 2:lrgarraydim[2]]
    down = down[1:lrgarraydim[0]-1, 1:lrgarraydim[1]-1, 1:lrgarraydim[2]-1]

    # Shift up
    up[:, :, 1:lrgarraydim[2]-1] = lrgvoxelIDS[:, :, 0:lrgarraydim[2]-2]
    up = up[1:lrgarraydim[0]-1, 1:lrgarraydim[1]-1, 1:lrgarraydim[2]-1]

    # Shift left
    left[:, 1:lrgarraydim[1]-1, :] = lrgvoxelIDS[:, 2:lrgarraydim[1], :]
    left = left[1:lrgarraydim[0]-1, 1:lrgarraydim[1]-1, 1:lrgarraydim[2]-1]
```

```
# Shift right
right[:, 1:lrgarraydim[1]-1, :] = lrgvoxelIDS[:, 0:lrgarraydim[1]-2, :]
right = right[1:lrgarraydim[0]-1, 1:lrgarraydim[1]-1, 1:lrgarraydim[2]-1]

# Shift forward
forward[1:lrgarraydim[0]-1, :, :] = lrgvoxelIDS[2:lrgarraydim[0], :, :]
forward = forward[1:lrgarraydim[0]-1, 1:lrgarraydim[1]-1, 1:lrgarraydim[2]-1]

# Shift backward
backward[1:lrgarraydim[0]-1, :, :] = lrgvoxelIDS[0:lrgarraydim[0]-2, :, :]
backward = backward[1:lrgarraydim[0]-1, 1:lrgarraydim[1]-1, 1:lrgarraydim[2]-1]

# Extract the original size from the large array
VOLOBJ = VOLOBJ[1:lrgarraydim[0]-1, 1:lrgarraydim[1]-1, 1:lrgarraydim[2]-1]

# Flatten the arrays for easier aggregation into a DataFrame
VOLOBJ_flat = VOLOBJ.flatten()
VOXELIDS_flat = VOXELIDS.flatten()
up_flat = up.flatten()
down_flat = down.flatten()
left_flat = left.flatten()
right_flat = right.flatten()
forward_flat = forward.flatten()
backward_flat = backward.flatten()

# Aggregate results into a DataFrame
df = pd.DataFrame({
    'VOLOBJ': VOLOBJ_flat,
    'VOXELIDS': VOXELIDS_flat,
    'up': up_flat,
    'down': down_flat,
    'left': left_flat,
    'right': right_flat,
    'forward': forward_flat,
    'backward': backward_flat
})

# Filter the DataFrame for rows where VOLOBJ == 1
df = df[df['VOLOBJ'] == 1]

# Return the result
return df
```

```
def _dark_3d_style(ax, fig):
    fig.patch.set_facecolor("black")
    ax.set_facecolor("black")

    for axis in (ax.xaxis, ax.yaxis, ax.zaxis):
        try:
            axis.pane.set_visible(False)
        except Exception:
            pass

    try:
        ax.w_xaxis.line.set_color((0, 0, 0, 0))
        ax.w_yaxis.line.set_color((0, 0, 0, 0))
        ax.w_zaxis.line.set_color((0, 0, 0, 0))
    except Exception:
        pass

    ax.grid(False)


def _light_3d_style(ax, fig):
    fig.patch.set_alpha(0)
    ax.set_facecolor((1, 1, 1, 0))

    for axis in (ax.xaxis, ax.yaxis, ax.zaxis):
        try:
            axis.pane.set_visible(False)
        except Exception:
            pass

    try:
        ax.w_xaxis.line.set_color((0, 0, 0, 0))
        ax.w_yaxis.line.set_color((0, 0, 0, 0))
        ax.w_zaxis.line.set_color((0, 0, 0, 0))
    except Exception:
        pass

    ax.grid(False)
    ax.set_axis_off()


def _draw_cube_lattice(ax, shape, step=1, color=(1, 1, 1, 0.08), lw=0.45):
    """
    Faint full-cube wireframe lattice, like your example.
    shape = (nx, ny, nz)
```

```
    """
    nx, ny, nz = shape
    xs = np.arange(0, nx + 1, step)
    ys = np.arange(0, ny + 1, step)
    zs = np.arange(0, nz + 1, step)

    # lines parallel to x
    for y in ys:
        for z in zs:
            ax.plot([0, nx], [y, y], [z, z], color=color, linewidth=lw)

    # lines parallel to y
    for x in xs:
        for z in zs:
            ax.plot([x, x], [0, ny], [z, z], color=color, linewidth=lw)

    # lines parallel to z
    for x in xs:
        for y in ys:
            ax.plot([x, x], [y, y], [0, nz], color=color, linewidth=lw)

def _set_axes_equal(ax, xlim, ylim, zlim):
    """
    Force equal scale on x/y/z so voxels look like perfect cubes.
    """
    ax.set_xlim(xlim)
    ax.set_ylim(ylim)
    ax.set_zlim(zlim)

    x_range = xlim[1] - xlim[0]
    y_range = ylim[1] - ylim[0]
    z_range = zlim[1] - zlim[0]
    max_range = max(x_range, y_range, z_range)

    x_mid = (xlim[0] + xlim[1]) / 2
    y_mid = (ylim[0] + ylim[1]) / 2
    z_mid = (zlim[0] + zlim[1]) / 2

    half = max_range / 2
    ax.set_xlim(x_mid - half, x_mid + half)
    ax.set_ylim(y_mid - half, y_mid + half)
    ax.set_zlim(z_mid - half, z_mid + half)

    # Newer Matplotlib supports this (best when available)
    try:
```

```
        ax.set_box_aspect((1, 1, 1))
    except Exception:
        pass


def morph3dplot(
    data,
    title="3D Morphology",
    show_title=False,
    save_path=None,
    save_dpi=300,

    # what to show
    plot_codes=None,          # e.g. [5] for CIRCUIT only, or [2,5,7]
    show_skin=True,           # show SKIN (code 3) as ash
    show_outside=False,       # outside is code 1

    # styling
    dark=False,                # black background
    ticks=False,              # remove tick numbering
    wireframe_cube=False,      # draw full cube lattice
    lattice_step=2,

    # skin style
    skin_as_ash=True,
    skin_alpha=0.03,

    # voxel edges
    solid_alpha=0.98,
    solid_edge_alpha=0.02,
    linewidth=0.15,
    axis_order=(2, 1, 0),
    flip_axes=(True, False, False),
    elev=18,
    azim=60,
    show_axes_arrows=False,
    arrow_scale=1.0,
    arrow_color="black",
    arrow_linewidth=2.0,
    show_axis_labels=True,
    axis_name_map=("X", "Y", "T"),
    **kwargs,
):
    """
    Expects a DataFrame with columns: x, y, z, value
```

```
    Codes:
      0 background
      1 OUTSIDE
      2 MASS
      3 SKIN
      4 CRUMB
      5 CIRCUIT
      6 ANTENNA
      7 BOND
      8 VOID-VOLUME
      9 VOID
    """

    # ---- build cube from points ----
    x = data["x"].to_numpy().astype(int)
    y = data["y"].to_numpy().astype(int)
    z = data["z"].to_numpy().astype(int)
    v = data["value"].to_numpy().astype(int)

    nx = x.max() + 1
    ny = y.max() + 1
    nz = z.max() + 1

    vals = np.zeros((nx, ny, nz), dtype=int)
    vals[x, y, z] = v

# --- axis mapping to match R/rgl orientation ---
    vals = np.transpose(vals, axis_order)

    fx, fy, fz = flip_axes
    if fx:
       vals = vals[::-1, :, :]
    if fy:
       vals = vals[:, ::-1, :]
    if fz:
       vals = vals[:, :, ::-1]

# update dims after transforms (important for lattice + limits)
    nx, ny, nz = vals.shape

    # ---- consistent RGBA colors by CODE ----
    cmap = {
        1: (0.75, 0.75, 0.75, 0.10),      # OUTSIDE  -> grey
        2: (0.00, 0.50, 0.00, solid_alpha), # MASS -> green
```

```
    3: (0.00, 0.00, 0.00, skin_alpha),  # SKIN -> black
    4: (0.65, 0.16, 0.16, solid_alpha), # CRUMB -> brown
    5: (1.00, 0.65, 0.00, solid_alpha), # CIRCUIT -> orange
    6: (1.00, 0.75, 0.80, solid_alpha), # ANTENNA -> pink
    7: (0.39, 0.58, 0.93, solid_alpha), # BOND -> cornflowerblue
    8: (0.00, 0.00, 0.50, solid_alpha), # VOID-VOLUME -> navy
    9: (0.40, 0.55, 0.34, solid_alpha), # VOID -> seagreen
    10:(0.25, 0.45, 0.85, solid_alpha)  # ObjectID (custom)
}

# ---- decide what to plot ----
if plot_codes is None:
    # default: all morphological classes except 0 and 1
    plot_codes = [2, 4, 5, 6, 7, 8, 9]
    if show_skin:
        plot_codes = [3] + plot_codes

if not show_outside and 1 in plot_codes:
    plot_codes = [c for c in plot_codes if c != 1]

if not show_skin and 3 in plot_codes:
    plot_codes = [c for c in plot_codes if c != 3]

# ---- start plot ----
fig = plt.figure(figsize=(7.8, 7.8), dpi=150)
fig.patch.set_alpha(0)
ax = fig.add_subplot(111, projection="3d")

if dark:
    _dark_3d_style(ax, fig)
else:
  _light_3d_style(ax, fig)


if wireframe_cube:
   lattice_color = (1, 1, 1, 0.08) if dark else (0, 0, 0, 0.08)
   _draw_cube_lattice(ax, (nx, ny, nz), step=lattice_step, color=lattice_color, lw=0.45)


# ---- plot SKIN as transparent ash (code 3) ----
# IMPORTANT: SKIN IS 3
if show_skin and (3 in plot_codes):
    mask_skin = (vals == 3)
    if mask_skin.any():
        ash = (0.75, 0.75, 0.75, 0.28)
```

```
        ax.voxels(
            mask_skin,
            facecolors=ash,
            edgecolor=(0.4, 0.4, 0.4, 0.18),
            linewidth=0.22,
            shade=False
        )

# ---- plot selected classes as SOLID colored voxels ----
for code in plot_codes:
    if code == 3:
        continue
    mask = (vals == code)
    if not mask.any():
        continue
    col = cmap.get(code, (1, 1, 1, solid_alpha))
    ax.voxels(
        mask,
        facecolors=col,
        edgecolor=(0.15, 0.15, 0.15, 0.25),
        linewidth=0.35,
        shade=False
    )

# ---- formatting ----
if show_title and title:
   ax.set_title(title, color=("white" if dark else "black"), pad=14)

if not ticks:
    ax.set_xticks([])
    ax.set_yticks([])
    ax.set_zticks([])

_set_axes_equal(ax, (0, nx), (0, ny), (0, nz))
ax.view_init(elev=elev, azim=azim)
ax.set_proj_type("ortho")
    # ---- optional axis arrows ----
if show_axes_arrows:
    L = max(nx, ny, nz) * 0.25 * arrow_scale
    # Determine which original axis each plotted axis corresponds to
    # axis_order tells us: plotted axis 0 came from original axis axis_order[0], etc.
    # flip_axes tells us whether plotted axis direction is reversed.
    fx, fy, fz = flip_axes
    orig_names = list(axis_name_map)
```

```
        plotted_to_orig = [orig_names[i] for i in axis_order]
        plotted_signs = [-1 if fx else 1, -1 if fy else 1, -1 if fz else 1]

        # Helper to format label like X, -X, T, -T
        def _fmt(name, sgn):
            return f"-{name}" if sgn < 0 else f"+{name}"

        # X arrow
        ax.quiver(0, 0, 0,
                  L, 0, 0,
                  color=arrow_color,
                  linewidth=arrow_linewidth,
                  arrow_length_ratio=0.12 )

        # Y arrow
        ax.quiver(0, 0, 0,
                  0, L, 0,
                  color=arrow_color,
                  linewidth=arrow_linewidth,
                  arrow_length_ratio=0.12)

        # Z arrow
        ax.quiver(0, 0, 0,
                  0, 0, L,
                  color=arrow_color,
                  linewidth=arrow_linewidth,
                  arrow_length_ratio=0.12)

        if show_axis_labels:
            ax.text(L, 0, 0, _fmt(plotted_to_orig[0], plotted_signs[0]), color=arrow_color)
            ax.text(0, L, 0, _fmt(plotted_to_orig[1], plotted_signs[1]), color=arrow_color)
            ax.text(0, 0, L, _fmt(plotted_to_orig[2], plotted_signs[2]), color=arrow_color)   # or "Z"

    fig.tight_layout()

    if save_path is not None:
        fig.savefig(save_path, dpi=save_dpi, bbox_inches="tight", pad_inches=0, transparent=True)

    return fig, ax



def morph3dprep(incube, orig=False, FINAL=False):
    """
```

```
Convert a 3D numpy array (nx, ny, nz) into a DataFrame with columns:
x, y, z, value
"""
nx, ny, nz = incube.shape

# Build coordinates in the SAME axis order as incube indexing: incube[x, y, z]
x, y, z = np.meshgrid(
    np.arange(nx),
    np.arange(ny),
    np.arange(nz),
    indexing="ij"
)

df = pd.DataFrame({
    "x": x.ravel(order="C"),
    "y": y.ravel(order="C"),
    "z": z.ravel(order="C"),
    "value": incube.ravel(order="C")
})

# If you ever need the "orig" behavior, keep it explicit
if orig:
    df["value"] = df["value"] + 1

return df
```